A Dy:YAG COATED FIBER OPTIC THERMAL SENSOR - PROOF OF CONCEPT

by

Dan Wrona

Thesis submitted to the Faculty of the
Virginia Polytechnic Institute and State University
in partial fulfillment of the requirements for the degree of

MASTER OF SCIENCE

in

Mechanical Engineering

APPROVED:

U. Vandsburger, Chairman

A. L. Wicks

S. B. Desu

October 1995

Blacksburg, Virginia

c.2

A PROOF OF CONCEPT Dy:YAG COATED FIBER OPTIC THERMAL SENSOR

by
Dan Wrona
Committee Chairman: Uri Vandsburger
Virginia Polytechnic Institute and State University
Department of Mechanical Engineering

Abstract

The goal of the research was to develop a non-intrusive optical thermal sensor which could withstand the high temperature, reacting flow environment of operational turbines. A fiber optic thermal sensing design was chosen because of two main attributes, one was the remote/non-intrusive sensing and the other was the distributed sensing potential (the ability to measure temperature as a function along the fiber).

In the prototype sensor design a Dy:YAG layer was coated onto the core of a fused silica optical fiber. The Dy:YAG is a ceramic material which fluoresces in the visible when excited with ultra-violet radiation. The visible emission has a direct correlation with temperature up to the melting point of the ceramic (~2100 K). The basic mechanism used to excite the Dy:YAG is the evanescent wave coupling of the guided pump radiation out of the core and into the coating. This mechanism was utilized to produce bound rays within the fiber from the Dy:YAG emission signal which in turn are guided to a detector. The pump radiation was launched into the fiber core to remove optical path difficulties in

turbines allowing a spatially distributed sensor capable of measuring the temperature as a function of distance along a single fiber.

The ceramic material (dysprosium doped yttrium aluminum garnet) was synthesized utilizing a precipitation reaction and x-ray diffraction patterns confirmed the existence of a YAG crystalline structure. An excimer pulsed laser deposition coating technique offered the best thin film uniformity and adhesion properties (as in the Eu:Y_2O_3 thin film), but the existing facilities could not coat the Dy:YAG thin film due to temperature limitations of the substrate heater. Therefore, the fibers were coated with a thick film using a slurry bonding technique.

The main objective of the experiments conducted as part of this study were to evaluate the effectiveness of the evanescent pump/emission wave coupling and external pumping of the coated fibers. The external pumping of the coated fibers showed that the emission signal can be separated from the background noise with a rather fast, 20 picosecond per point sampling rate, oscilloscope. This was not the case for the majority of the measurements (the noise was greater than the signal) taken with an oscilloscope which could not resolve the pulse (5-6 data points resolution vs. ~5,000). Therefore, further investigation is needed to determine the feasibility of the Dy:YAG coated fiber optic thermal sensor.

ACKNOWLEDGMENTS

I would like to express my thanks to my advisor, Dr. Vandsburger, and committee members for their time and support. I thank Dr. Wicks for finding a high speed oscilloscope at the last minute. I would like to thank Dr. Desu for access to the MSE facilities and especially Dilip Vijay, Claire Chen, and Xubai for helping me with my materials problems. Also, I thank Dr. Datta and Shokai Yang for assisting with the synthesis of the YAG crystals. I thank the Fiber and Electro-Optics Research Center in the EE department for their valuable consultation, especially Dr. Claus, Vikram, and Jason Zeakes.

Special thanks are due to the students I have worked with in the Reacting Flows Lab for their assistance and friendship. I would like to thank the ME department and staff for their advice and help on my research. Without their help my research would not amount to much.

Finally, I thank my parents for their continuous encouragement and support.

TABLE OF CONTENTS

LIST OF FIGURES

1.0 INTRODUCTION

1.1 MOTIVATION

Temperature plays a major role in the design of hot gas turbines; ranging from power generation turbines to high performance aircraft engines. High temperature turbine blade materials impervious to thermal stresses are required for high turbine efficiency and long engine life. However, a non-uniform temperature distribution in the hot gas stream can produce hot spots which may damage blade materials and cause failure. Therefore, sensors are paramount for testing and improving the performance of gas turbines, enabling measurement of temperature and heat flux over the whole blade surface.

Current heat flux sensing technology is inadequate (as listed below) for testing operational turbines. Thermocouples (TC's) are used extensively for heat flux measurements, but have several drawbacks. Extreme combustor temperatures are at the upper limits of thermocouple sensing ranges. Because of the point sensing nature of thermocouples, many thermocouples and accompanying leads are needed for each blade. The leads and thermocouple must not interfere with hot gas or cooling flow for accurate temperature and heat flux measurements. Optical pyrometers are also used to measure heat flux in turbines, but are difficult (and in some cases impossible) to use in an operational turbine because of the need for an unobstructed optical path for temperature

measurements. The thermal emission from the reacting flows within a turbine also interferes with pyrometer measurements.

An optical heat flux sensor was investigated by Cole [1993] for the Reacting Flows Laboratory to overcome the temperature limits and flow interference problems of existing technologies. The proposed design utilized a thin film thermographic phosphor to measure the temperature of an entire turbine blade. When excited with ultraviolet radiation, the thermographic phosphor emits visible radiation which has a direct temperature correlation. A dual layer film would be used to derive the heat flux from the temperature and distance between films. A uniform and thin film is required to coat the blades to insure turbine flow is unaffected.

A thin film was deposited onto a quartz substrate to calibrate the temperature versus emission intensity of the phosphor. The phosphor was excited with an excimer laser orthoganol to the thin film surface. The majority of the visible emission from the phosphor tunneled into and was guided by the substrate. This made temperature calibration by measuring the emission normal to plane of the substrate difficult. However, the wave guided emission signal produced the concept of an intrinsic heat flux sensor. The proposed design may eliminate the optical path difficulties of the thin film sensor through the use of a wave-guiding substrate. A substrates would coat an entire blade with the thermographic phosphor as shown in Figure 1.1.

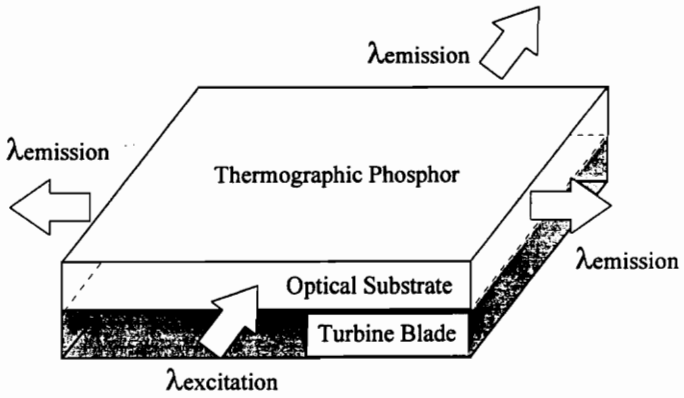

Figure 1.1: Intrinsic Heat Flux Sensor

The wave-guide (optical substrate) pipes the pumping radiation and emitted signal to and from the thermographic phosphor on the entire turbine blade.

Distinguishing signals from various points along the turbine blade is a difficult signal processing task. Deconvolving pulses from the entire blade is expensive (if not impossible) with current digital conversion speeds and computing power. Therefore, a proof of concept fiber-optic sensor has been examined. Eventually, the sensor will utilize numerous fibers to measure a distributed heat flux.

1.2 SENSOR BACKGROUND

Optical fibers are sensitive to a wide range of external influences, one is temperature. An optical fiber temperature sensor measures the external temperature field without significantly disturbing the sensing environment while being completely immune to

external electro-magnetic interference. An advantage of fiber optic sensors is one component (the optical fiber) contains the sensing element and transmission line.

Optical fibers utilize many physical phenomena to measure temperature. Phosphorescent emission from rare-earth and transition doped phosphors has long been used to measure temperatures, Allison, et al. [1987], Bizzak and Chyu [1994], and Goss, et al. [1989]. Ultraviolet radiation pumps the phosphor's dopant ion electrons into a higher energy state and visible light is emitted (phosphorescence) as the electrons relax to their lower energy state. The emission spectrum depends on the relaxation mechanisms, which have a direct temperature correlation—decay lifetime or intensity ratio of the phosphorescence. Decay-time and intensity ratio signals both have the advantage of being intensity independent, implying they do not need a reference signal.

An optical fiber coated with a Dy:YAG thin film was constructed to test the concept of a thermographic phosphor temperature sensor. Combining high resolution with extreme temperatures were the primary design parameters of the proposed distributed fiber optic temperature sensing system.

Distributed fiber optic sensors offer great potential for temperature sensing. Theoretically a temperature distribution can be measured continuously as a function of position. The

spatial resolution is determined by differentiating between the various temperatures along the fiber.

High temperature thermographic phosphor synthesis, fiber doping techniques, optical temperature calibration, and distributed sensing principles were examined to determine the feasibility of the fiber optic thermal sensor.

1.3 EXISTING PHOSPHOR TEMPERATURE SENSOR TECHNOLOGY

Various thermographic phosphors exhibit a temperature dependent emission spectrum and have long been used to measure surface temperatures. The following sections contain a survey of temperature sensing technologies.

1.3.1 THERMOGRAPHIC PHOSPHOR SURFACE TEMPERATURE SENSORS

Allison, et al. [1987], used a La_2O_2S:Eu phosphor to monitor the temperature of an operational jet engine. A temperature correlation could be acquired from either the phosphorescent decay lifetime or intensity ratios at two different wavelengths. The temperature sensing range recorded was 100 to 180°C. A heat flux was calculated from recorded temperature data for a phosphor coated variable area ejector on an operational jet engine and thermocouple data. The binder and phosphor wore off the ejector after a few hours of testing.

In another sensing system, Dy:YAG was utilized to measure surface temperatures (Goss, et al. [1989]). A two dimensional array detector was used to record a surface temperature distribution. A surface was coated with small (<50μm) Dy:YAG crystals and excited with ultraviolet radiation (tripled output of a Nd:YAG laser—355 nm). The 1024-element intensified diode array was used to measure the 467 - 496 nm emission ratio which correlates to the surface temperature. The intensified diode array determined the spatial resolution of the surface measurement, more precise (greater resolution) detectors can measure a finer spatial resolution for temperature. The detector noise was around 3% and negated the strong crystal emission for precise measurements. For the experimental temperature measurement range of 300-1500 K there is a 9-50 K uncertainty in q-switched single laser shot operation.

In different system, turbine blades were examined. Proof-of-concept experiments were conducted on thermographic phosphor coated turbine blade material substrates by Tobin, et al. [1990]. The substrates were rotated and placed in a jet fuel flame. The sensor temperature ranged from 700 to 1000°C. The test objectives were to 1) demonstrate the ability to view phosphor luminescence through a flame using a low power laser, 2) verify phosphor durability in sustained combustion conditions, and 3) gain sensor experience in measuring operating turbine blade temperatures. Europium doped yttrium vanadate ($Eu:YVO_4$) and yttrium oxide ($Eu:Y_2O_3$) were the thermographic phosphors used. $Eu:YVO_4$ was used to align the optics, because of the strong room temperature

fluorescence, and Eu:Y_2O_3 was sensitive up to 1200°C. Both thermographic phosphor sensing systems utilized the phosphorescent decay lifetimes to measure the temperature. The Eu:Y_2O_3 was deposited onto the blade surface with electron beam deposition to a thickness of 8μm. The sensing system could only distinguish the surface temperature of the turbine blade greater than 0.32 cm diameter.

Because of optical path difficulties, Tobin, et al. [1991] examined a turbine temperature sensor utilizes optical fibers to carry the pump and probe signals. Single and dual fiber optic-probes were designed to remotely measure the temperature of turbine blades coated with thermographic phosphors. The single fiber probe delivered the UV pump energy and the resulting phosphorescence to and from the turbine blade in one fiber versus two in the dual fiber probe. The phosphors were Y_2O_3:Eu, YVO_4:Eu, and YAG:Tb. The decay lifetimes of the phosphors were used to measure temperatures in a flame environment up to 1200 °C. Electron-beam deposition, rf-sputtering, and chemical bonding techniques were used to bond the phosphors to thermal barrier coated substrates. The bonded phosphors survived 1.4 hours of operational turbine tests, however the temperatures were too low to correlate decay lifetimes with temperatures. This type of remote sensor only measures the temperature of a single location on a turbine blade which depends on the optical-fiber's spot size.

In yet another study, decay lifetime versus temperature measurements were obtained by Sami, et al. [1993] for Y_2O_3:Eu (4.52% Eu) and YAG:Tb (5% Tb) for a 27-1095°C temperature range. As temperature increased the decay lifetime of the phosphor decreased due to phonon relaxation mechanisms. Continuous temperature measurements were possible from 550-1000°C with an accuracy of ±5%.

In a technique by Bizzak and Chyu [1994], a novel thermal imaging system based on the fluorescent properties of an europium-doped lanthanum oxysulfide ($La_2O_2S:Eu^{+3}$) was used to measure the temperature. The ratio of the resulting phosphorescence from the temperature sensitive 512 nm radiative transition is compared with the temperature independent 620 nm transition. Temperature is correlated with the integration of the decay lifetimes of the phosphorescent ratio. The areas of the two intensity peaks (integration of decay lifetimes) are compared to improve the accuracy of the measurement.

The temporal resolution of the temperature sensor was as fast as 30 ns, the thermal equilibration time of the phosphor fluorescence. Spatial resolution was as small as the size of the individual phosphor particles (on the order of a fraction of a microns), but detector resolution usually is the limiting factor. Emphasis was placed on a uniformly coated surface free of voids for an accurate surface temperature sensing. Temperatures in

the range of 20 to 60°C were measured with an accuracy of ±0.5°C for a 1 mm square spatial resolution.

All of the aforementioned surface temperature phosphor based measuring techniques have the same problems as optical pyrometers when investigating operational turbines. The optical path requirements and blackbody radiation from the reacting flow in the engine degrade the accuracy of the temperature measurements. Binding methods for coating the phosphor onto surfaces also need improvements. The durability of most coating techniques is limited and typically lasts a few hours at most in a high temperature and or combustion environment. Optical fibers provide a means for overcoming the path requirements of the optical thermal sensors by piping the light to the sensing element. Due to their small diameters, fibers coated with a thermographic phosphor could be embedded within a thermal barrier coating (TBC). This technique would protect the binder and phosphor from the harsh combustion environment and drastically improve the operational durability of the sensor.

1.3.2 DOPED FIBER METHODS

Several temperature sensors based on optical fibers doped with rare-earth ions (i.e. uniformly through the fiber core) have been reported. These sensors are constructed by uniformly doping the core with the phosphor material. These are limited by two factors according to Farries and Fermann [1987]: high absorption rapidly diminishes the useful

signal and the absorption and phosphorescence are considerably broadened by the host fiber which dominates the temperature dependent broadening.

Luxtron's optical thermal sensor, Wickersheim and Sun [1987], measured temperature with europium-activated lanthanum oxysulfide (Eu:La_2O_2S). Excited states of the trivalent europium ion produced sharp line (wavelength) fluorescence. The phosphorescent emission lines correlated with temperature since populations of the excited states are proportional to the temperature. An intensity ratio of the emission phosphorescence was used to produce a temperature measuring instrument which ranges from -100 to 290°C with a precision of ±0.1°C. Another Luxtron thermal sensor, presented in the same source as referenced earlier, relied on the phosphorescent decay lifetime of manganese-activated magnesium fluorogermanate. The measurement range of this sensor was -200 to 450°C with a precision of ±0.5°C.

In another thermal sensor built by Farries and Fermann [1987], a temperature dependent absorption of 1.06 micrometer radiation in neodymium-doped optical fibers was observed. This absorption was utilized to measure temperatures ranging from 20-700°C. The temperature dependent fluorescence at 940 nm was the basis for the sensor. The absorption and fluorescence increased with temperature following a Boltzmann distribution. The experimental setup used 45 m of single-mode optical fiber doped with neodymium. A high temperature oven was used to calibrate the absorption and

phosphorescence from the doped optical fiber. The phosphorescent emission had a dual wavelength emission, however the extended emission lifetimes prevented fine spatial resolution for a distributed sensor. An optical time domain reflectometer (OTDR) was constructed for measuring the spatial temperature distribution which utilizes the absorption properties of the doped fiber. The spatial resolution was determined by the laser pulse width used to measure the temperature. The experiment had poor resolution (on the order of 10 m) due to the 150 ns pulses from a Q-switched Nd:YAG laser. The sensor had an accuracy of 10°C. Due to the large energy in neodymium first excited state or required excitation energy, distributed applications were limited to measuring temperatures above 500°C, but other rare-earths could be used for different sensing ranges.

A study by Quoi, et al. [1992] reported the use of a dual-wavelength distributed fiber sensor to detect average temperature. The application utilized rare-earth doped fibers incorporated into the fiber core by MCVD (Metalorganic Chemical Vapor Deposition) processing. The operating principle of the sensors is based on the temperature dependence of the transmission due to the presence of the trivalent rare-earth ions in the fiber core. The spatially distributed temperature sensor design utilized an intensity ratio at two different wavelengths to measure the temperature The doped fiber sensor had a measurement range of 0-100°C with a 1°C thermal resolution. The shortest length of fiber required to measure the average temperature for this sensor is 1.2 m, which is too

long for turbine blade length scales. Also, distinguishing between two different doped sections along the same fiber was not considered by the authors.

The Smith and Smith [1993] fiber-optic sensor measured the temperature with a thermographic phosphor (Y_2O_2S:Eu) coated on the fiber core. The excitation radiation and resulting phosphor emission were coupled into and out of the fiber core via the evanescent wave phenomena discussed earlier. The phosphor was not uniformly doped within the fiber's cladding, but deposited directly onto the core, because theory taken from Marcuse [1988] shows that light sources located at the core-cladding interface are more efficient at coupling light into the fiber. The sensor configuration coated a length of the fiber core 5 cm long with Y_2O_2S:Eu utilizing a high temperature binder. The emission decay lifetimes (at 538 nm) correlated with temperature ranging from 20 to 180°C. Distributed sensing was mentioned, but there was no supporting investigation. A multi-phosphor coated fiber was suggested to achieve the desired distributed sensor.

2.0 LITERATURE REVIEW

2.1 THERMOGRAPHIC PHOSPHOR THEORY

Thermoluminescence (TL) is the temperature dependent light emission from a material resulting from the stimulation of radiation. TL is governed by the principles of all luminescence processes—which are the general term for the emission of visible radiation from a substance during or following the absorption of energy (excitation) such ultraviolet or high energy radiation.

Fluorescence and phosphorescence are two classifications of luminescence. Lifetimes of excited atoms in the gaseous state less than approximately 10^{-8} seconds are considered fluorescence and longer decay lifetimes are considered phosphorescence. Phosphorescence lifetimes in some solids can last hours and even days. This discussion and theoretical background follows the analysis of Vij [1993].

Luminescence in solids (or powders) is a result of traces of an impurity known as an activator. The activator is doped into the host material crystal lattice by heat treatment. Discrete energy levels created by the addition of the trace impurity, through which radiative recombination can take place, are called luminescent centers. Activators and the presence of vacant sites or other defects and irregularities in the host lattice provide unoccupied levels (or traps) in which electrons get trapped, which are responsible for

delaying the luminescence by detaining the charge carriers (electron-hole pairs) before they recombine at the luminescent centers.

Luminescent emission is explained by the transfer of energy from a radiation source to the electrons of the solid, thus exciting them from a ground state G to an excited state F (Figure 2.1). Fluorescent emission is when the excited electron returns to its ground state independent of temperature (transition 1, Figure 2.1). Excited electrons trapped in the metastable state M emit phosphorescence when enough thermal energy returns them to the ground state G via F (transition 2, Figure 2.1). The delayed emission results from the time the excited electron spends in the metastable level or trap before the recombination reaction returns the electron to its ground state. This simplified phosphorescence model is based on the energy band theory of solids.

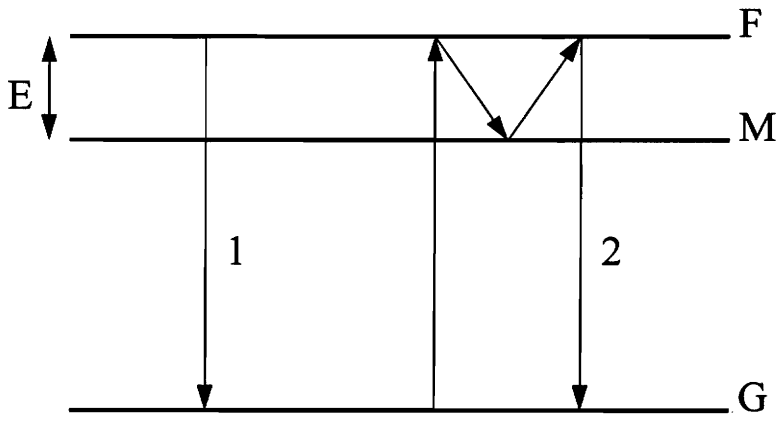

Figure 2.1: Jablonski's model of fluorescence and phosphorescence transitions (Vij [1993])

The phosphorescent decay process of the solid follows second order recombination kinetics, which corresponds to bi-molecular chemical reactions. Second order kinetics depends on the initial luminescence intensity and temperature. The phosphorescent decay lifetime is inversely proportional to the temperature, and decays exponentially. The other recombination reaction, fluorescence, follows first order kinetics (uni-molecular chemical reaction). The decay reactions are also exponential like phosphorescence but are independent of temperature.

There are different models which explain luminescence and thermoluminescence in various phosphors. One models a process where the emission takes place within the luminescent center of the crystal. This model is explained by the configurational coordinate system. Figure 2.2 represents the ground and first excited states of the luminescent center.

The diagram shows the potential energy versus the distance between atoms in the crystal lattice. Absorbed energy pumps the luminescent center to an excited state (transition AA') and relaxes to a stable state B dissipating the energy nonradiatively. Visible emission of light results from transition BB' as the luminescent center returns to the ground state. More nonradiative energy is dissipated as the center returns to the stable state A.

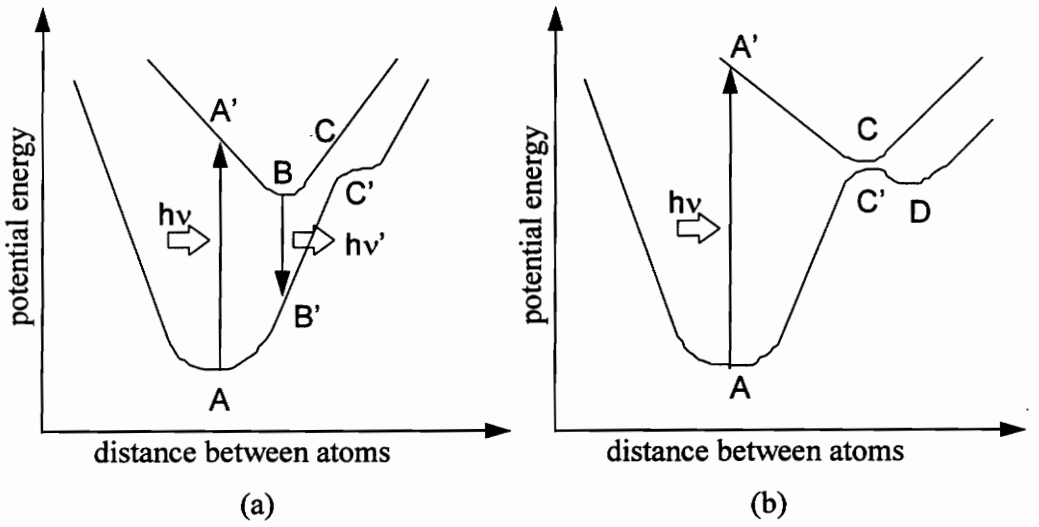

Figure 2.2: Configurational Coordinate Diagram
Atomic center energy configuration conditions for
(a) Luminescence, (b) Radiationless Dissipation
AA'-absorption transition, BB'-luminescence transition,
CC'-radiationless transition, and D-metastable state
(Vij [1993])

This model also allows for quenching or radiationless dissipation of absorbed energy through path A'-C-C'-A. The absorbed energy is transferred to the crystal as phonons or vibrational energy. The decay of the luminescent emission is given by:

$$I = I_0 \exp\left[-(P_r + P_{nr})/t\right.$$

where P_r and P_{nr} are the radiative and nonradiative dissipation of energy, respectively.

Another thermoluminescence model describes the process of emission through ionization of the luminescent center and charge transportation (photoconductivity), on the basis of the band theory of solids. Figure 2.3 represents the modified energy band model.

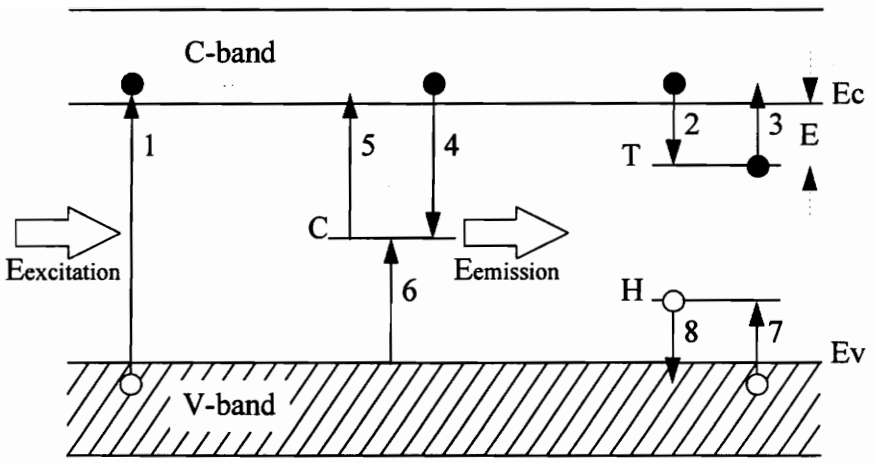

Figure 2.3: Modified Energy Band Model (Vij [1993])

The luminescent centers arise from impurities (e.g. Dysprosium dopant) in the crystal. When the crystal is pumped with more energy than the difference in the band gap energy the electrons are excited to the conduction band from the valence band (transition 1). This transition produces holes in the valence band. The excited electrons return to the valence band by emitting light (phosphorescence) or heating the solid (no emission).

State T traps some of the excited electrons which have corresponding holes at state H, transitions 2 and 7 respectively. Radiative emission occurs when electrons and holes recombine via the luminescent centers (transitions 4 and 6). Electrons may also be pumped to the conduction band if the absorbed energy is greater than the energy difference between C and the C-band. Transitions from T to C and T to the V-band may

also occur, but have the same radiative results as the recombination reaction of transitions 4 and 6 as mentioned above.

The probability (p, per unit time) of the release of an electron from a trap of depth E (activation energy) is:

$$p = s \exp[-E/kT$$

where s is the frequency factor, k is a constant, and T is the temperature. E and s determine the length of non-equilibrium due to the absorbed radiation. Equilibrium is restored when the specimen temperature is raised above the irradiation temperature ($kT \geq E$). At this point the electrons recombine with the trapped holes at the luminescent centers, C, thus producing thermoluminescence (TL). TL intensity I(t) is proportional to the rate of electron/hole recombination at the luminescent center, C.

The charge carriers move through the crystal lattice during irradiation. The carriers travel in the conduction band before the recombination process of trap filling (irradiation or pumping) and trap emptying (thermal excitation) takes place. The processes are governed by a set of simultaneous differential equations describing the traffic of charge carriers between conduction band, valence band, traps, and recombination centers.

The equations below describe the physics of TL. A free electron has an equal probability of going to recombination centers or returning to the same trap. If N is the total number

of traps of which n are occupied at a time t, the probability that a free electron will go to the recombination center is:

$$\frac{n}{N} = \frac{n}{[(N-n)+n]}$$

therefore;

$$I_{TL} = c\frac{n}{N}\frac{dn}{dt} = -cs\exp[-E/kT]\frac{n^2}{N}$$

where c is a constant. By integrating the previous equation, the TL intensity is given by:

$$I_{TL} = \frac{n_0^2 cs' \exp[-E/kT]}{\left[1 + s'\frac{n_0}{\beta}\int_o^T \exp[-E/kT']dT'\right]^2}$$

where n_0 is the initial number of trapped electrons, s' = s/N (cm^2 s^{-1}), and β is the heating rate (dT/dt). At a fixed temperature T, the instantaneous TL intensity is given by:

$$I(t) = I_0/[1 + A' n_0 t]^2$$

where A' = c s' exp(-E/kT).

2.1.1 Dy:YAG Thermoluminescence (TL)

Certain rare-earth ions exhibit a temperature dependent emission spectrum. The rare-earth dysprosium (Dy) is one such material. The temperature sensitivity of the Dy phosphorescent emission spectrum is ideal for an optical thermometer. Existing laser-induced fluorescent (LIF) systems utilize the same principles to measure temperature with various phosphorescent species in both gaseous and solid forms.

Trivalent dysprosium doped at 3.0 mole % (by mass) in yttrium aluminum-garnet (Dy^{+3}:YAG) also exhibits a temperature sensitivity as shown by Goss, et al. [1989]. A "Thermalization" process is responsible for the temperature sensitivity of the Dy:YAG crystal. As the temperature increases more electrons populate the upper levels of the crystal according to Boltzmann's law. When two energy levels of the crystal are closely spaced (around 1000 cm^{-1}) the fluorescent intensity is directly proportional to the temperature. At lower temperatures, there is no upper level population buildup and thus no phosphorescence because of quenching from the multi-phonon reaction rates. But, as the temperature increases the upper level population increases as does the phosphorescent intensity. Temperature is determined by comparing the upper and lower level phosphorescent intensities.

Figure 2.4 illustrates the thermoluminescence of the LIF for the Dy:YAG crystal. Absorbed ultra-violet (UV) light pumps the Dy^{+3} electrons to an excited level. These electrons radiatively and non-radiatively decay to the F and G levels in the crystal. Level G is thermally pumped by level F and the population buildup is related to the temperature. Phosphorescence from the two levels results when the electrons return to the ground state. Both phosphorescent signals are in the visible range, level F centered at 496 nm and level G centered at 467 nm. The intensity of the light from the F level remains fixed but that from the G level increases as the temperature rises. The

phosphorescent intensity for the 467 nm peak falls off at temperatures above 1800 K, but the 512 nm peak may be used from 500 K to the melting point of the YAG crystal (~2100 K). Figure 3.12 contains the Dy:YAG emission spectrum taken from Goss, et al [1989].

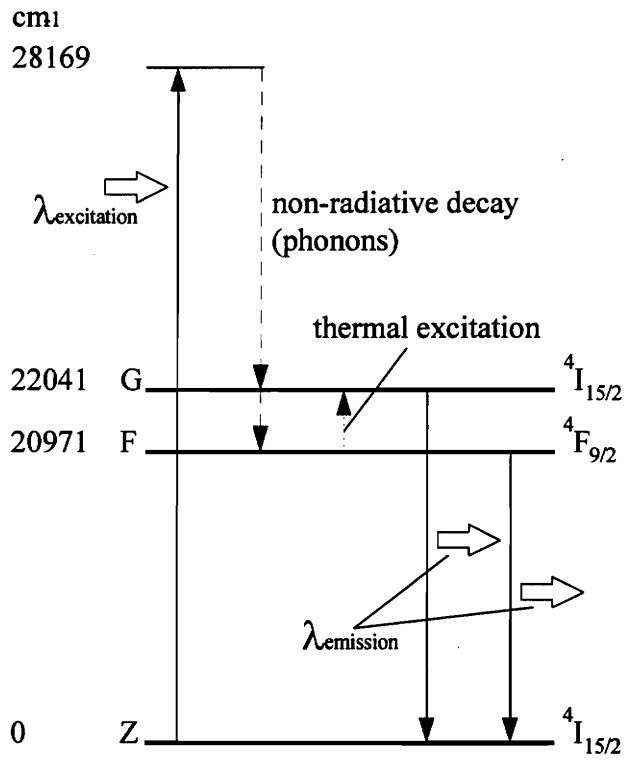

Figure 2.4: Simplified energy diagram of F and G levels of Dy:YAG phosphorescence (Goss, et al. [1989])

2.2 OPTICAL FIBER THEORY

Optical fibers consist of an inner core and an outer layer of cladding as shown in Figure 2.5. The cladding has a lower index of refraction so that the light traveling within the core is reflected and thus continues to remain in the core (Snell's Law). The core has a circular cross section and the cladding is assumed to be infinite. The refractive index of the core may be uniform or graded and the cladding refractive index is constant. The following optical waveguide theory and equations are taken from Snyder and Love [1983].

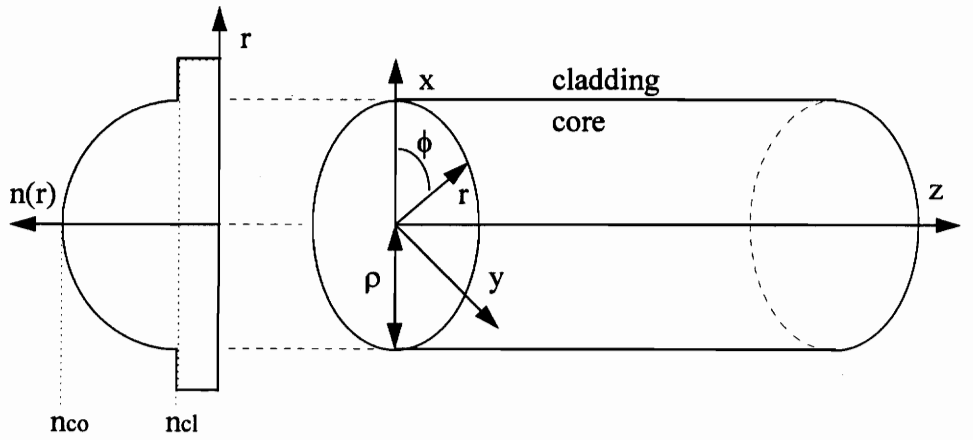

index of refraction profile

Figure 2.5: Nomenclature for Circular Optical Fiber

The dimensionless fiber parameter, V, is defined as:

$$V = \frac{2\pi\rho}{\lambda}\left(n_{co}^2 - n_{cl}^2\right)^{1/2}$$

where n_{co} and n_{cl} are the core and cladding maximum indexes of refraction respectively, ρ is the core radius, and λ is the free-space wavelength of light. Ray theory requires that

V>>1 for multimode fibers. The numerical aperture (NA) is the square root term in the previous equation and the local NA is given by:

$$\left(n_{co}^2 - n_{cl}^2\right)^{1/2}$$

Ray tracing is simple to analyze in step profile fibers. Step profile fibers are fibers with a constant refractive index in the core which is greater than the cladding's. The construction of the ray path follows Snell's Law:

$$n_{co}\cos(\theta_z) = n_{cl}\cos(\theta_t$$

where θ_Z and θ_t are the reflected and transmitted ray angles respectively. Only total internal reflection keeps all the ray's power within the core. Total internal reflection is determined by the compliment of the critical angle; $0 \le \theta_z < \theta_c$. θ_c is the compliment of the critical angle and is given by, $\theta_c = \frac{1}{\cos(n_{cl}/n_{co})}$. The ray is partially reflected and partially refracted if $\theta_c \le \theta_z \le \frac{\pi}{2}$. Refracting and tunneling rays are considered "leaky", the guided ray within the fiber is attenuated, or some or all of its energy is transferred into the cladding or surroundings, at the core-cladding interface. The tunneling rays are rays which "tunnel" a finite distance into the cladding analogous to frustrated total internal reflection.

Geometric or ray optics cannot describe fiber power transmission loss due to cladding absorption. The loss occurs beyond the ray path and is a diffraction/wave effect

dependent of the wavelength of the light traveling in the core. The power loss can be explained by using ray optics along with assuming that all the energy is lost at the reflections in the core by treating the ray locally as a plane wave. The expression for power loss in step profile fibers is derived from plane-wave reflections at a planar interface (first done by Fresnel). Ray power attenuation from the cladding absorption requires the density (or number) of reflections. The total cladding absorption is determined from ray optics by multiplying the number of reflections with the plane-wave losses at each reflection.

2.2.1 EVANESCENT WAVE COUPLING

Classical geometric optics describes light traveling through an optical fiber. Evanescent field losses (cladding absorption and radiation losses) are described by the generalized Fresnel transmission coefficient, but this is only valid for multimode fibers. Maxwell's equations determine the propagation characteristics of electromagnetic waves guided in a fiber. The equations rarely have simple closed form solutions and usually require numerical methods. The problem is simplified by reducing Maxwell's equations to the scalar wave equation. Appendix C outlines the derivation.

Only a portion of the source power is guided within an optical fiber without attenuation. A finite number of bound modes represents the light guided in the fiber (bound modes are the same as bound rays in geometric optics). Bound modes are solutions of Maxwell's

equations and result from resonance conditions in the waveguide cross-section, analogous to the vibration modes of a stretched membrane. The fundamental properties of the bound modes are for ideal fibers—uniform, nonabsorbing, and dielectric waveguides. The fields of the fiber are represented by an expansion over the guided modes (the building blocks for describing light propagation).

Ray optics does not allow light sources located in the cladding to be coupled into the core of positively guiding, step-index optical fibers. Snell's Law dictates that light penetrating the core (higher index of refraction) from the cladding (lower index) travels at angles which exceed the critical angle for total internal reflection. The electromagnetic fields of the plane-waves are evanescent beyond the reflection boundaries and decrease exponentially away from the core's axis. The exponential decay is inversely proportional to the free-space wavelength (λ) of the light in the core. For classical geometric optics ($\lambda = 0$), the fields are zero beyond the reflection in the cladding.

Wave optics illustrates how sources in the cladding interact with evanescent field tails of the guided core modes to transfer energy to these guided modes. The weak guidance approximation describing bound modes shows how light originating in the cladding couples into guided modes within the core. The evanescent fields of the guided modes allow for the coupling. The coupling is similar but opposite to cladding loss

phenomenon, where optical absorbance centers in the cladding cause attenuation in the core.

Lieberman, et al. [1990] represented the evanescent electromagnetic field with a decaying exponential in the cladding coupled with a matching oscillating exponential in the core at the core-cladding interface point of total internal reflection. Without absorbing centers in the cladding all of the tail energy returns to the guided core mode but with the centers the energy is dissipated into the cladding. This is analogous to sources in the cladding exciting a bound mode within the core. The sources represent a decaying exponential of an evanescent tail which in turn excites an oscillating exponential in the core, creating a bound ray.

Incident and reflected rays interfere to produce a standing wave at the interface, as illustrated in Figures 2.6a and 2.6b.

The standing wave has a finite electrical field amplitude ($\overline{E}$) at the interface of two dielectric media. The field decays exponentially into the lower index phase—the field cannot go to zero instantaneously. The exponential decay is called an evanescent wave or tail. According to Andrade, et al. [1985], the penetration depth (d_p) for perpendicularly polarized light is given by:

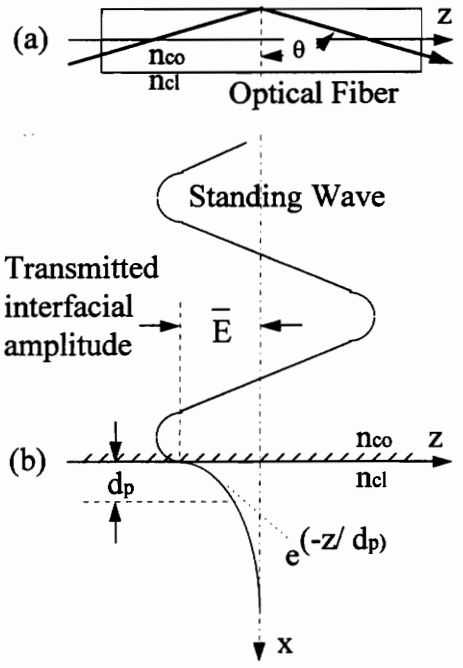

Figure 2.6: Evanescent Wave Coupling Schematic
(a) Side view of total internal reflection. ($n_{co}>n_{cl}$)
(b) The incident and reflected rays interfere to produce a standing wave with an electric field amplitude $\overline{E}$ at the interface which decays exponentially into the cladding with a penetration depth of d_p
(Andrade, et al. [1985])

$$d_p = \frac{\lambda_0}{2\pi \left\{ n_{co}^2 \sin^2(\theta_{co}) - n_{cl}^2 \right\}^{\frac{1}{2}}}$$

The evanescent wave has the same wavelength and polarization properties of the incident wave.

All electromagnetic modes have high field intensities at the core-cladding boundary for step profile fibers. Modes near cutoff collect more light from the cladding sources due to their deeper penetrating evanescent fields compared to the more tightly guided core

modes. The efficiency of light captured by guided modes is proportional to the square of the V number. The "collection efficiency" is defined as the ratio of light collected by the fiber core relative to the total source radiation. According to Marcuse [1988], light power collected by an optical fiber is linearly dependent on fiber length and the collection efficiency increases with greater index of refraction differences (V number).

Fibers with higher V numbers exhibit stronger coupling from sources located at the core-cladding interface. These fibers have a larger number of modes near cutoff and their evanescent fields penetrate further into the cladding. The injection efficiency of thin film coated fibers, i.e., sources located at the core-cladding boundary, increases parabolically with increasing V-number.

The evanescent fields at the optical fiber's core-cladding interface provide the basic mechanism by which the thermographic phosphor is excited. The phosphorescent signal couples back into the fiber utilizing the evanescent tails, but in the opposite direction. Appendix C contains the equations of the pump and emission light guided in the fiber.

2.3 DISTRIBUTED SENSOR PRINCIPLES

Distributed optical fiber sensors detect changes in light propagation through a fiber due to external field variations, e.g., temperature. Propagation delays in backscattered or transmitted light determine the location of the sensing element. Several methods are

available to construct a distributed sensing system and optical time domain reflectometry (OTDR) is one of them. OTDR determines disturbance magnitudes through signal intensity variations. Figure 2.7 shows the basic configuration of distributed fiber optic sensors.

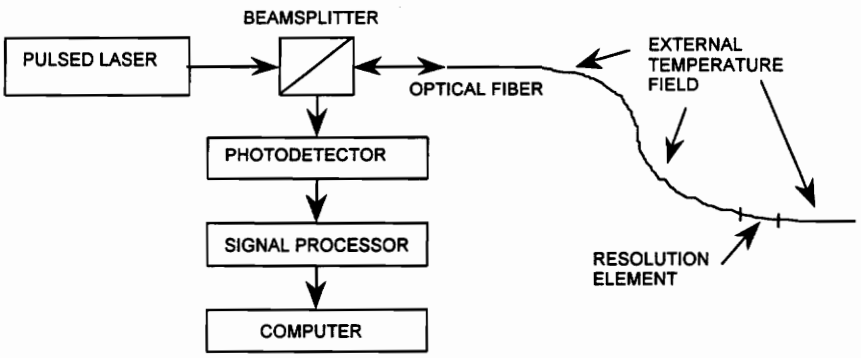

Figure 2.7: Schematic for a backscattered DOFS system

2.3.1 SIGNAL PROCESSING PRINCIPLES

All optical fiber sensor measurements can be represented as four basic types of measurements corresponding to time and frequency derivatives of the transmission or reflection coefficient of the optical fiber. The variation of the amplitude (A) and phase (ϕ) parameters with frequency (ω) and time (t) produce the four measurements: $\partial A/\partial t$, $\partial A/\partial \omega$, $\partial \phi/\partial t$, and $\partial \phi/\partial \omega$. Some of the key parameters in a distributed sensing system are source coherence, spatial resolution, bandwidth, and repetition rate of the optical modulation, Davies [1984].

The simplest signal processing scheme to measure time delay is to transmit short pulses of light and measure the time differences. If phase is also a required measurement then the light must be coherent from pulse to pulse. Optical time domain reflectometry (OTDR) measures the spatial resolution from the propagation delays in the "probe" light signal. The basic concept is an optical wave-guide location principle:

$$l = t \bullet v$$

where l is location, v is the fiber light velocity, and t is the propagation delay, Dakin [1992].

The OTDR range resolution of the measurement is given by half the physical pulse length in the fiber:

$$\Delta R = \frac{1}{2} v\tau$$

where τ is the pulse duration and v is the fiber light velocity taken from Davies [1984]. Increased accuracy and resolution requires shorter pulses and wider bandwidth processing (with consequential increased noise level in the receiver). The noise level in the receiver (which limits the detection of the reflected or transmitted pulses) is proportional to the bandwidth of the receiver which is determined from the reciprocal of the pulse duration. Thus, shorter pulses decrease the SNR and reduce the sensitivity/range performance of the sensor.

A major problem with time of flight distributed sensing systems is accumulative attenuation; as the light (signal) levels at the most distant sensor depends on the measurand at each prior sensor. This places demanding requirements on the dynamic range of the detection system and limits the number of sensors. The sensor data gathering capacity is limited by the bandwidth and signal-to-noise ratio (SNR) of the detected optical signals. According to Dakin [1987], crosstalk between signals from independent sensor elements increases noise in the detected signals.

OTDR and other time of flight sensing methods utilize time division multiplexing (TDM) of the fiber optic wave-guided signals. The time differences between sensor returns is achieved by arranging differing total optical propagation delays for the signals from each sensing element. The simplest form of coding, for ease of both modulation and demodulation, is to use a repetitive short pulse, of duration such that returning differentially delayed pulses from each sensor do not coincide at the detector, and with a repetition rate that is low enough to allow a pulse to return from the most distant element of the sensing array before the following pulse returns from the nearest sensing element, Dakin [1987].

The maximum spatial resolution of an OTDR instrument is determined by the convolution between the probe signal and the impulse response of the receiver filter. In

the limit of infinite filter bandwidth, the filter impulse response becomes a delta function and resolution is limited by the probe signal shape, Healy [1986].

2.4 THERMOGRAPHIC PHOSPHOR OPTICAL SENSING ADVANTAGES

There are many advantages to the thermographic phosphor type sensor compared to reflection and transmission type temperature sensors. Non-temperature related errors like source fluctuations, fiber bending, and optical coupling losses must be removed from the optical signal, either by using a self referencing technique or measuring an intensity independent parameter. Thermographic phosphors measure temperature using decay lifetimes or intensity ratios (both are intensity independent parameters). This is much more difficult to accomplish with transmission/reflection methods, which require an interferometric component to compare with the source.

None of the previously mentioned sensors in the introduction (section 1.3) could be converted into a fully distributed fiber-optic temperature sensor. The systems are either designed as point sensors, the spatial resolution limits are already minimized for distributed sensors, or filtering the temperature dependent signal from unwanted noise is very difficult and expensive digitally

A distributed temperature sensor system can be constructed by filtering the decay spectrum of the fiber. Wavelengths with the largest temperature variations were selected

for the signal processing. The fluorescent efficiency is much higher than light scattering sensing techniques and can be improved through higher doping levels of the fiber. Longer fluorescent lifetimes limit the spatial resolution, but reducing the lifetime decreases the temperature sensitivity of the dopant according to Dakin [1992]. Problems also arise due to non-uniform fiber doping as shown by Rogers [1988].

2.5 GOALS AND OBJECTIVES OF RESEARCH

Existing technology for measuring the temperature of operational turbines is not capable of monitoring a distributed heat flux of internal components. The sensors are point sensors (numerous sensors would be cumbersome and impractical for the desired spatial resolution). Other deficiencies exist but overcoming the non-spatial distributed sensing nature of current systems is the motivation behind the prototype sensor.

Optical sensors offer the most advantages (as shown in previous studies mentioned above) for measuring the temperature profile of turbine components. Remote sensing improvements are incorporated in the current study to overcome past deficiencies. The prototype utilizes thermographic phosphors following proven surface temperature measurement systems. However, phosphor/binder coating techniques have been known to degrade and separate from the fiber rapidly in a combusting and or extreme

temperature environment. Therefore, a better deposition method is needed to construct a thermal optical sensor.

A proof of concept Dy:YAG coated fiber-optic thermal sensor is examined in this thesis. Research done by Lewis, et al. [1990] shows that temperatures up to 1900 K have been measured with Dy:YAG. Different binding techniques are also examined to improve the durability of coated sensors. Therefore, Dy:YAG synthesis, optical fiber binding techniques, and emission signals are examined to determine the feasibility of the proposed fiber-optic temperature sensor. Towards the completion of the current study the author was made aware of a similar effort by Smith and Smith's [1993]. The temperature sensor utilizes numerous phosphors to achieve a spatially distributed sensor. However, the system would be difficult and expensive to manufacture for turbine blade applications.

The objective of the research is to determine if the Dy:YAG optical thermal sensor is worth pursuing for developing the heat flux sensor concept. The following outlines the research goals:

COMPLETED

- thermographic phosphor synthesis
- optical fiber deposition
- emission signal measurements

FUTURE WORK

- temperature correlation
- distributed temperature predictions
- heat flux sensor construction

3.0 EXPERIMENTAL PROCEDURES

3.1 Dy:YAG SYNTHESIS

Yttrium aluminum garnet doped with dysprosium (Dy:YAG) was the thermographic phosphor used to construct the optical thermal sensor. Large, optical quality YAG crystals are commonly used as a lasing medium in Nd:YAG lasers. However, these crystals are quite expensive even without the required activator (Dy) doped into the crystal lattice. Therefore, the Dy:YAG was synthesized from raw materials in the laboratory. The chemical formula for the YAG crystal doped with dysprosium is $Dy:Y_3Al_5O_{12}$.

3.1.1 SOLID STATE REACTION

Dysprosium, aluminum oxide, and yttrium oxide were mixed to produce yttrium aluminum garnet doped with 3 mole % dysprosium (Dy:YAG). The dopant concentration of 3 mole % was chosen in order to match the phosphorescent emission spectrum reported by Goss's, et al. [1989]. A solid state reaction was utilized to synthesize the crystal. The following equations represent the mole ratios for the 3 mole %:

$$Dy:Y_3Al_5O_{12} \text{ (3 mole \% Dy)}$$

$$= (Dy_{0.03}Y_{0.97})_3Al_5O_{12}$$

$$= (Dy_{0.09}Y_{2.91})Al_5O_{12}$$

The following equation shows the mole ratios for the solid-state reaction:

$$0.18Dy + 2.91Y_2O_3 + 5Al_2O_3 \xrightarrow{\Delta} 1.94(Y_3Al_5O_{12}):0.18Dy + \cdots$$

Appendix A inventories the exact raw materials used. The reactants were mixed together and calcinated at 1000°C for 3 hours to remove the impurities from the mixture. This was a high temperature process which produces a powdery-ash material. X-ray diffraction (XRD) was used to validate the synthesized crystalline structures. A simple explanation of the XRD technique is provided in Appendix D. The YAG structure is a cubic system and the reference XRD pattern is shown in Figure 3.1. The peaks on the plot represent different planes and orientations of the crystal structure. 2 θ on the abscissa is the diffraction angle and the ordinate is the intensity of the reflected x-rays. The reference XRD pattern is taken from the Joint Committee on Powder Diffraction Standards (JCPDS), which is referenced in Shackelford, 1988.

Figure 3.2 compares the diffraction pattern of the synthesized 1000°C calcinated mixture with the YAG reference. Identical crystal structures have identical diffraction patterns. The patterns are not identical, therefore the synthesized material did not have a YAG crystalline structure.

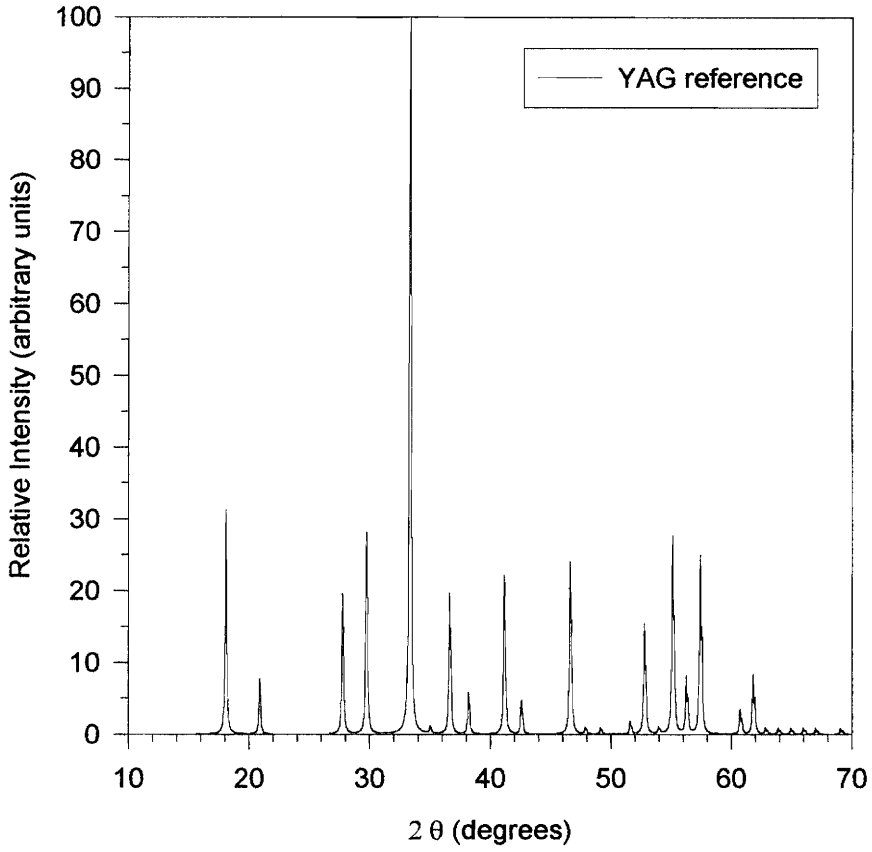

Figure 3.1: YAG reference XRD pattern

Next, the powder was sintered at a higher temperature to assist in the YAG formation. Sintering is a firing process which causes changes in the grain size and shape, pore shape, and size of the powder material. This transformation produces a strong, dense ceramic material. Sintering fills the necks at the point of contact between the powder particles and the pore space, thus increasing the density and strength of the compacted powders.

The powder was sintered at 1300°C for 6 hours. The diffraction pattern for the new material is shown in Figure 3.3 and is close to the reference structure, but not quite the same.

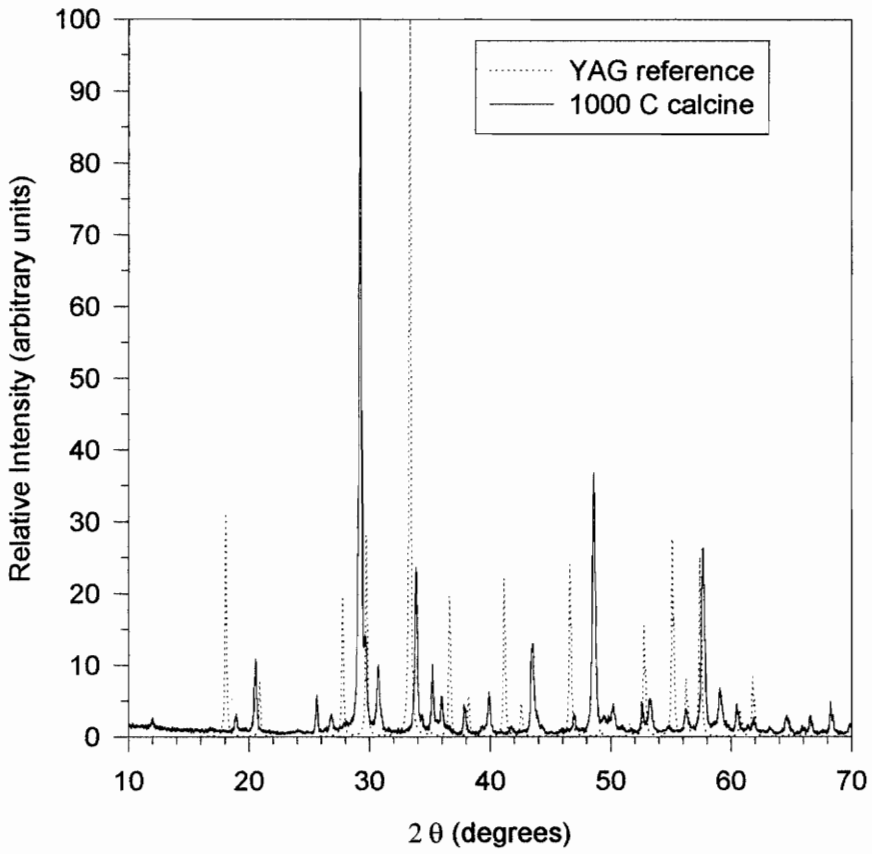

Figure 3.2: XRD comparison of calcinated YAG mixture with reference

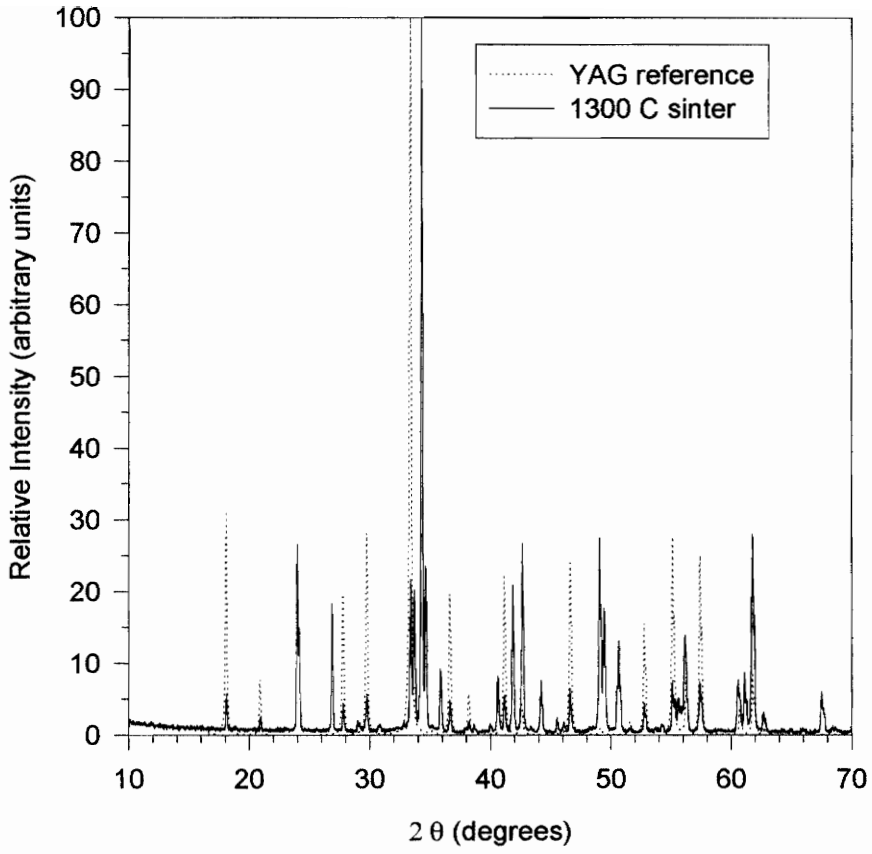

Figure 3.3: XRD comparison of sintered YAG mixture with reference

In a following trial the calcinated powder was sintered at 1500°C for 6 hours to see if the resulting material would transform into the YAG crystalline structure. Figure 3.4 shows its XRD pattern compared with YAG. The diffraction pattern is not the same as the reference and is almost identical to the previously sintered sample (1300°C).

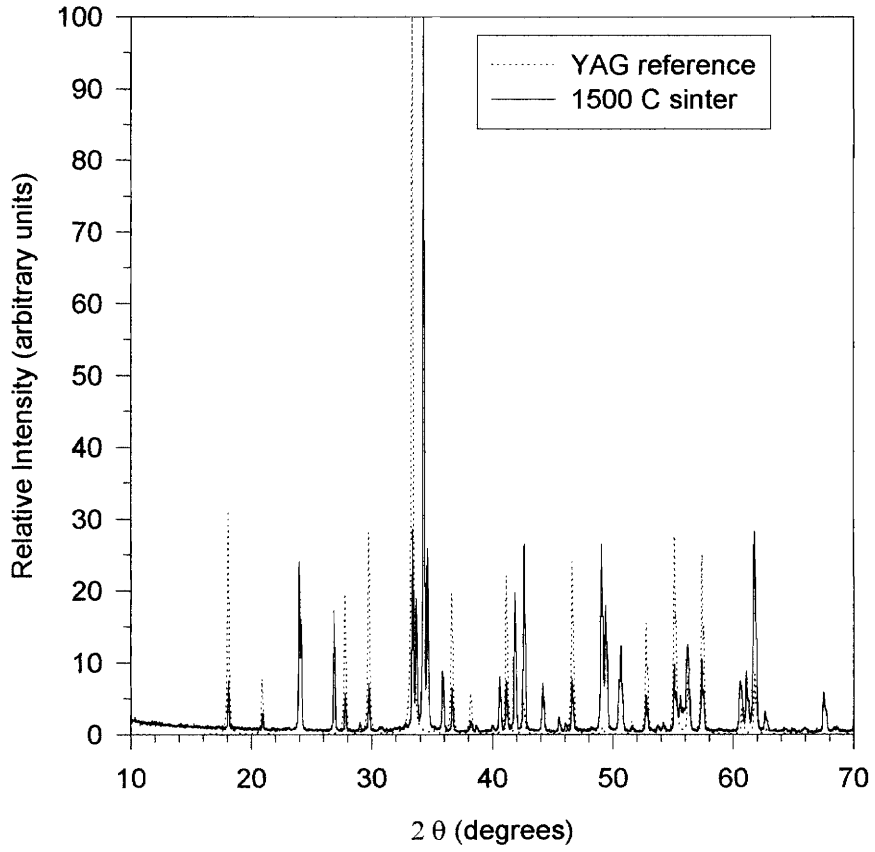

Figure 3.4: XRD comparison of sintered YAG mixture with reference

Since the sintering process did not convert the powder into YAG, a sample was calcinated at 1550°C for 6 hours. Figure 3.5 shows the crystal formed is closer to the YAG structure than previous attempts. However, the pattern is shifted and has a few extra peaks when compared with the YAG reference.

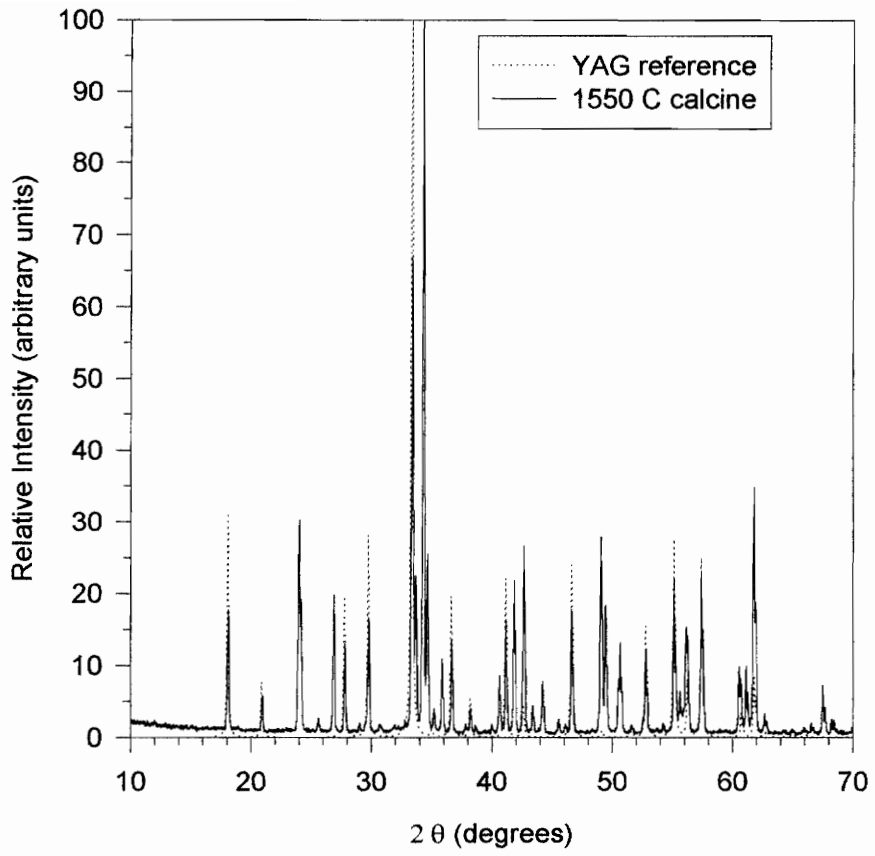

Figure 3.5: XRD comparison of calcinated YAG mixture with reference

The calcinated mixture was sintered next at 1700°C for 6 hours and Figure 3.6 shows its XRD pattern. Most of the peaks match up with the YAG reference's, but there are a few extra peaks. The peaks near 24°, 27°, 31°, 35°, 42°, 49°, and 50° do not exist on the YAG reference XRD pattern, but the peaks that match are identical to the reference.

This material was the closest match to the YAG crystalline structure achieved using the solid-state synthesizing technique.

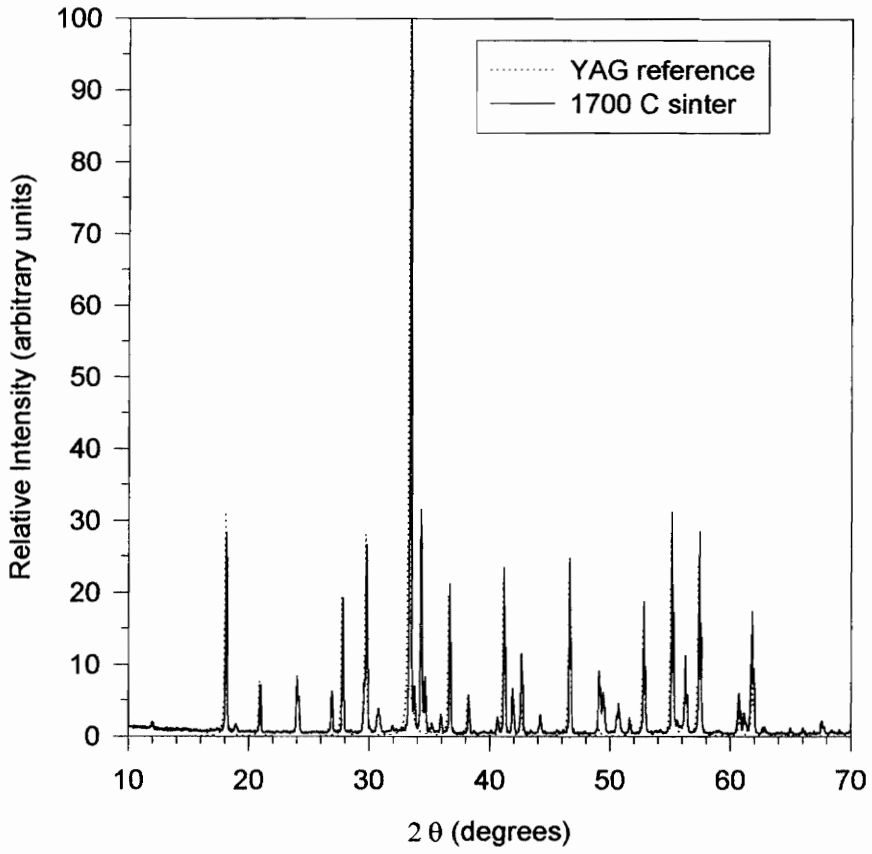

Figure 3.6: XRD comparison of sintered YAG mixture with reference

The 1700°C sintered powder was pressed into a target for pulsed laser deposition (PLD). Appendix E contains a brief discussion on pulsed laser deposition. An Excimer laser

filled with krypton fluorine (KrF) gas was used for the PLD. Figure 3.7 shows a schematic and the experimental conditions for the PLD.

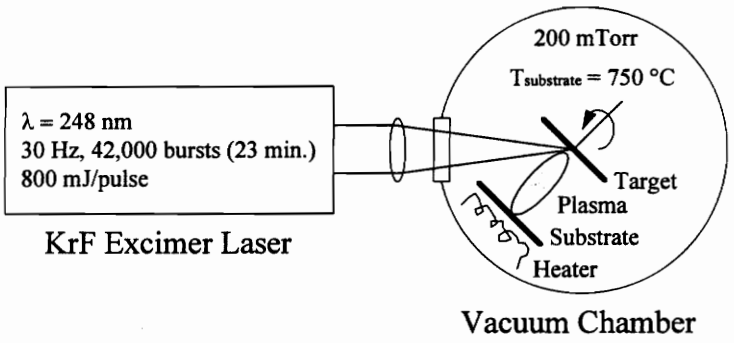

Figure 3.7: Schematic of Pulsed Laser Deposition

The substrate was a 1.27 cm (1/2") diameter fused silica disk. The vacuum chamber accommodated fibers up to 5.08 cm (2") in length, but a flat substrate was needed to verify the thin-film crystal structure. The vacuum chamber was pumped down to 200 mtorr and the substrate was heated to 750°C (the maximum possible heater temperature). The target was ablated with 42,000 excimer laser pulses (248 nm) at a frequency of 30 Hz and each pulse had 800 mJ of energy.

Film thickness and uniformity would be measured on the fused silica fibers once the thin-film crystalline structure is verified. The most important property is the uniformity of the Dy:YAG coating at the fiber core and film interface, since this is where the pump and emission light interacts. Eventually, PLD coated thin film fibers would be tested for

durability in harsh combustion and turbine environments. Figure 3.8 shows the diffraction pattern of the deposited thin film. The film is amorphous—it has no crystalline structure. A chemical vapor deposition (CVD) of YAG thin film requires 1100°C substrate temperature according to Bai [1994]. Since the substrate heater was only capable of heating up to 750°C, this explains why the film is amorphous because the substrate does not have enough crystallization energy to from the YAG structure.

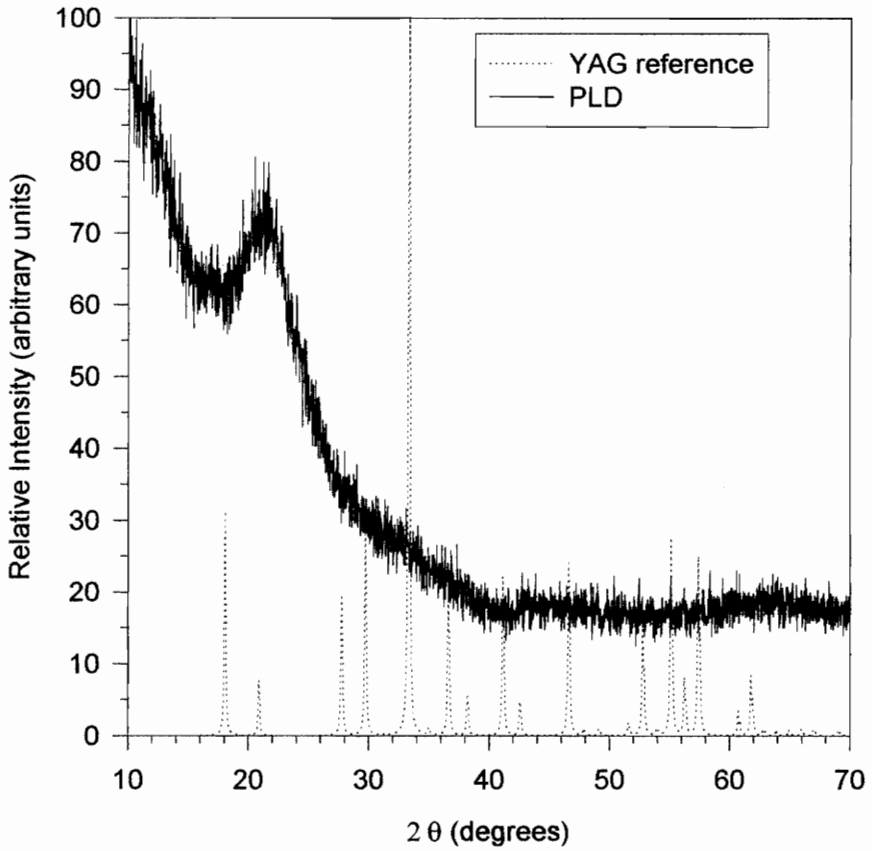

Figure 3.8: XRD comparison of YAG thin film pulsed laser deposition (PLD) with reference

In an attempt to modify the structure the substrate was annealed (placed in an oven at 1100°C for 3 hours) to see if the film converted to the more stable YAG structure. Figure 3.9 reveals a few peaks showing some crystalline features, but it does not match the YAG reference pattern. It is concluded that a much hotter heater is needed for the PLD of the Dy:YAG thin film.

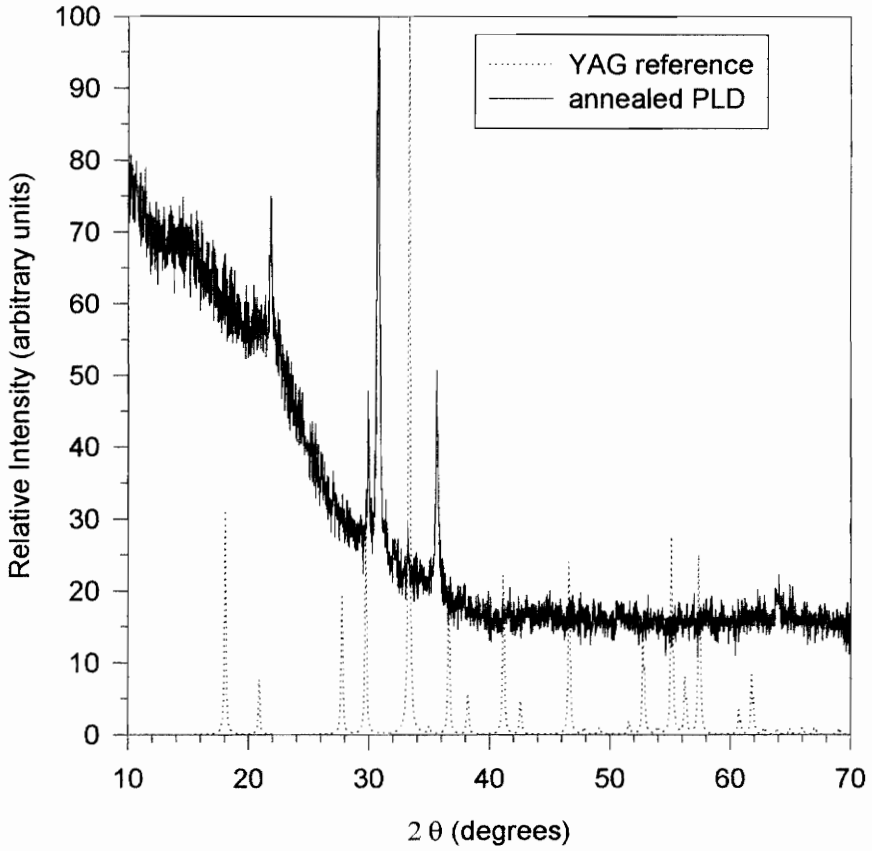

Figure 3.9: XRD comparison of annealed YAG thin film with reference

3.1.2 PRECIPITATION REACTION

The solid-state synthesized Dy:YAG was not identical to the reference YAG crystal. Therefore, a precipitation reaction was used to synthesize the Dy:YAG crystal. Instead of 3 mole %, 2 mole % of the dysprosium activator was used. This was done following Shokai Yang's (MSE department at Virginia Tech) suggestion to strengthen the phosphorescent emission signal, he has worked with Dy:YAG and its emission properties in the past. The following equations represent the mole ratios for the 2 mole %:

$$\text{Dy:}Y_3Al_5O_{12}\ (2\ \text{mole \% Dy})$$

$$= (Dy_{0.02}Y_{0.98})_3Al_5O_{12}$$

$$= (Dy_{0.06}Y_{2.94})Al_5O_{12}$$

The precipitation reaction required the following molar proportions:

$$0.06Dy_2O_3 + 2.94Y_2O_3 + 10Al(NO_3)_3 \bullet 9H_2O + xH_2O + yHNO_3 + zNH_4OH$$
$$\rightarrow 0.12Dy(OH)_3\downarrow + 5.88Y(OH)_3\downarrow + 10Al(OH)_3\downarrow + \cdots$$
$$\xrightarrow{\Delta} 1.96(Y_3Al_5O_{12}):0.12Dy + \cdots$$

Appendix A lists the raw materials and synthesis details. The Dy:YAG synthesis is not very sensitive to the number of moles of deionized water (x), nitric acid (y), and ammonium hydroxide (z). Only enough of each (x, y, and z) was needed to dissolve the powders and change the solution's pH respectively. The precipitate was fired in a furnace to produce the final Dy:YAG powdery product.

An X-ray diffraction pattern was measured for the synthesized powder. Figure 3.10 compares the reference and synthesized YAG patterns. Every major intensity peak for the Dy:YAG has a matching reference peak at the correct diffraction angle. The relative intensity of some of the peaks is not an exact duplicate of the reference's, but the diffraction pattern confirms successful synthesis of the YAG crystalline structure.

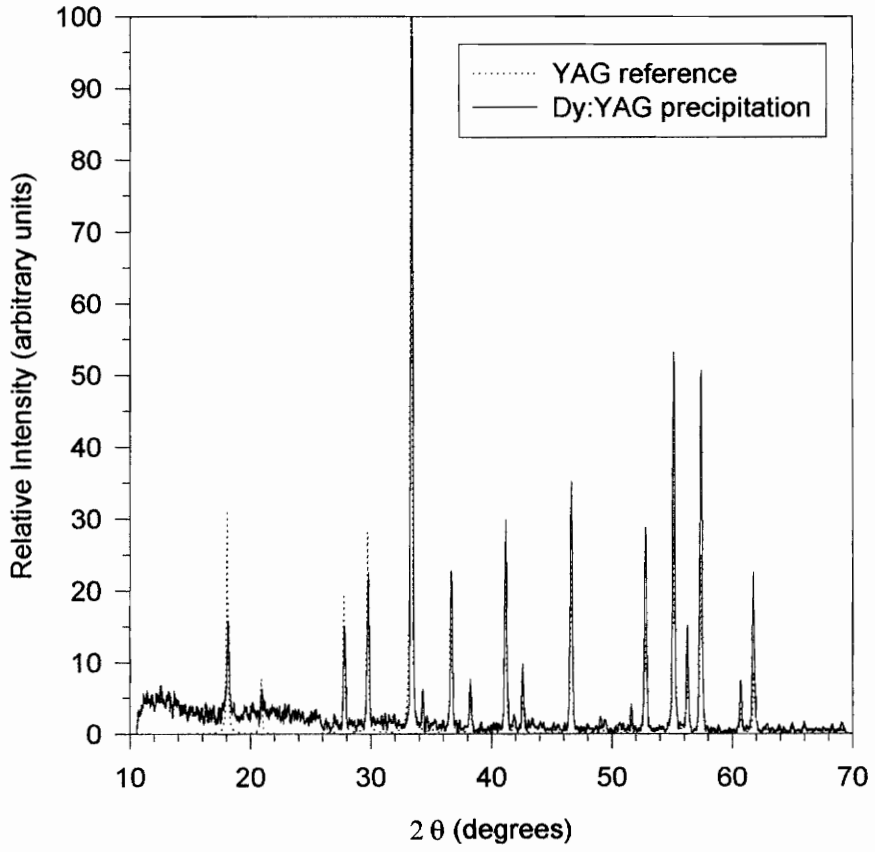

Figure 3.10: XRD comparison of Dy:YAG precipitate with reference

The sample Dy:YAG was tested for its phosphorescent emission spectrum, which was measured with an emission spectrometer. The spectrometer utilizes two monochromators, one to filter an arc lamp's wavelength used to excite the sample and another to measure the sample's emission spectrum. Figure 3.11 shows the emission spectrum for the Dy:YAG excited at 254 nm (ultraviolet light). The spectrum is not the same as the one of Goss, et al [1989] in Figure 3.12. The difference results from a using a 254 nm versus a 355 nm excitation radiation.

The sample was also excited at 355 nm (same wavelength as the tripled output of a Nd:YAG laser) to compare with Goss's reference spectrum, and Figure 3.13 contains the emission spectrum. The spectrum is not identical to Goss's, however, the synthesized Dy:YAG crystals are the same structure as the reference (confirmed by the XRD analysis).

The excitation wavelength was changed to 308 nm, matching the wavelength of the XeCl excimer laser available in the Reacting Flows Laboratory (ME department, VA Tech). The 308 nm wavelength was examined because the experimental setup utilizes the excimer laser to excite the phosphor coated fibers. Figure 3.14 contains the emission spectrum. None of the recorded emission spectra match Goss's, but the F-level phosphorescence is similar for all the emission spectra; all have a strong peak near 500 nm with a relative intensity of around 90 %. The F-level emission ranges from about

495-505 nm and is the temperature independent emission band. The G-level emits approximately in the 440-470 nm wavelength range and its emission intensity is directly proportional to temperature. If the F-level emission remains independent of temperature, the F and G level intensity ratio can be used to measure temperature.

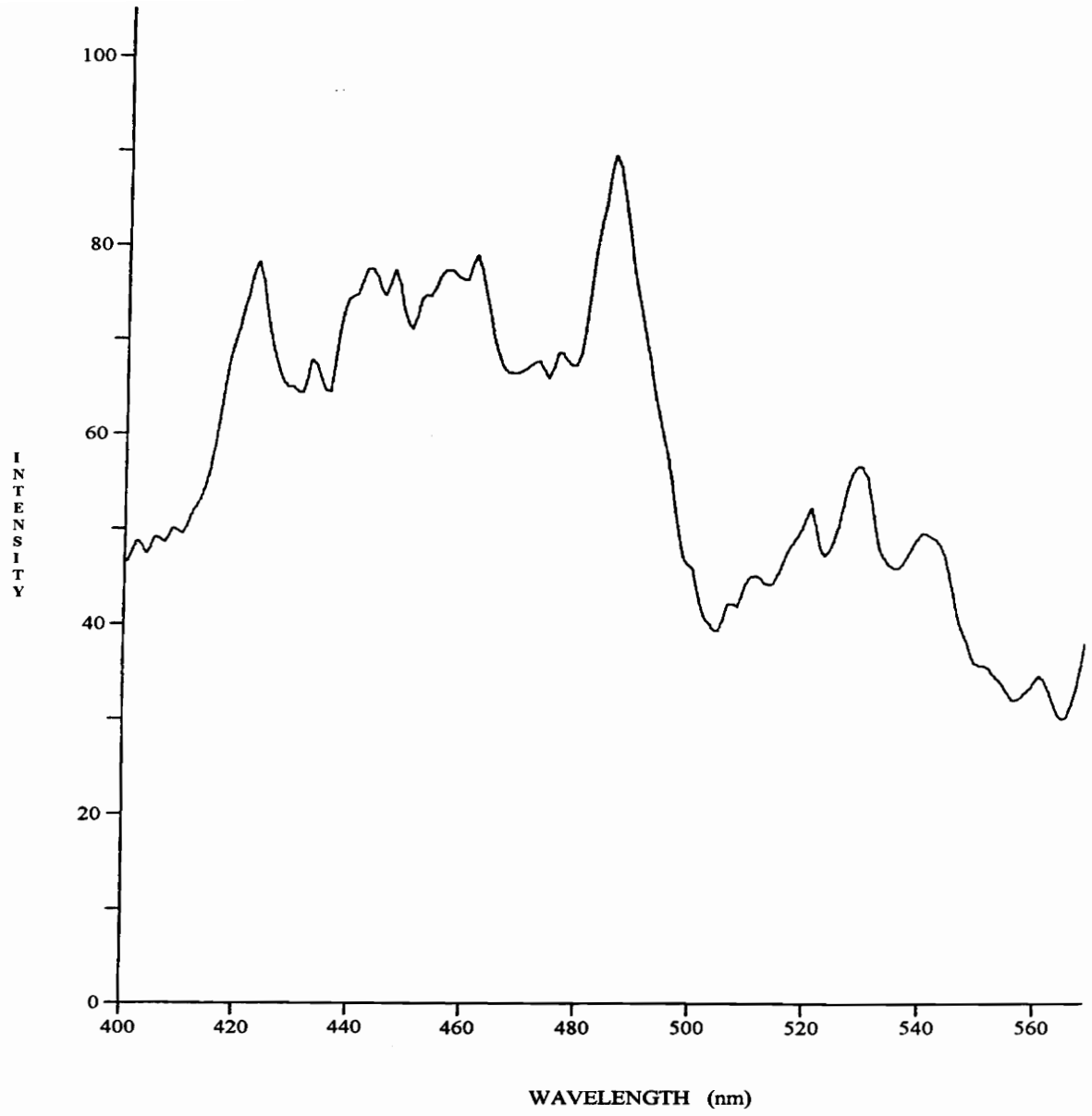

Figure 3.11: Dy:YAG emission spectrum, 254 nm excitation (monochromator)

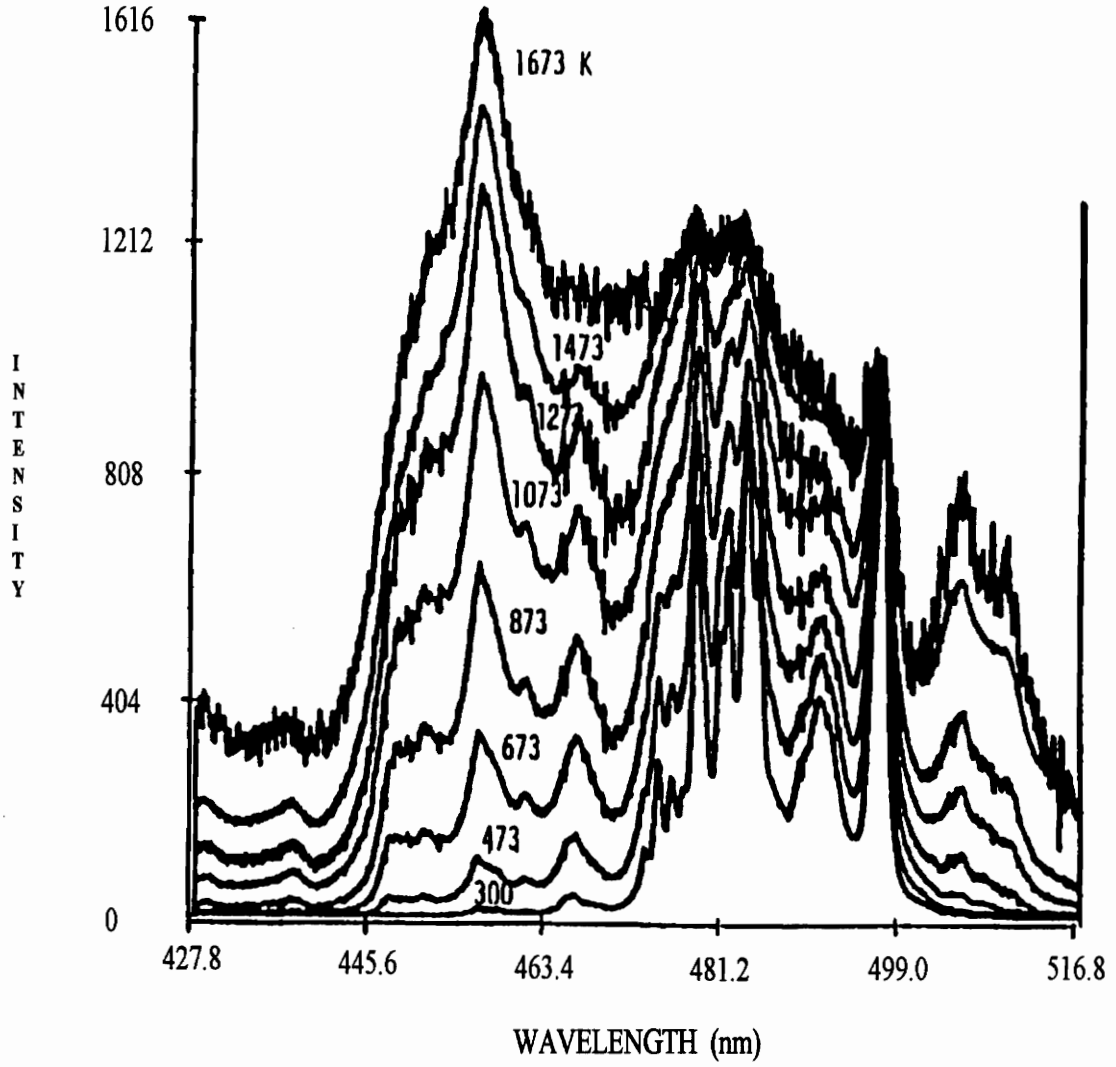

Figure 3.12: Dy:YAG emission spectrum, 355 nm excitation (tripled Nd:YAG laser) temperature dependent intensity variation also included (Goss, et al. [1989])

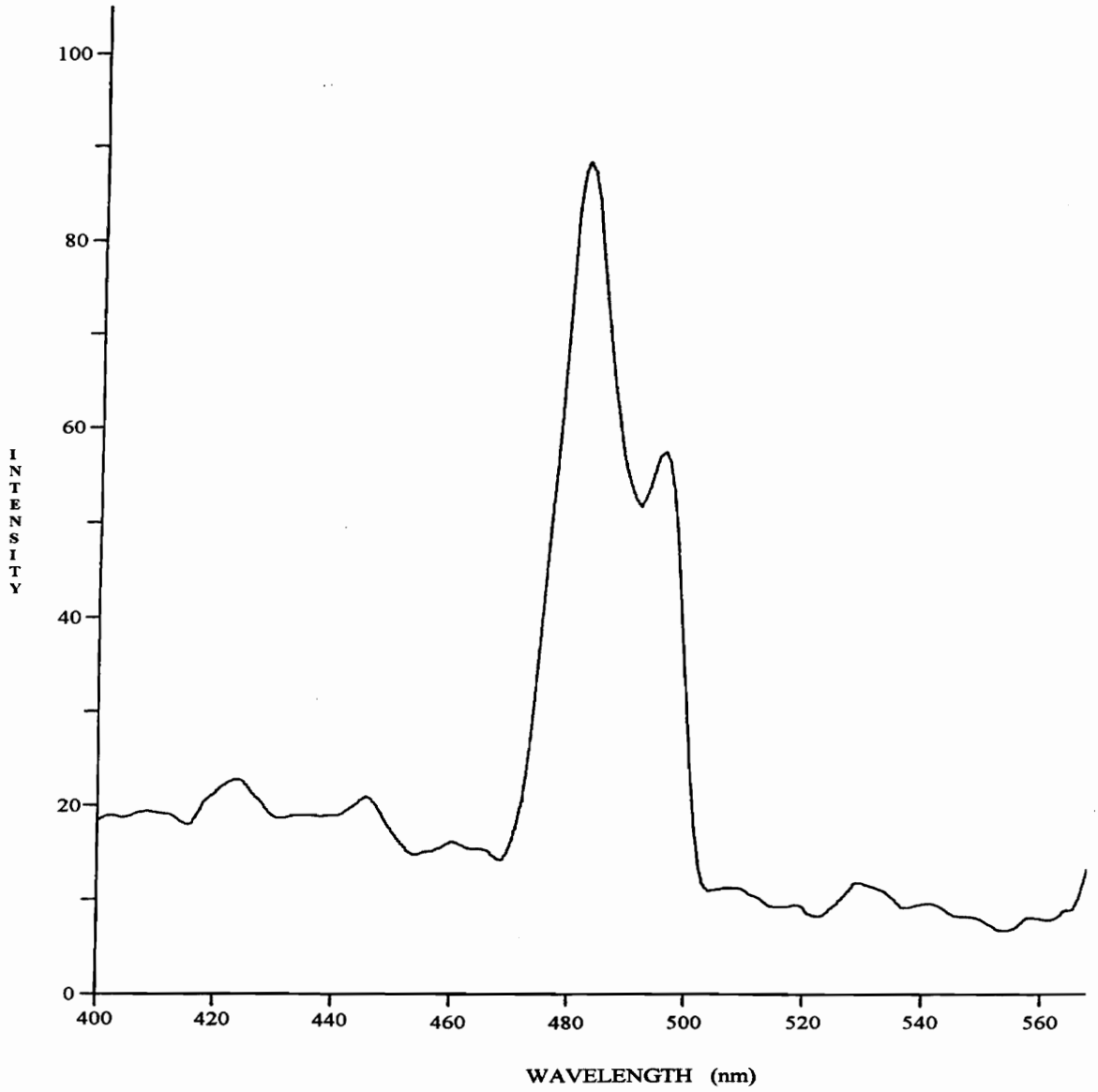

Figure 3.13: Dy:YAG emission spectrum, 355 nm excitation (monochromator)

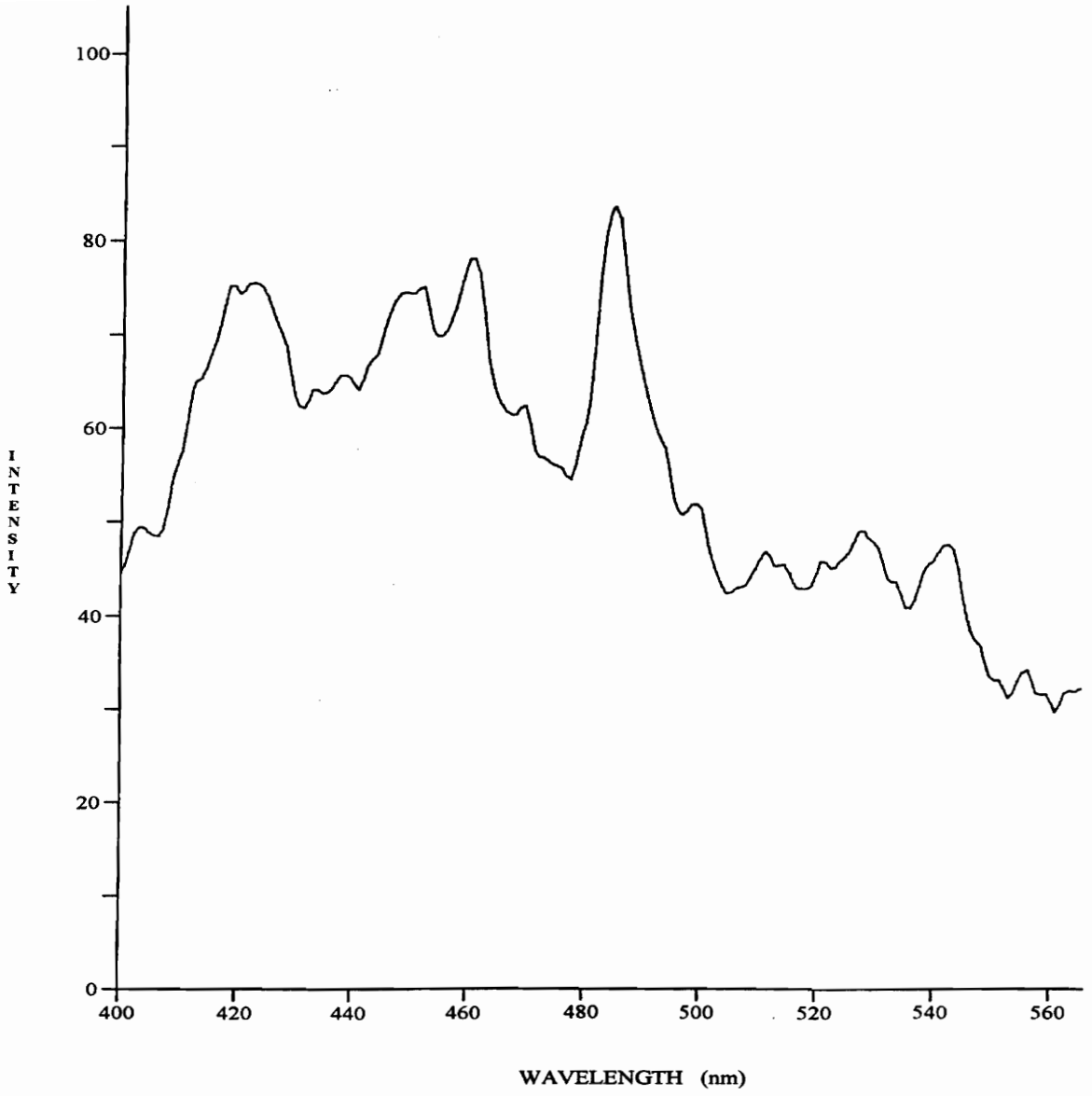

Figure 3.14: Dy:YAG emission spectrum, 308 nm excitation (monochromator)

3.1.3 SLURRY DEPOSITION FIBER COATING

The Dy:YAG thick film slurry coated fibers were used in the proof of concept experiments. A slurry thick film deposition technique was used to coat the fibers since the pulsed laser deposition method did deposit a thin film of Dy:YAG onto the substrate (the film was an amorphous mixture of the dysprosium, yttrium, aluminum, and oxygen constituents). Appendix B lists the raw materials and synthesis details.

Figure 3.15 compares the diffraction pattern of the Dy:YAG thick film slurry with the YAG reference. The slurry pattern is nearly identical to the Dy:YAG precipitate except for the relative intensity between the peaks is about ten compared with zero for the reference. The slurry is amorphous between the YAG crystals due to solvent and binder residue remaining in the thick film. The diffraction pattern shows the amorphous nature of the thick film (the upward shift of the relative intensity in between the peaks).

3.2 EXPERIMENTAL DESIGN AND PROCEDURES

The experimental apparatus was designed to test the proof of concept Dy:YAG coated fiber-optic temperature sensor. Validating the remote sensing nature of an optical fiber sensor coated with the Dy:YAG thermographic phosphor was the main objective. The remote nature of the sensor was validated by distinguishing a visible emission signal from unwanted background noise in a prototype fiber-optic sensor. The prototype design was a

fused silica fiber coated with a Dy:YAG thick film. The pump laser energy and emission signal were guided to and from the thermographic phosphor with the optical fiber. The experiments examined both the fiber/Dy:YAG evanescent wave coupling and external pumping signal strengths by exciting the Dy:YAG coated fibers with a UV laser and measuring the visible emission.

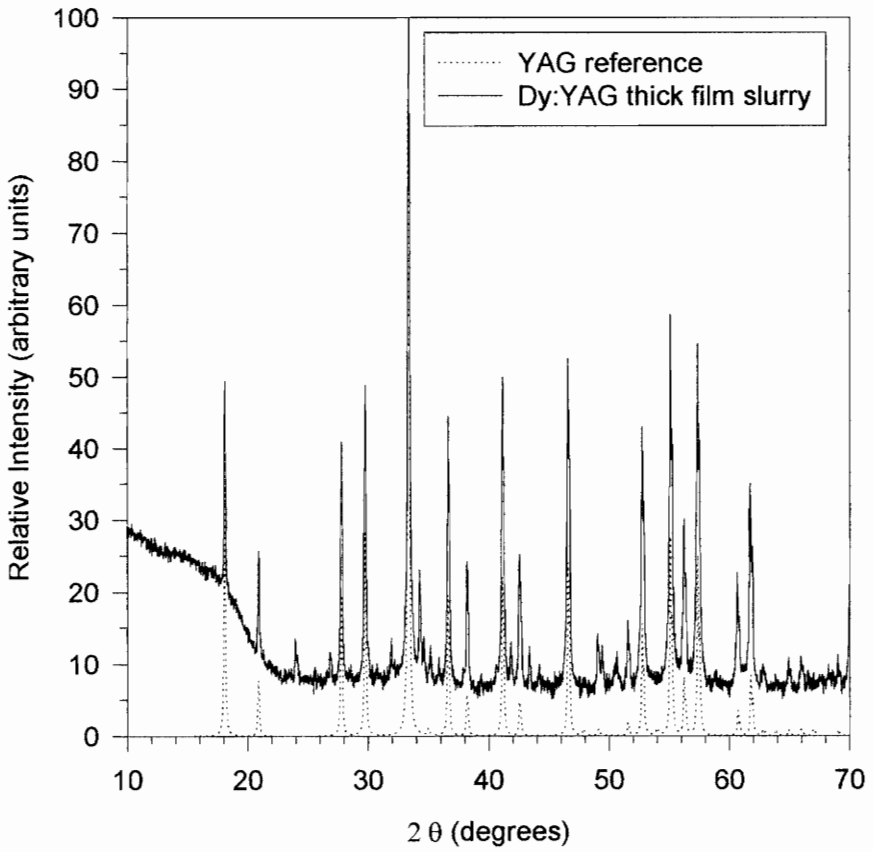

Figure 3.15: XRD comparison of Dy:YAG thick film slurry with reference

Figure 3.16 shows the experimental schematic for testing the evanescent wave coupling of the sensors. The schematic for the external pumping of the sensors is illustrated in Figure 3.17.

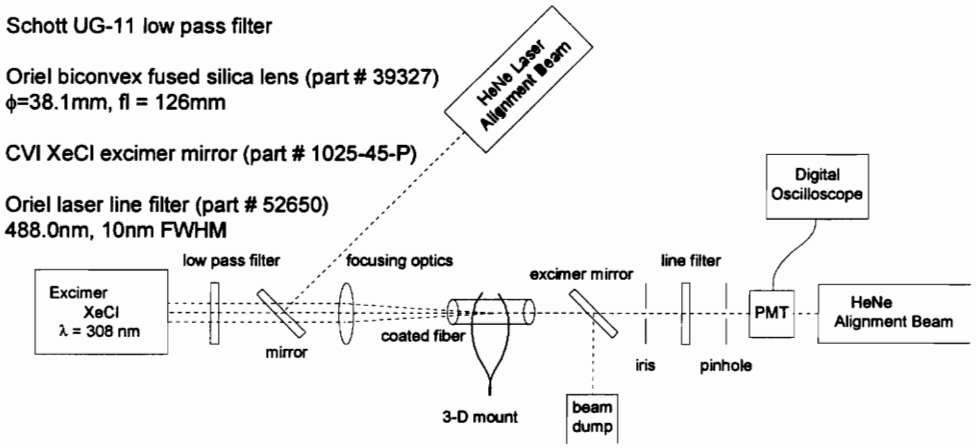

Figure 3.16: Experimental schematic for testing evanescent wave coupling

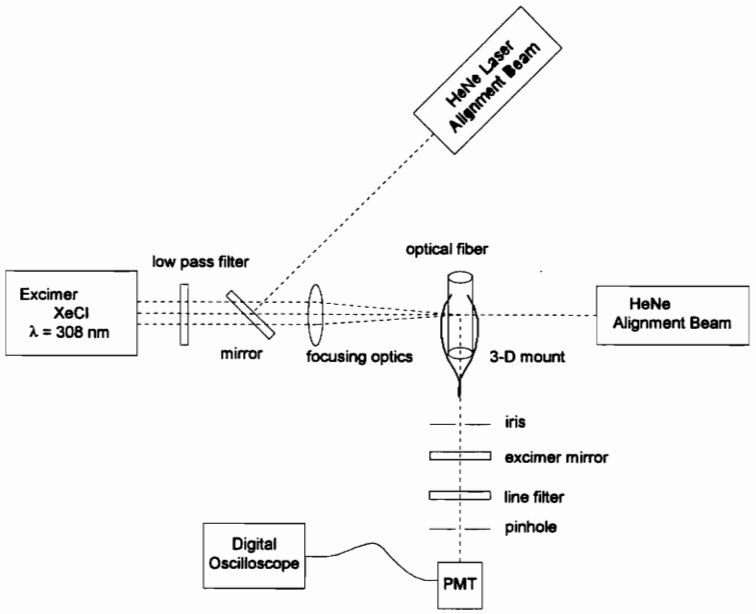

Figure 3.17: Experimental schematic for testing external pump source

3.2.1 LASER AND OPTICS

The Excimer laser used was a Lumonics TE-861T-4 gas laser filled with xenon (Xe) and chloride (Cl) gas and its emission wavelength was 308 nm with a 6 x 33 mm collimated rectangular beam. Due to visible emission when the lasing gases are running low in the laser, a Schott UG-11 glass filter (essentially a low pass filter) passed the 308 nm radiation and filtered the visible. The beam was focused onto the optical fiber with an Oriel biconvex fused silica lens (lens # 39327: ϕ = 38.1 mm, f.l. = 126 mm, F/# = 3.3).

3.2.2 PROTOTYPE SENSOR

Two types of sensors were constructed and tested. One was a 3M FP-600-LHT optical fiber 5.08 cm (2") long. The fiber was stripped down to its 600 μm fused silica core and 5.08 cm strips were measured and cut to size with a diamond scribe. The ends were polished smooth for greater coupling efficiency into and out of the fiber. A second sensor was constructed using a 2 mm diameter fused silica rod. The rods were scribed to length and polished like the smaller diameter sensor. The rod was purchased from the chemistry store at Virginia Tech. The Dy:YAG was deposited onto the fibers using a thick film slurry technique (the directions for making the film are in Appendix B). The prototype sensor was held in place using tweezers, and a three-dimensional set of linear stages were used to align the sensing element and focused excimer laser beam. The sensor was placed 160 cm beyond the focusing lens so the high energy density from the laser would

not shatter the sensor. The HeNe lasers and the accompanying mirror were not used during test measurements but were only used to align the laser, optics, filters, detector, and sensor.

3.2.3 DETECTION OPTICS

The visible emission signal was filtered before entering the photo-multiplier tube (PMT). The source excimer radiation was reflected using a CVI XeCl excimer mirror (part #: 1025-45-P). The mirror reflects the excimer laser radiation and passes light in the visible emission range. An iris and cylindrical light shield were used to block any unwanted light from reaching the PMT. Because 490 nm is the strongest emission peak from the Dy:YAG at room temperature, an Oriel laser line filter (part # 52650: 488.0 nm, 10 ± 2 nm FWHM) was used to pass the emission signal and block the noise. The pinhole protected the PMT from being by a combination of the emission signal, laser radiation, and other light sources present in the room.

The photomultiplier tube was a RCA 1p28, 9-stage, side-on PMTs and was snubbed with a 50 ohm resistor on the end of an eight inch cable attached in parallel with the coaxial cable running from the PMT to the digital oscilloscope. The snubbing procedure cut down on the fall time reading of the PMT for use in fast applications, i.e., photon counting. A Pacific Instruments model 204 high voltage power supply was used for the PMTs.

3.2.4 DIGITAL OSCILLOSCOPES

A Nicolet 4094C & 4175 combination and Tektronix TDS 684A digital oscilloscope recorded the emission signals measured by the PMT. The Tektronix scope was used primarily for its high speed sampling rate to examine the Nicolet results. Appendix F contains the data transformation codes and file format changing programs.

All of the data recorded with the Nicolet scope was sampled at 20 nanoseconds per point, while the data was sampled at 20 picoseconds per point with the Tektronix digital oscilloscope. The full scale scope settings were test specific and are specified in the results section.

4.0 RESULTS AND DISCUSSION

Experiments were used to examine two different coupling techniques to see if the proof of concept optical thermal sensor would work. One method was the evanescent wave coupling discussed earlier in the literature review section and the other employed/used external pumping of the thick film coated fibers. The external excitation should produce a stronger phosphorescent signal because all of the laser energy is absorbed by the Dy:YAG compared to a small percentage in the evanescent wave coupling method. The following sections discuss the results.

4.1 EVANESCENT WAVE COUPLING

4.1.1 600 μm DIAMETER FIBER

The small diameter fiber (ϕ = 600 μm) was tested first to see if the evanescent coupling would excite the phosphor. Figure 3.16 shows the schematic for the evanescent coupling measurements. The HeNe lasers and accompanying mirror were not present during the test runs. Baseline laser signal measurements were taken to compare with the coated fiber signal measurements and experiments only used the low pass filter when specified.

Measurements were taken with a Nicolet digital oscilloscope, which was set at 100 mV full scale, and a PMT where the power supply was set at 800 V. All of the following plots are an average of 10 cases. Each test run recorded 225 data points with a sampling

rate of 20 nanoseconds per data point. The oscilloscope was triggered when it received the synchronized output signal from the laser when it lased. The laser pulse itself was approximately 10 ns long.

Figures 4.1, 4.2, and 4.3 contain the plots for the visible emission for the three different Dy:YAG coated fibers. The jagged pattern of the plots are caused by a ringing effect (also known as a "pulse shape distortion", Burle [1980]). The ringing results from the signal reflections in the 8 inch snubbing coaxial cable, and can be eliminated by finding the correct length for the snubbing coaxial cable so that the reflections interfere destructively. All of the plots show this ringing effect. A baseline comparison is given by the bare fibers in Figures 4.4, 4.5, and 4.6. The signal strength is slightly stronger for the uncoated fibers and is due to a stronger laser signal causing the line filter to fluoresce. The double peak (or high frequency ringing) on the plots results from the PMT base not being wired for measurements in the nanosecond range. The coated fibers could have a stronger signal but the scope only captures about five points for the entire visible emission signal. The Tektronix scope shows how a greater number of averages and finer time resolution are better at capturing the event. This is discussed in a later section. Figure 4.7 contains the plot for the laser signal. This signal is as strong as the signal for the coated and uncoated fibers, which confirmed the line filter fluorescing problem.

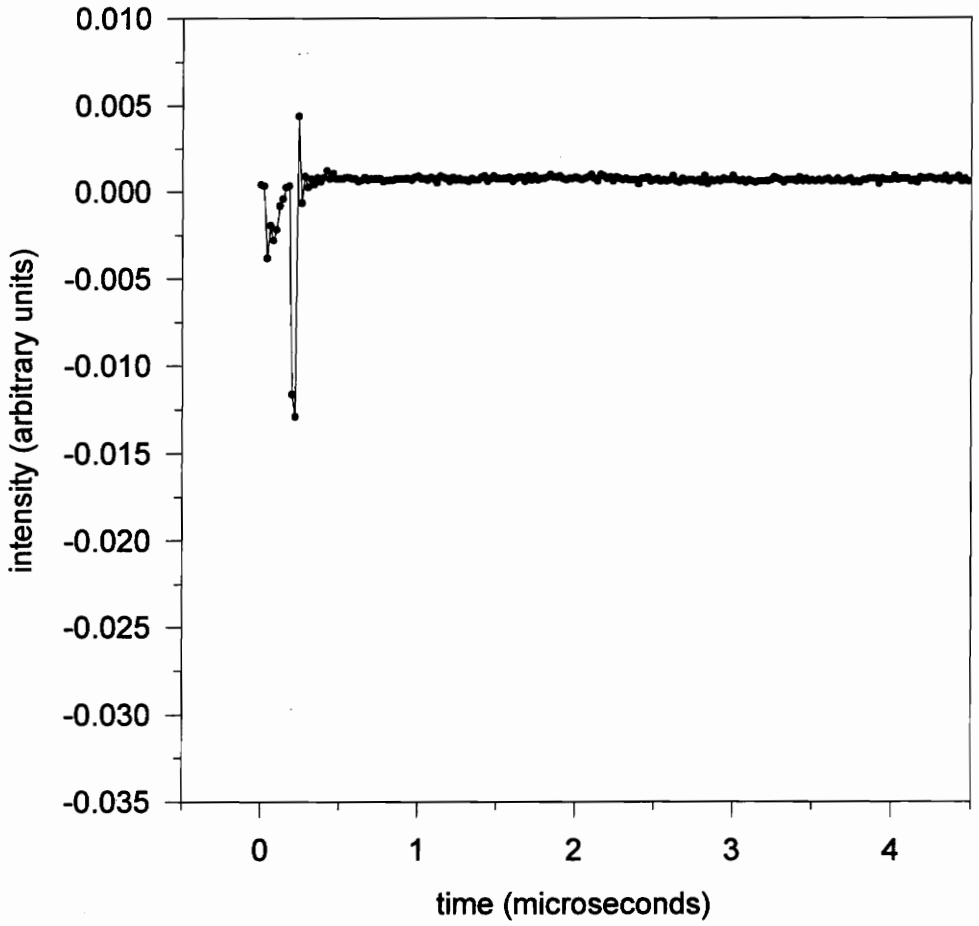

Figure 4.1: Dy:YAG coated fiber #1 (ϕ = 600 μm) waveguided excimer illumination Nicolet oscilloscope

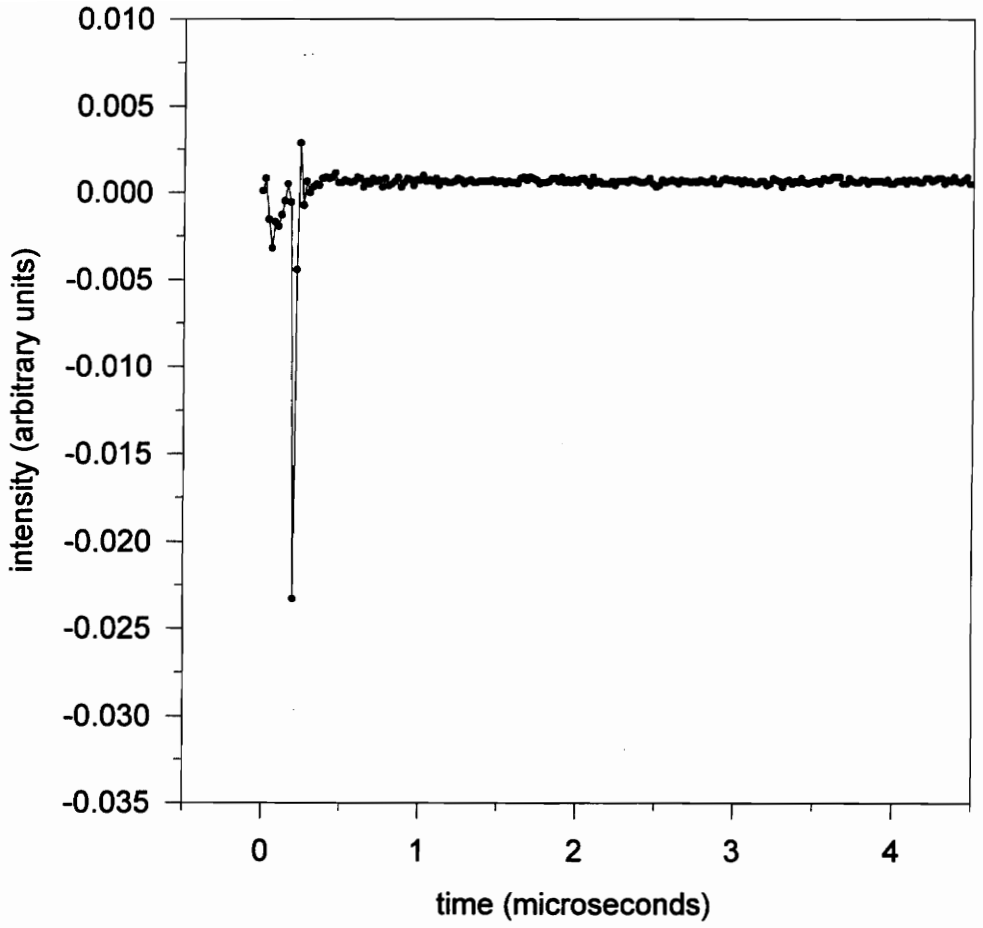

Figure 4.2: Dy:YAG coated fiber #2 (ϕ = 600 μm) waveguided excimer illumination Nicolet oscilloscope

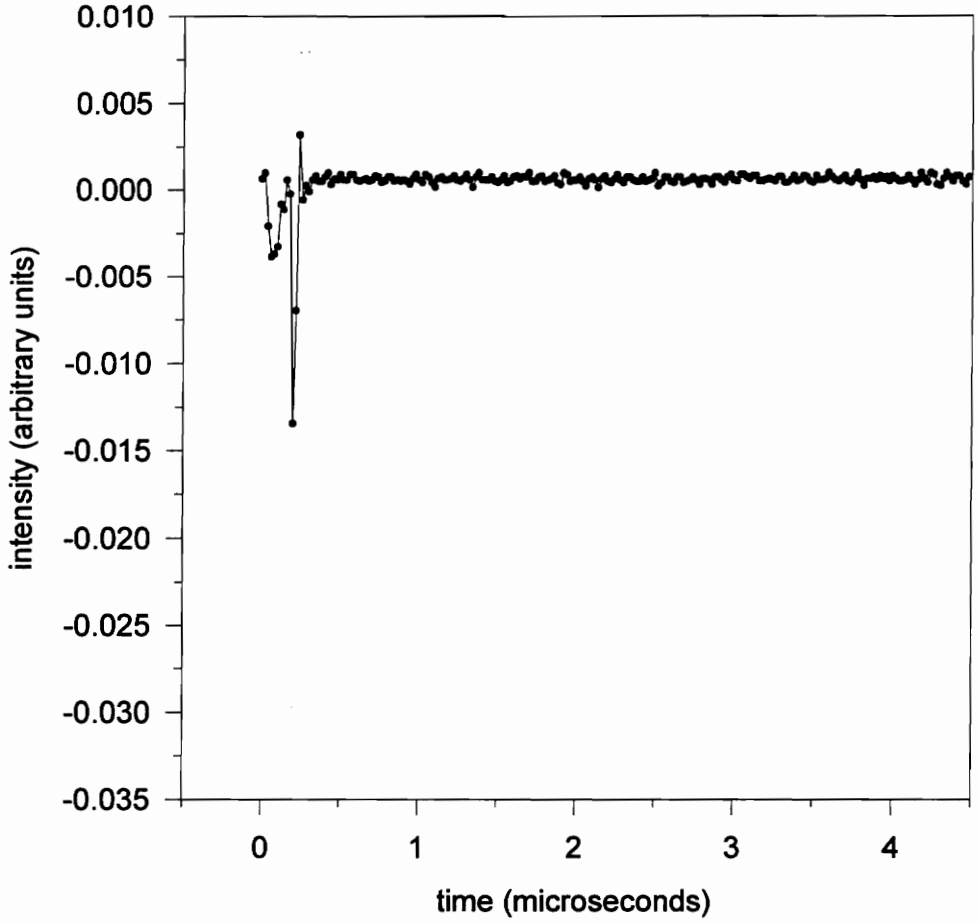

Figure 4.3: Dy:YAG coated fiber #3 (ϕ = 600 μm) waveguided excimer illumination Nicolet oscilloscope

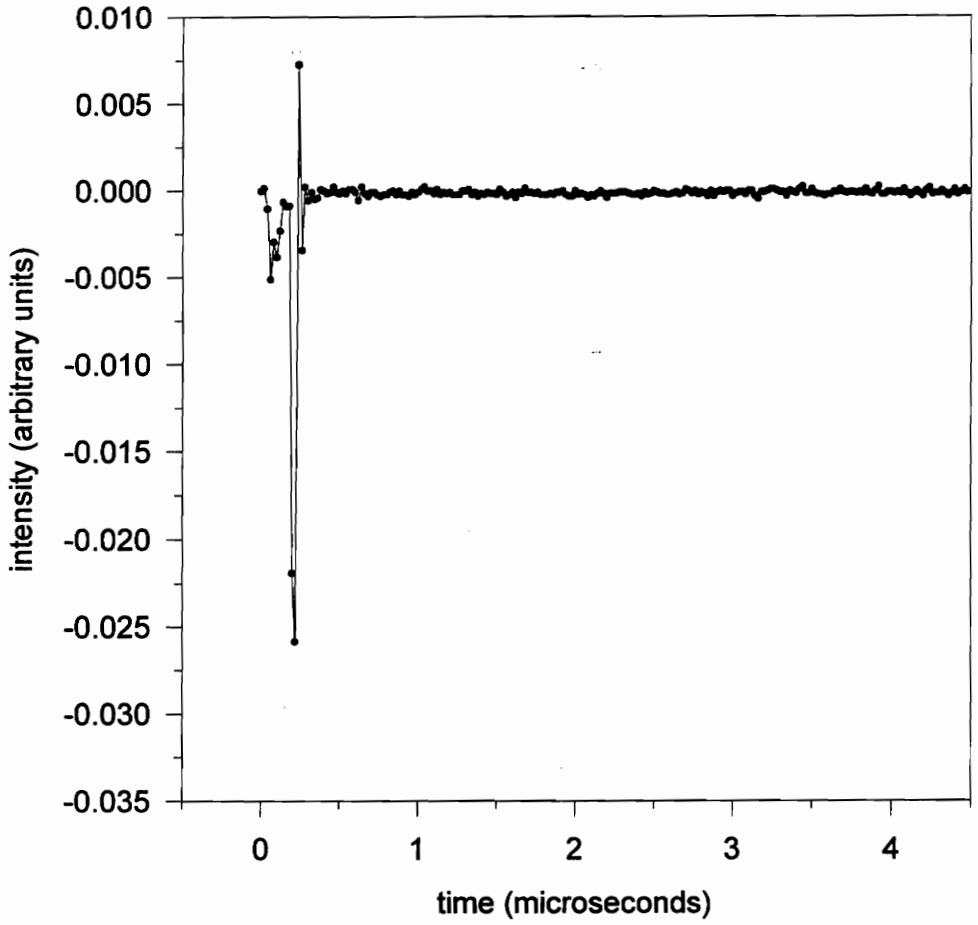

Figure 4.4: Bare fiber #1 (ϕ = 600 μm) waveguided excimer illumination Nicolet oscilloscope

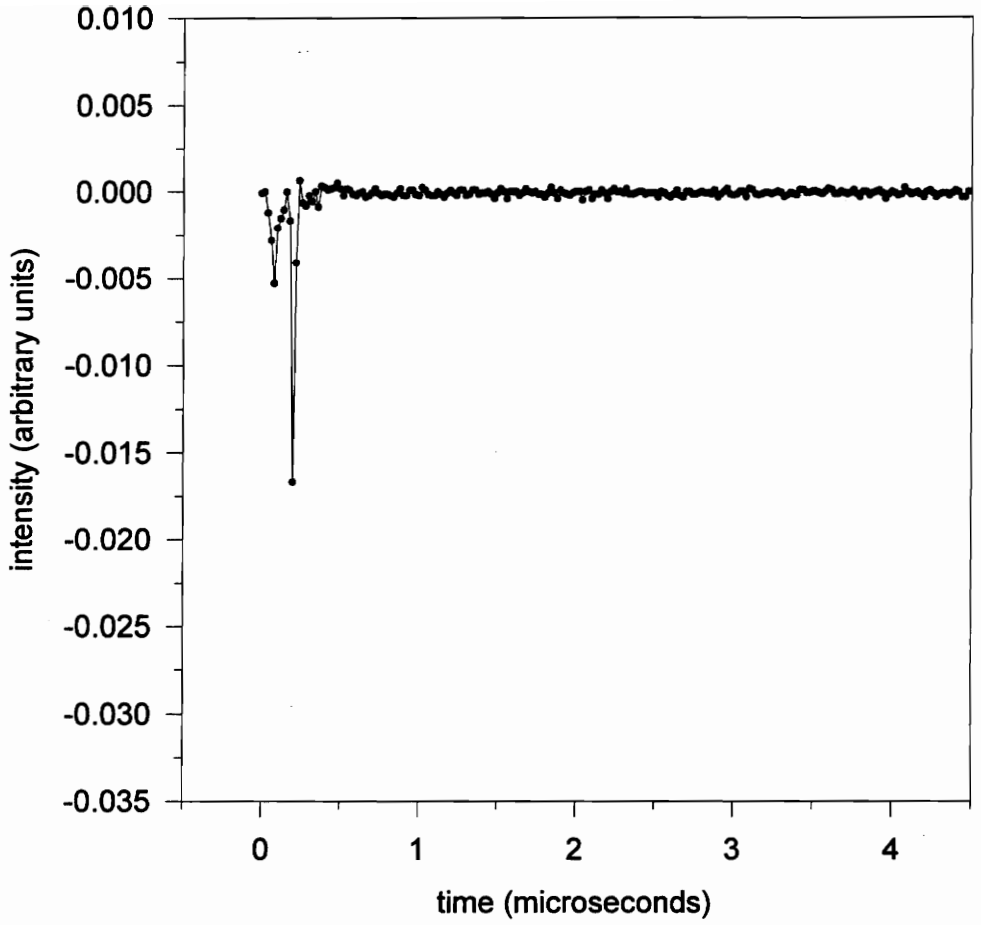

Figure 4.5: Bare fiber #2 (ϕ = 600 μm) waveguided excimer illumination Nicolet oscilloscope

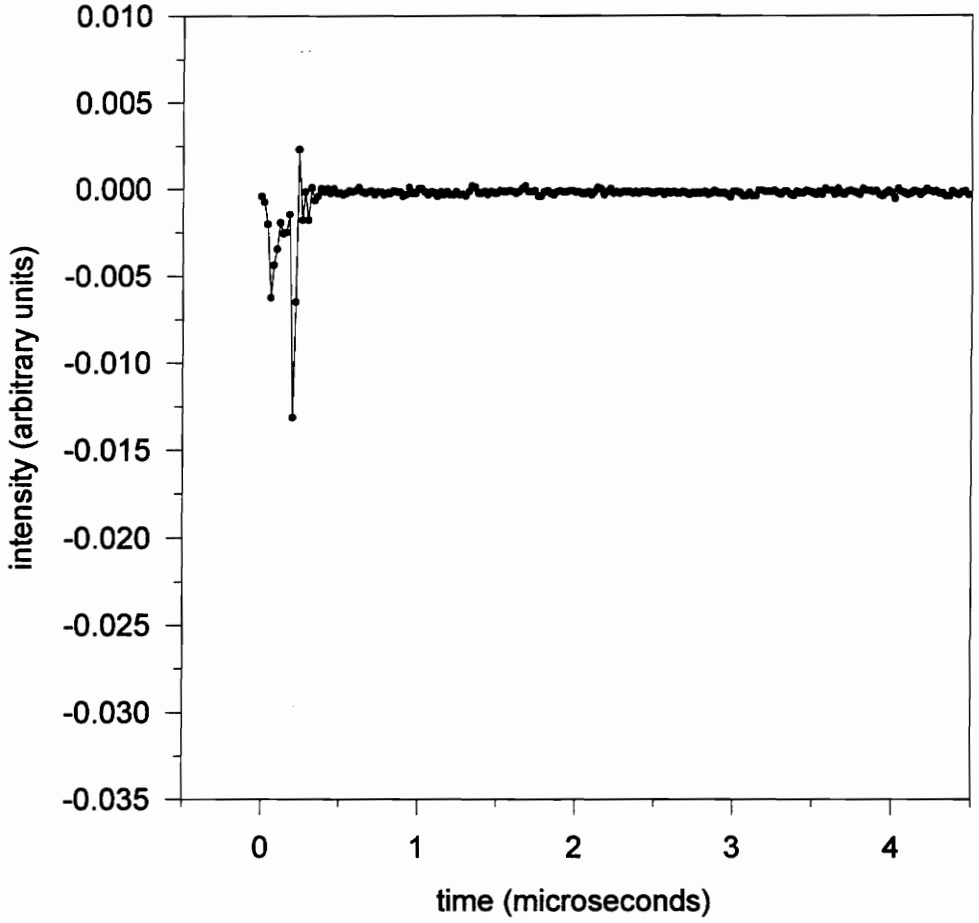

Figure 4.6: Bare fiber #3 (ϕ = 600 μm) waveguided excimer illumination Nicolet oscilloscope

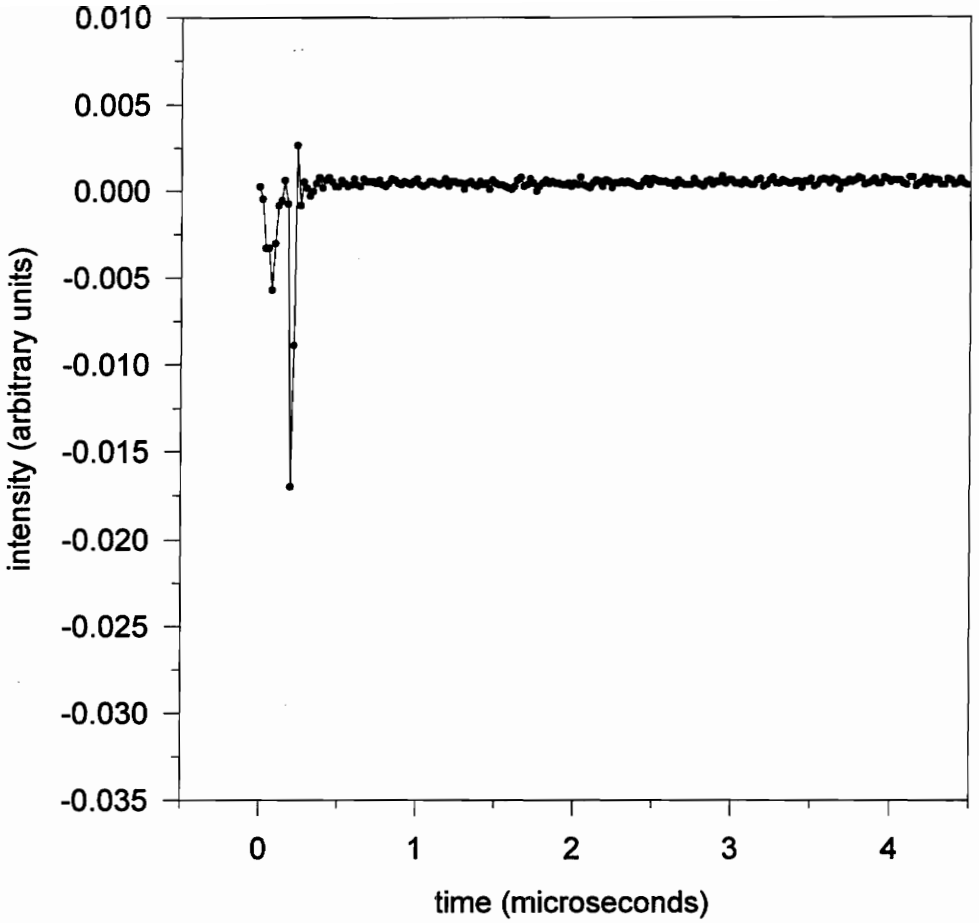

Figure 4.7: Excimer illumination
PMT setting for $\phi = 600$ μm fiber
Nicolet oscilloscope

4.1.2 2 mm DIAMETER SILICA ROD

A large diameter fiber was tested next to see if the evanescent coupling would excite the phosphor for a larger fiber (ϕ = 2 mm). The large diameter was expected to produce a stronger phosphorescence due to a higher number of guided modes penetrating deeper into the thick film coating. It was hoped the stronger signal would eliminate the noise problem (bare fiber signal stronger than coated fiber) found in the smaller diameter evanescent test cases.

The Nicolet digital oscilloscope was set at 100 mV full scale and the PMT power supply was set at 600 V. All of the following plots are an average of 10 cases. The oscilloscope triggering and data sampling rate were the same as in the small diameter case.

Figure 4.8 shows the visible emission for a thick film coated fiber. The bare fiber comparison is in Figure 4.9. The intensity is nearly triple for the bare fiber case with no Dy:YAG present. The fluorescence from trace impurities within the fiber produces the stronger signal. The excimer beam signal is shown in Figure 4.10. This plot confirms that impurities in the fiber were responsible for the noise. If more intense radiation caused the line filter to fluoresce, then the signal would be the strongest for the bare laser case. All of the large diameter fiber plots exhibit the ringing and double hump phenomena as discussed for the smaller diameter fibers.

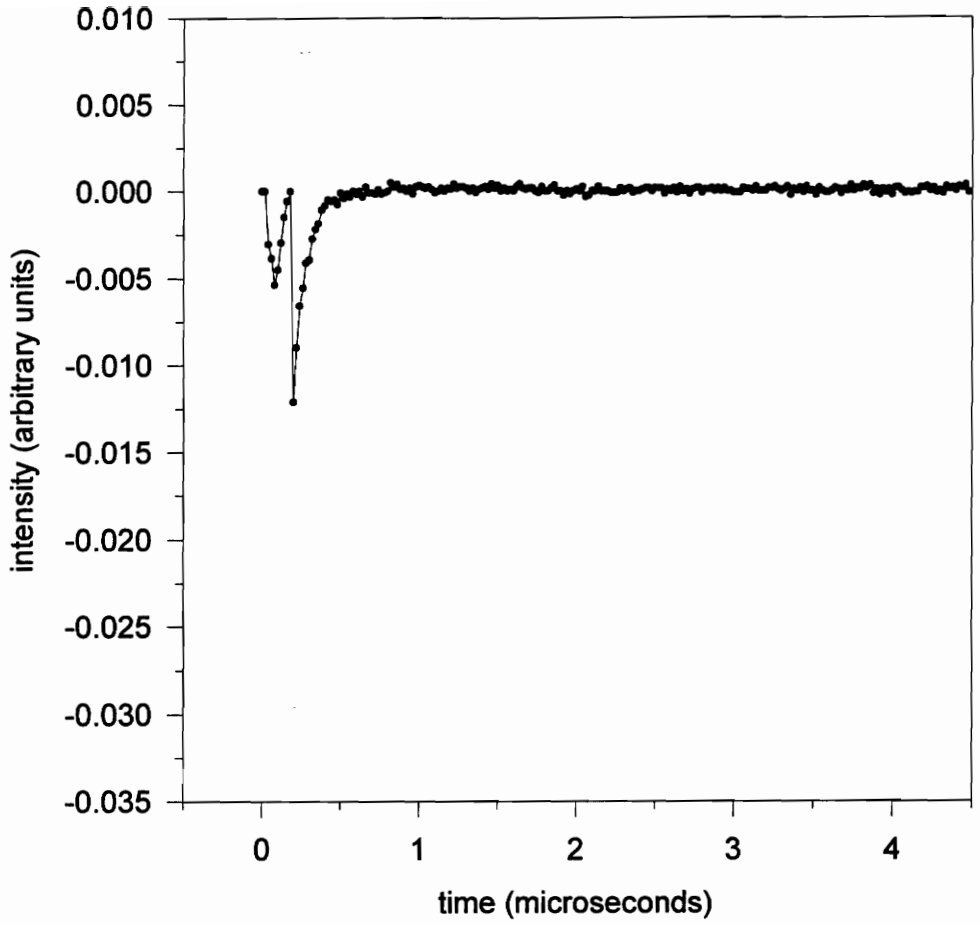

Figure 4.8: Dy:YAG coated fiber (ϕ = 2 mm) waveguided excimer illumination Nicolet oscilloscope

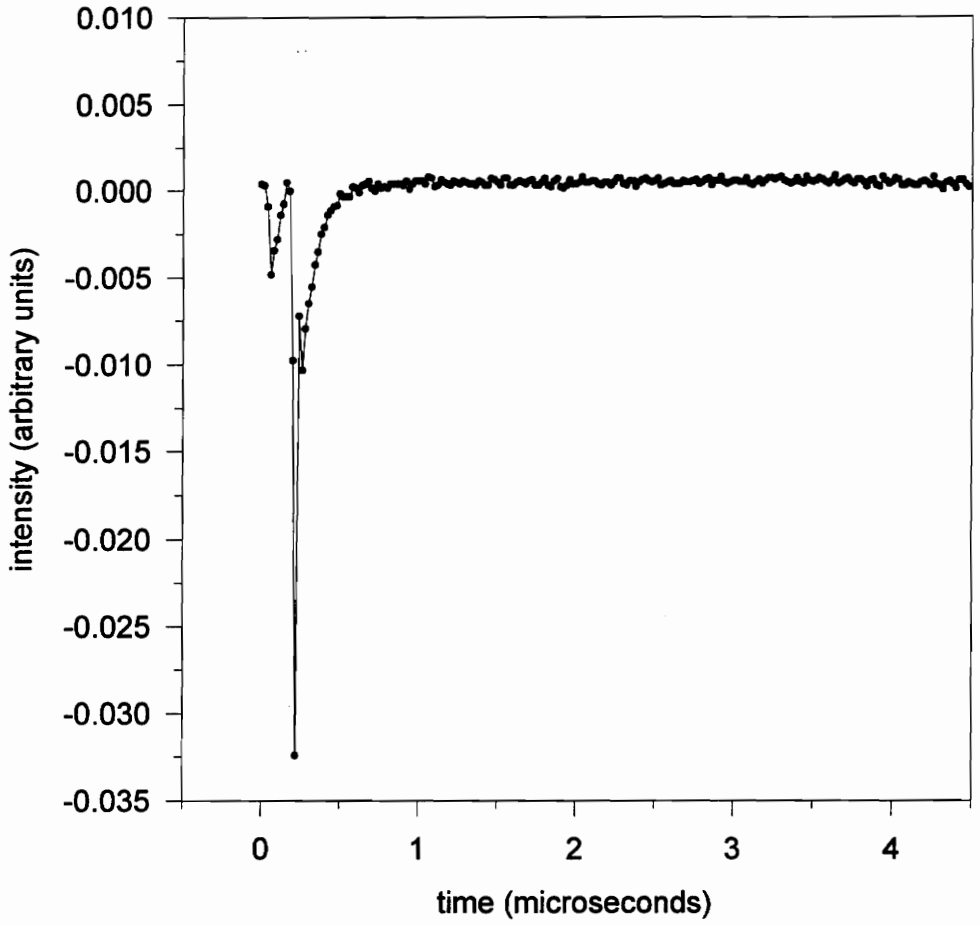

Figure 4.9: Bare fiber (ϕ = 2 mm) waveguided excimer illumination Nicolet oscilloscope

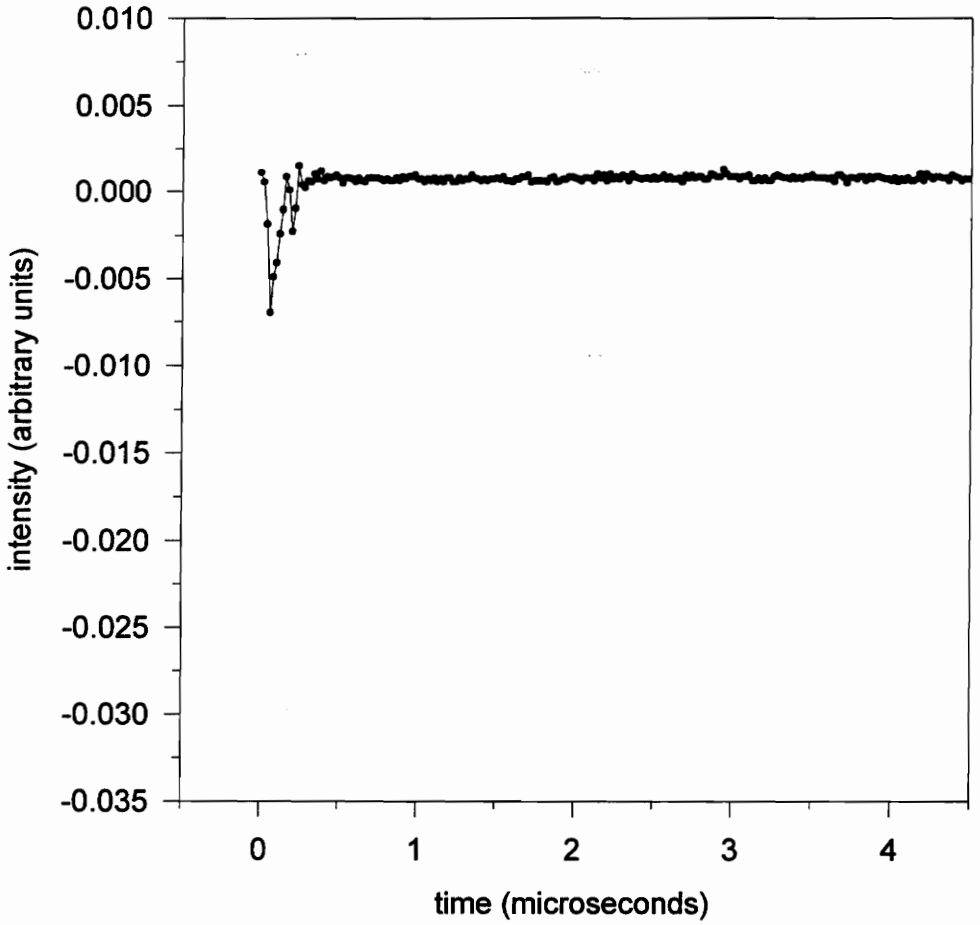

Figure 4.10: Excimer illumination
PMT setting for $\phi = 2$ mm fiber
Nicolet oscilloscope

4.2 EXTERNAL PUMPING

The noise was greater than the Dy:YAG phosphorescent emission signal for the evanescent cases, which does not support the proposed optical thermal sensor concept. The fibers were next tested with an external illumination/pumping source as shown in Figure 3.17. The external illumination (pumping) of the Dy:YAG coated fibers were expected to produce the strongest possible signal because all of the laser radiation pumps the phosphor. The laser signal measurement cases were the same as the others except they do not have an optical wave guide to pass the beam through. The experiments only used the low pass filter when specified.

4.2.1 2 mm DIAMETER SILICA ROD

A large diameter fiber (ϕ = 2 mm) was examined to test the external phosphor illumination. The large diameter was expected to produce the strongest phosphorescence due to the greater area of the thick film Dy:YAG coating. It was hoped the stronger signal would eliminate the noise problem (bare fiber signal stronger than coated fiber) found in the smaller diameter evanescent test cases.

The Nicolet digital oscilloscope was set at 100 mV full scale and the PMT power supply at 700 V. All of the following plots are an average of 20 cases. Each test run recorded 225 data points with a sampling rate of 20 nanoseconds per data point. The oscilloscope

was triggered when it received the synchronized output signal from the laser when it lased.

Figures 4.11. and 4.12 compare the coated and bare fiber for the external laser pumping. The signal intensity for both cases is nearly identical. Figures 4.13 and 4.14 compare the same case as above, except the laser is filtered with a low pass filter (Schott UG-11 filter) to block any visible noise from the laser. The bare case is more intense. This is a result of more of the UV radiation causing the line filter to fluoresce. The experiment was checked to see if the fused silica lens was fluorescing and the results are shown for the coated and bare fibers in Figures 4.15 and 4.16, respectively. The signals are nearly identical and less intense than the previous cases, therefore, it was concluded the lens itself was not fluorescing. These test cases exhibited the same ringing and double peak shown in Figures 4.1 - 4.10.

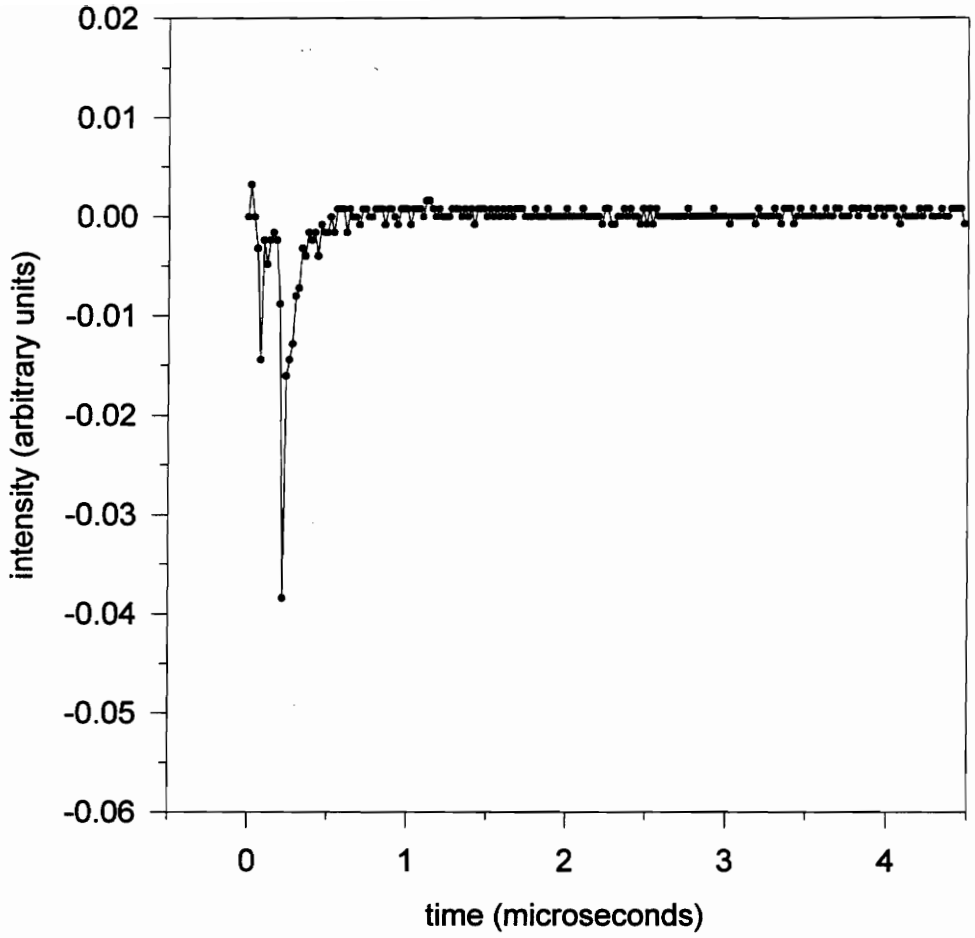

Figure 4.11: Dy:YAG coated fiber (ϕ = 2 mm)
external excimer illumination
Nicolet oscilloscope

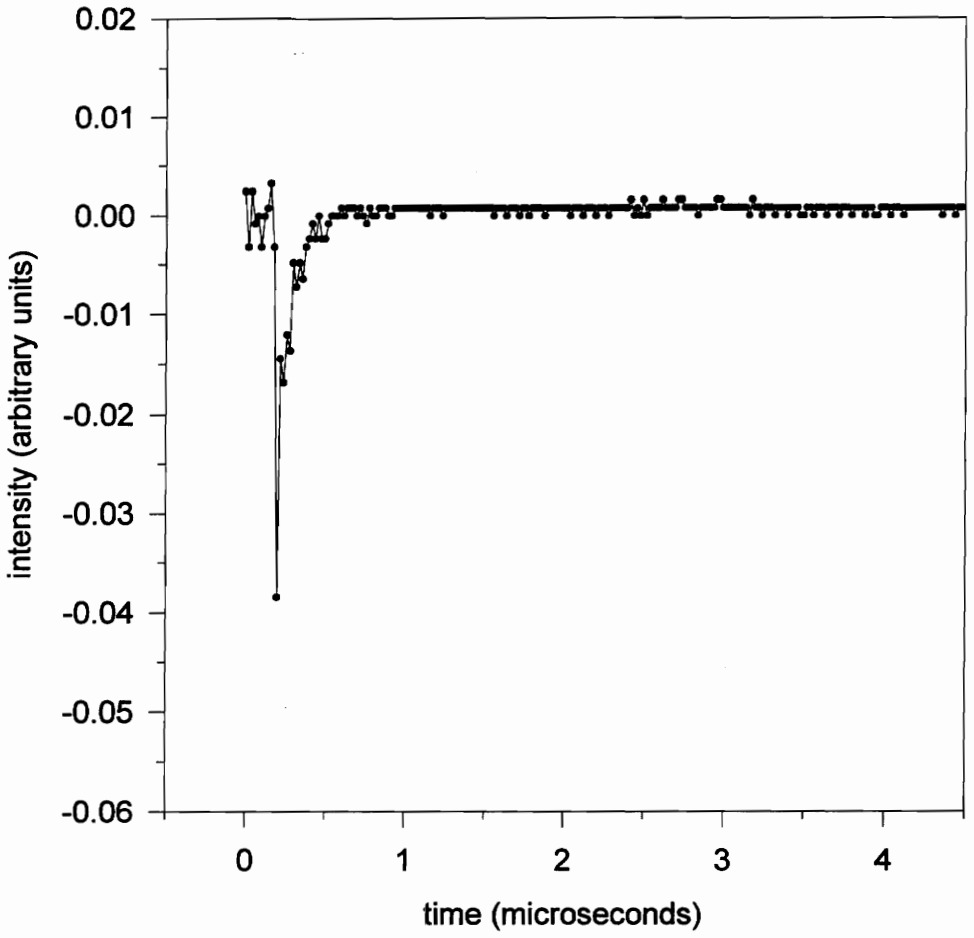

Figure 4.12: Bare fiber (ϕ = 2 mm)
external excimer illumination
Nicolet oscilloscope

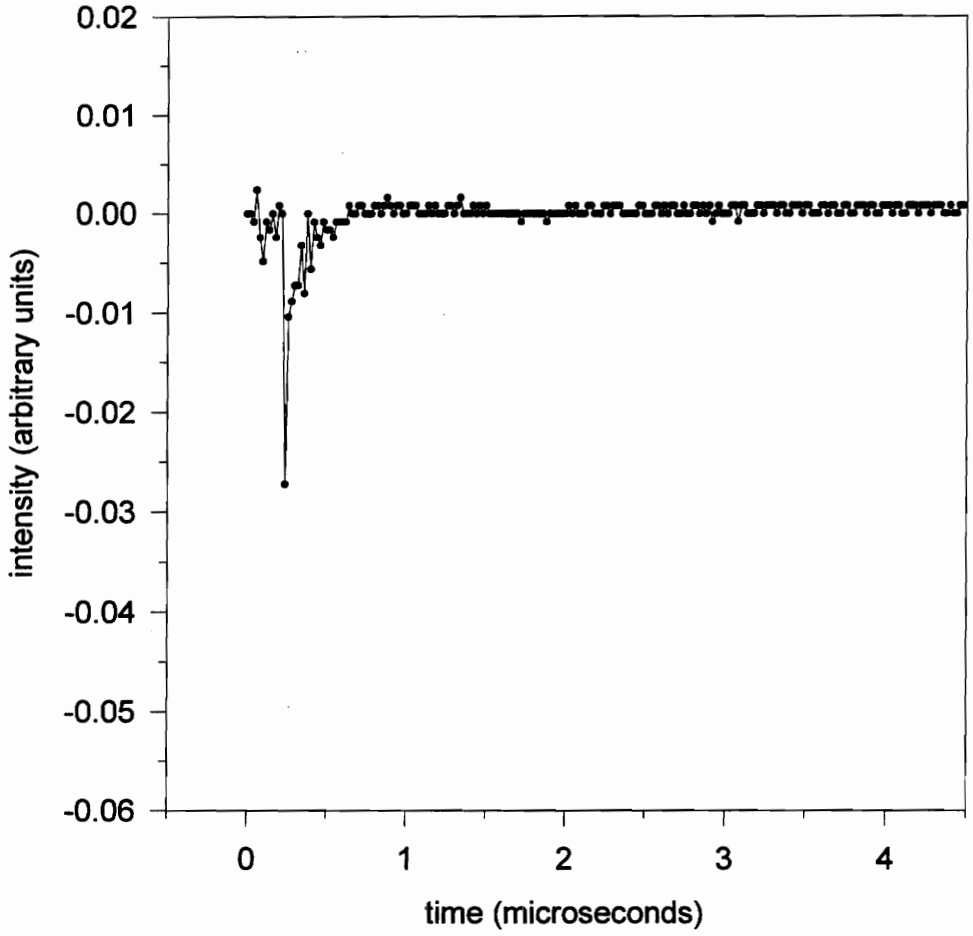

Figure 4.13: Dy:YAG coated fiber (ϕ = 2 mm)
external excimer illumination
low pass laser filter
Nicolet oscilloscope

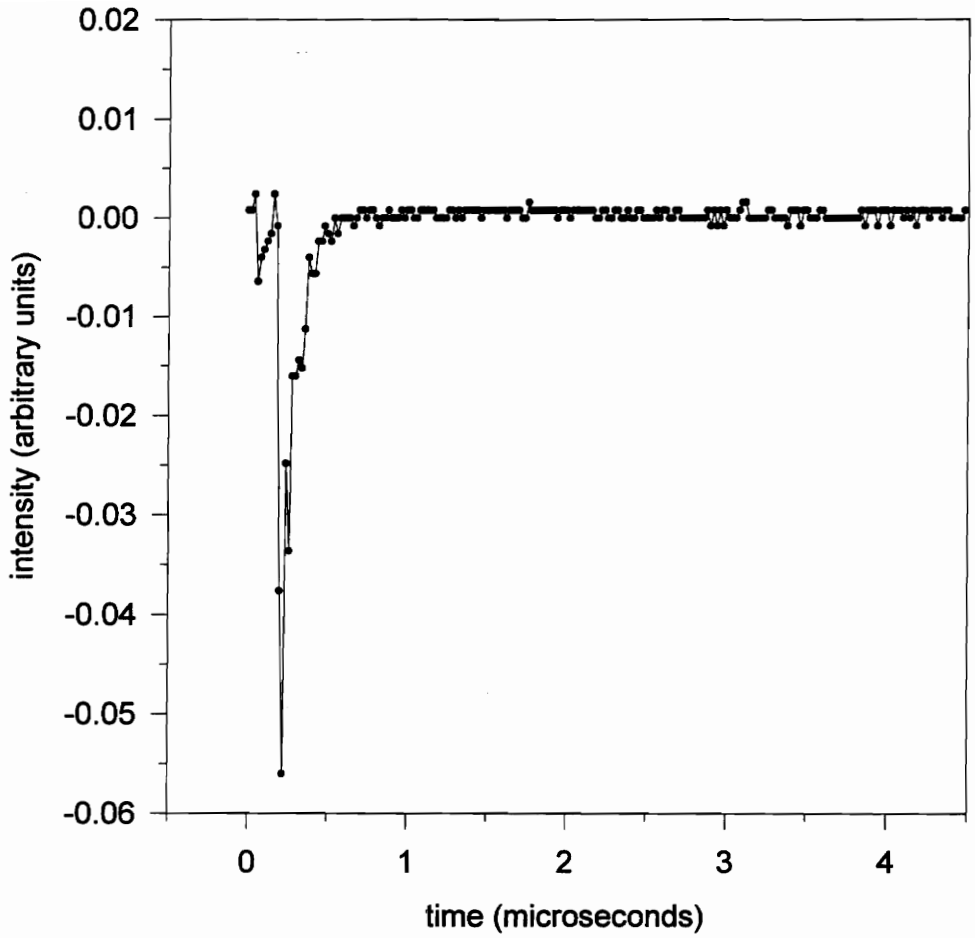

Figure 4.14: Bare fiber (ϕ = 2 mm)
external excimer illumination
low pass laser filter
Nicolet oscilloscope

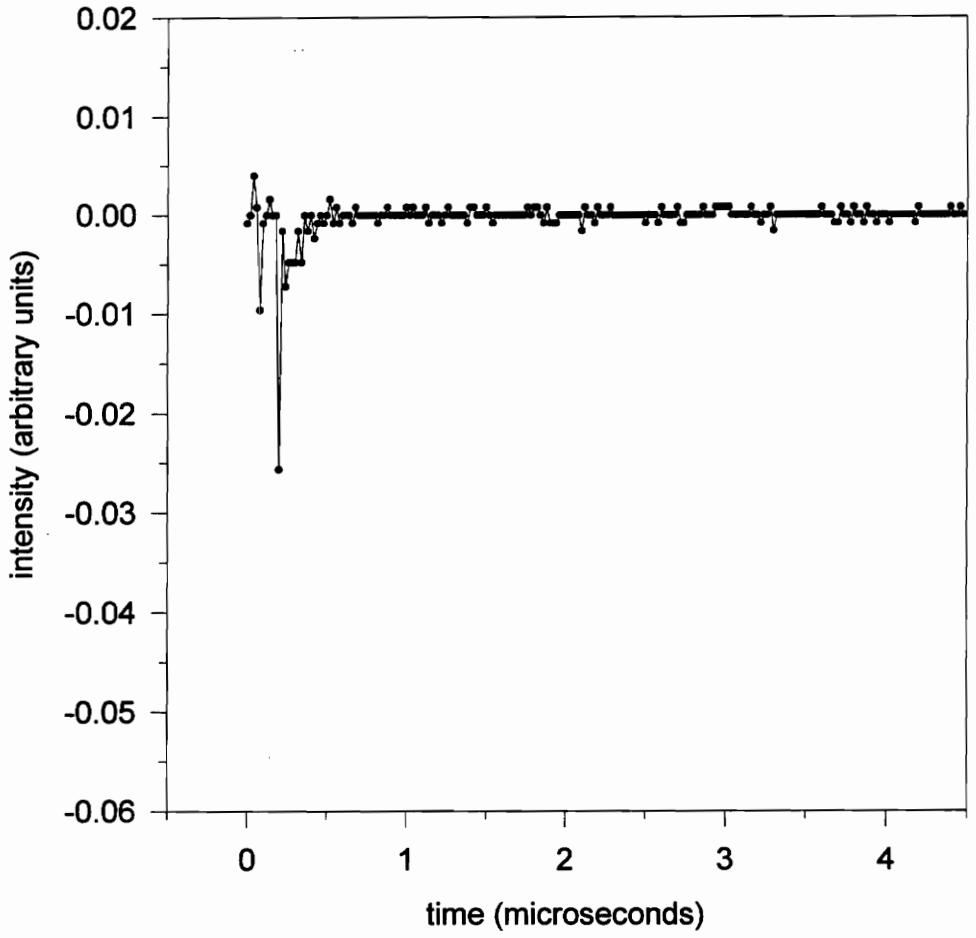

Figure 4.15: Dy:YAG coated fiber ($\phi = 2$ mm)
external excimer illumination
no focusing optics
Nicolet oscilloscope

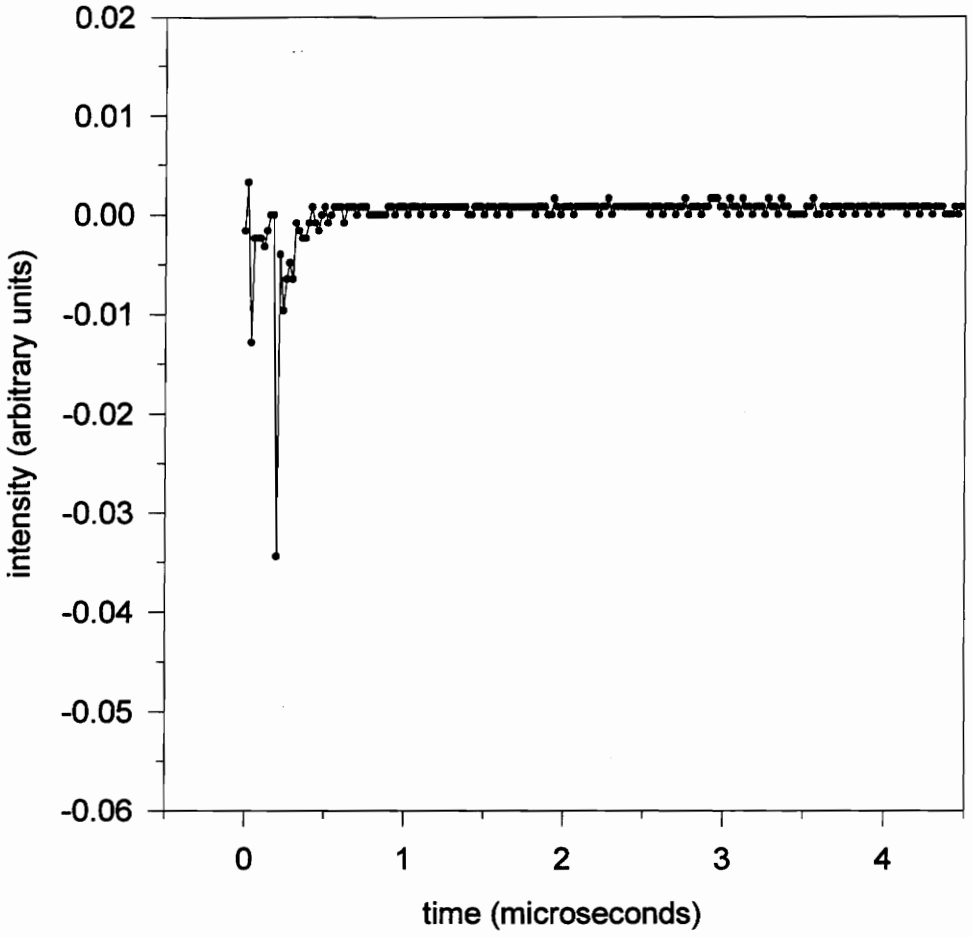

Figure 4.16: Bare fiber (ϕ = 2 mm)
external excimer illumination
no focusing optics
Nicolet oscilloscope

4.2.2 600 μm DIAMETER FIBER

Next, a small diameter fiber (ϕ = 600 μm) was examined to test the external phosphor illumination. The Nicolet digital oscilloscope was set at 100 mV full scale and the PMT power supply was set at 900 V. All of the following plots are an average of 10 cases. Each test run recorded 225 data points with a sampling rate of 20 nanoseconds per data point. The oscilloscope was triggered when it receives the synchronized output signal from the laser when it lased.

Figures 4.17 and 4.18 compare the external excimer illumination for the coated and uncoated fiber #1. The coated fiber has a much stronger signal resulting from the Dy:YAG tempreature dependent emission. Figures 4.19, 4.20, and 4.21 contain the plots for the three coated cases with the low pass laser filter (Schott UG-11 filter). Figures 4.22, 4.23, and 4.24 give a baseline comparison for uncoated fibers. The bare fibers have a stronger signal and this contradicts the previous figures (4.17 vs. 4.18). All of these plots also exhibit the ringing and double peak problems as in the previous plots.

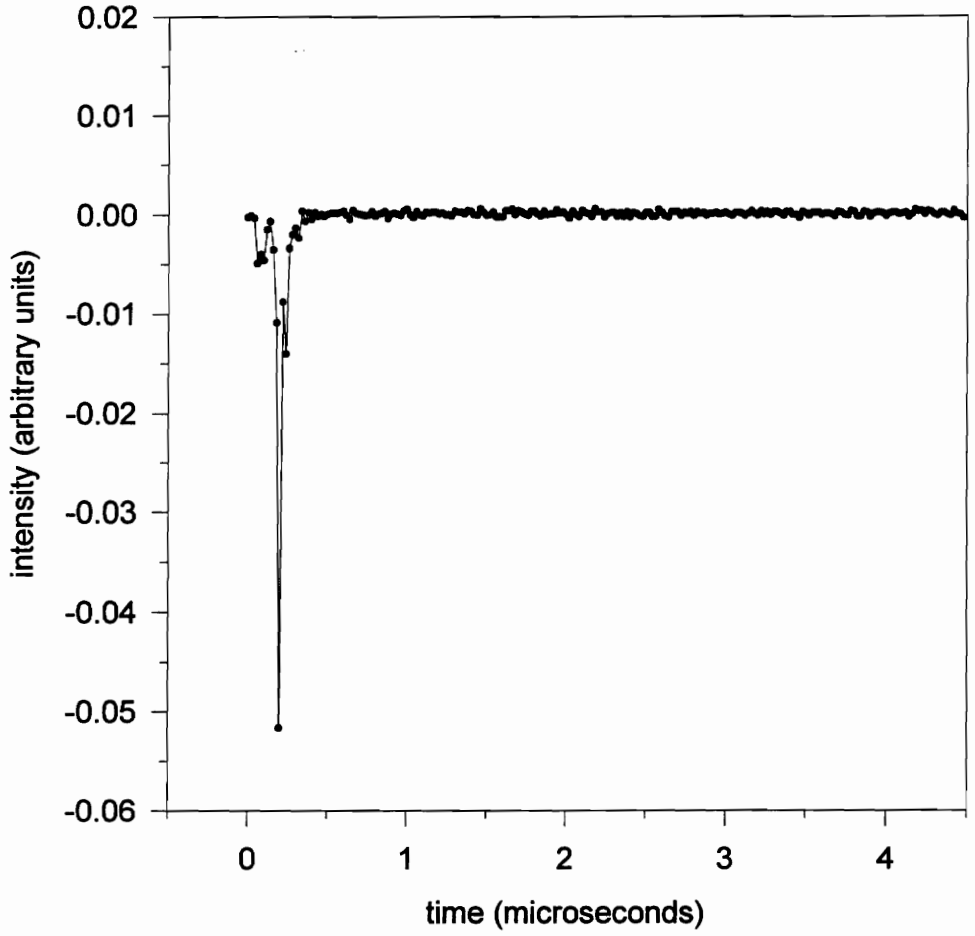

Figure 4.17: Dy:YAG coated fiber #1 (ϕ = 600 μm)
external excimer illumination
Nicolet oscilloscope

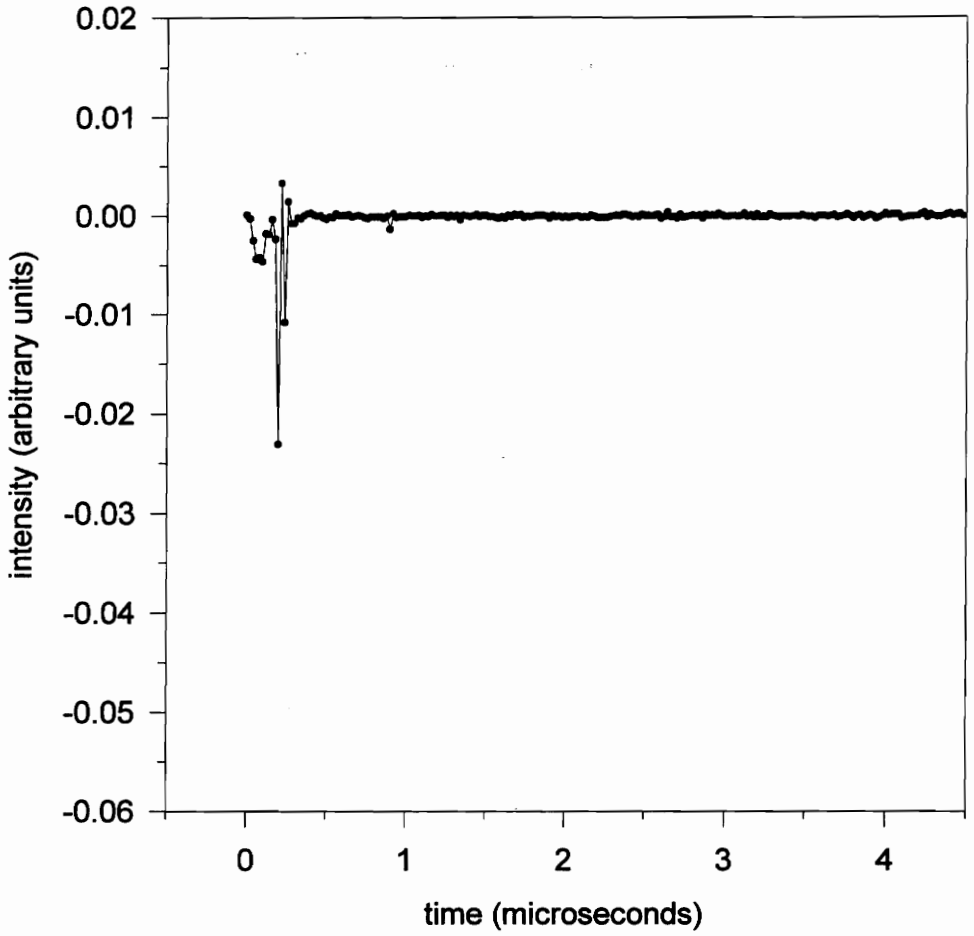

Figure 4.18: Bare fiber #1 (ϕ = 600 μm)
external excimer illumination
Nicolet oscilloscope

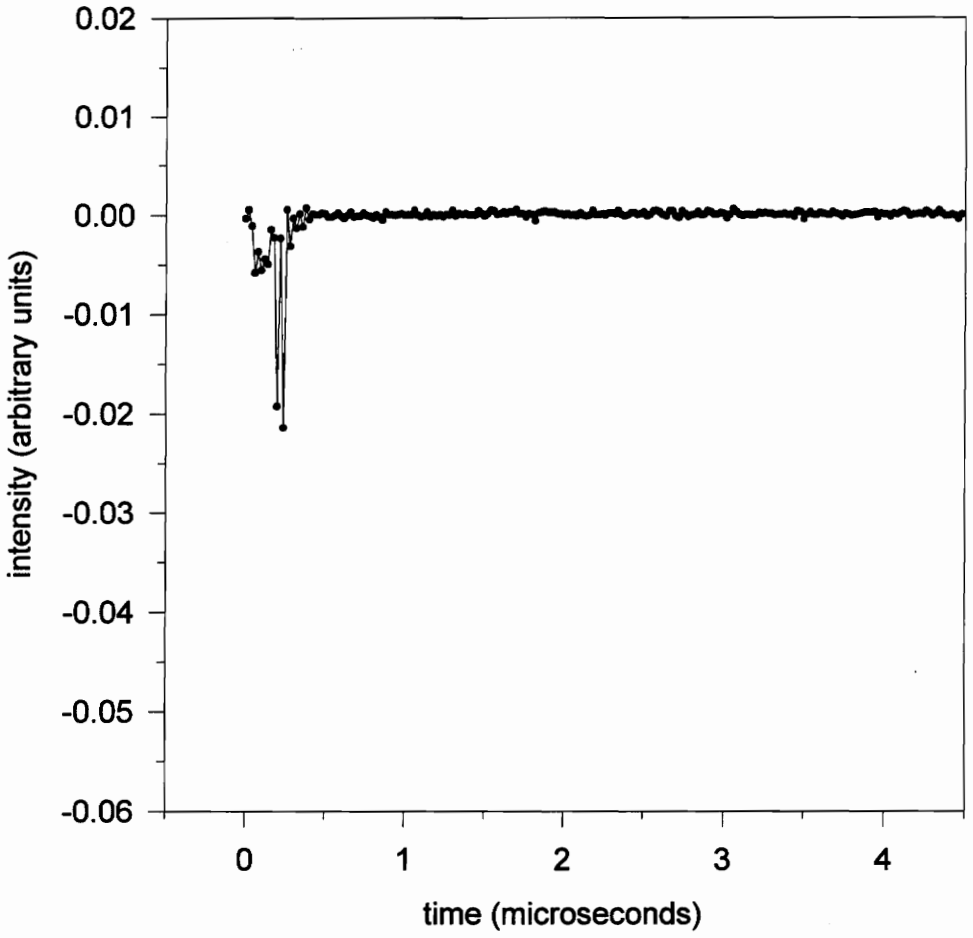

Figure 4.19: Dy:YAG coated fiber #1 (ϕ = 600 μm)
external excimer illumination
low pass laser filter
Nicolet oscilloscope

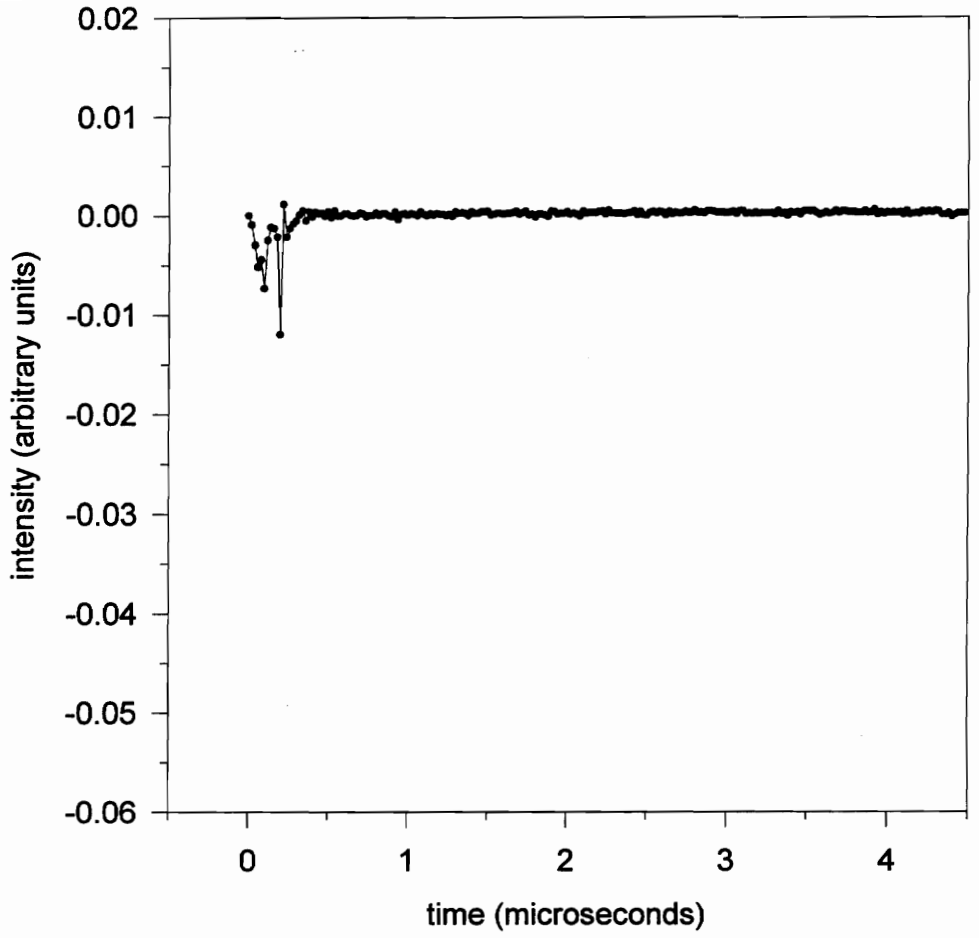

Figure 4.20: Dy:YAG coated fiber #2 (ϕ = 600 μm)
external excimer illumination
low pass laser filter
Nicolet oscilloscope

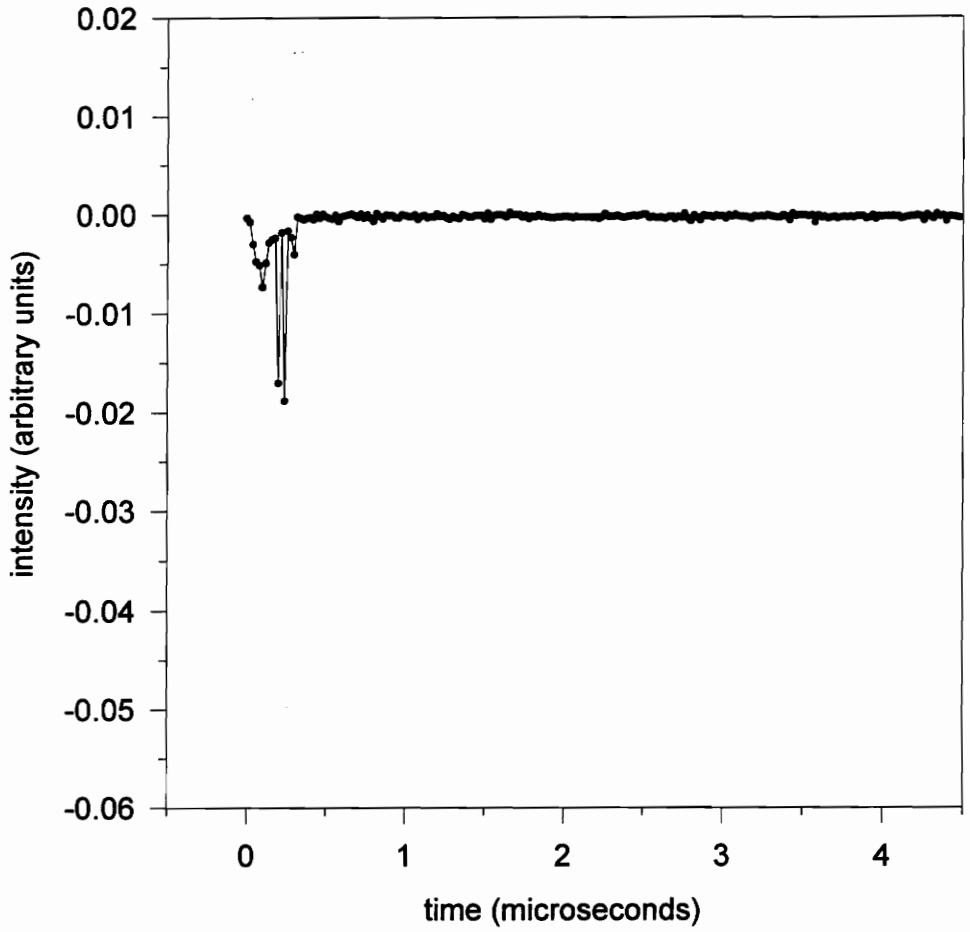

Figure 4.21: Dy:YAG coated fiber #3 (ϕ = 600 μm)
external excimer illumination
low pass laser filter
Nicolet oscilloscope

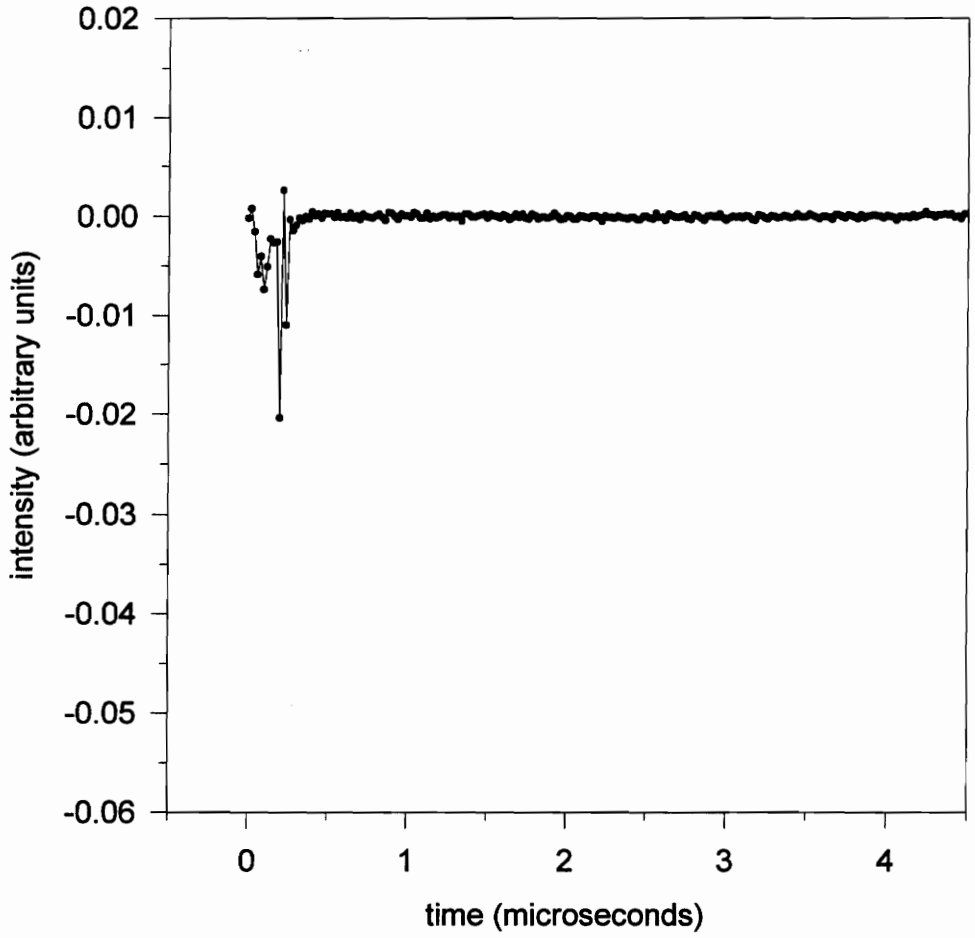

Figure 4.22: Bare fiber #1 (ϕ = 600 μm)
external excimer illumination
low pass laser filter
Nicolet oscilloscope

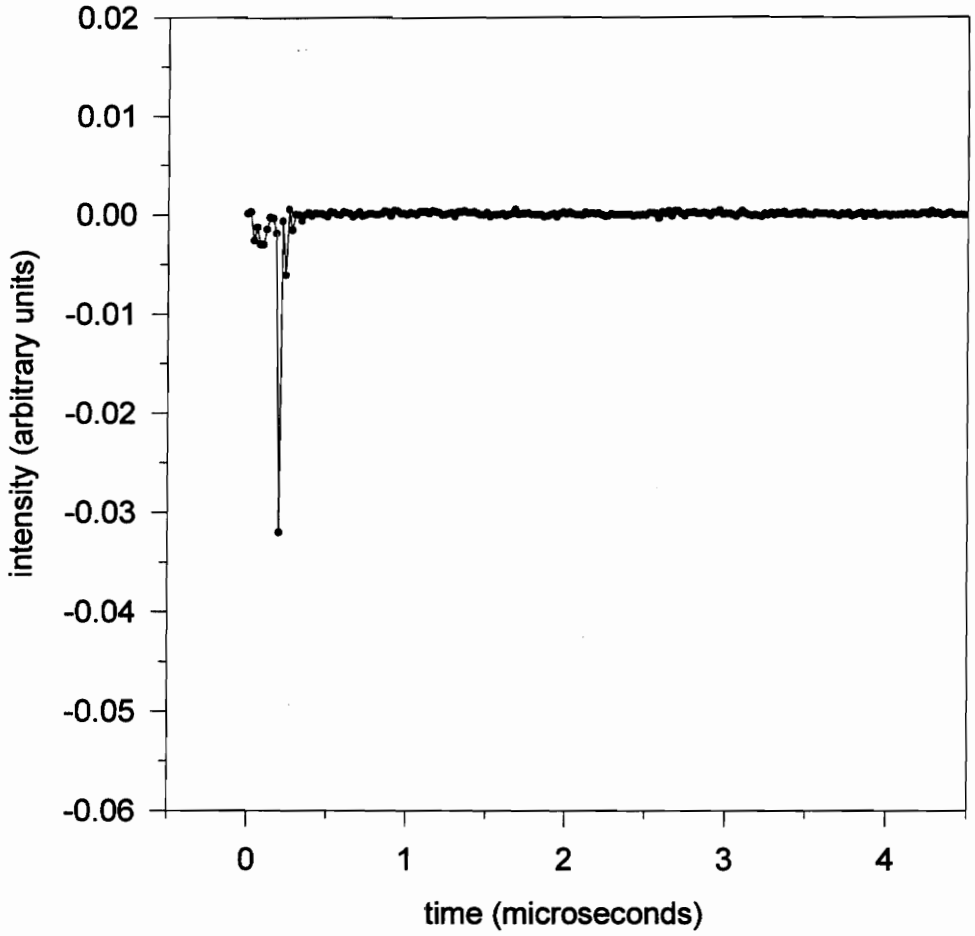

Figure 4.23: Bare fiber #2 (ϕ = 600 μm)
external excimer illumination
low pass laser filter
Nicolet oscilloscope

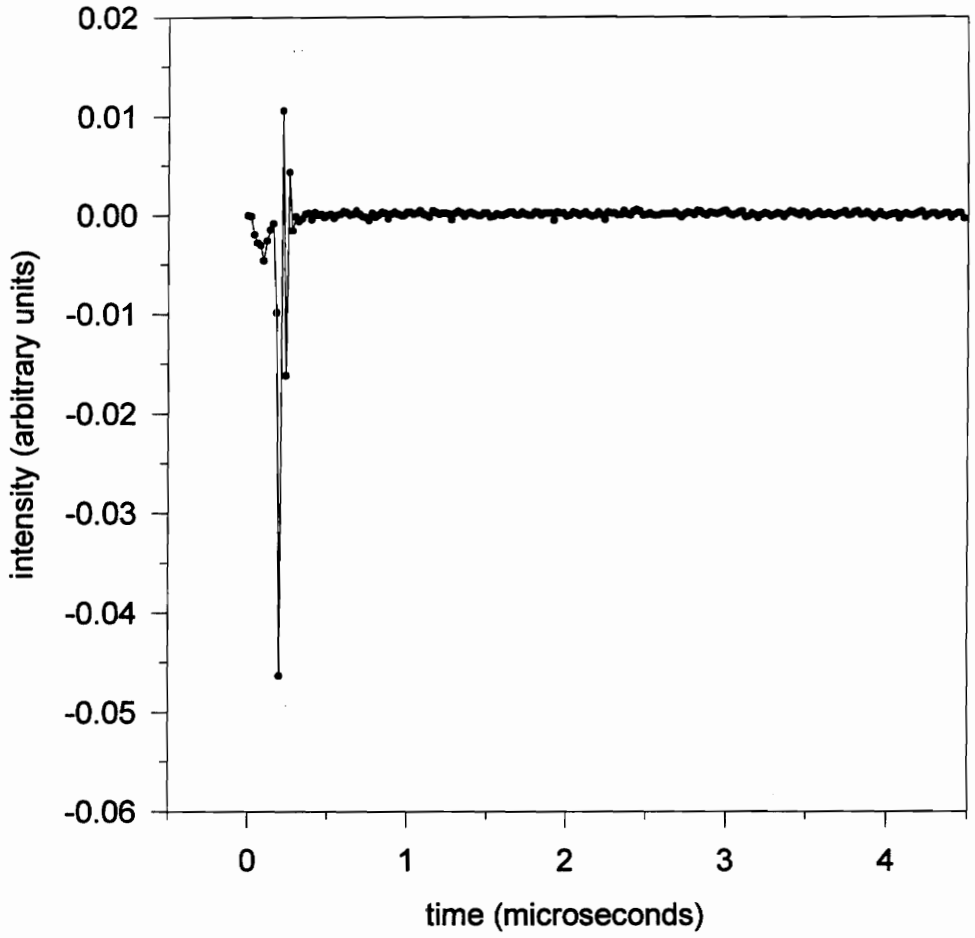

Figure 4.24: Bare fiber #3 (ϕ = 600 μm)
external excimer illumination
low pass laser filter
Nicolet oscilloscope

4.2.3 TEKTRONIX OSCILLOSCOPE

Because the oscilloscope for the previous cases could not measure many data points per pulse due to a limited sampling rate oscilloscope, a faster scope was used to determine the effectiveness of the side on illumination of the 600 μm fibers. The oscilloscope was a Tektronix TDS 684A and it was set at 500 mV per division and the sampling rate was 20 picoseconds per point. Figure 3.17 contains the experimental schematic minus the HeNe lasers and mirror. The filters and lenses discussed in sections 3.2.1 and 3.2.4 were used in this case. The triggering was the same as before except a voltage divider was used going into the scope, since the trigger would overwhelm the scope (the synchronous output was 20±5 V and the input for the scope had to be less than 20 V). Each run collected 15,000 data points and 47 runs were averaged.

Figures 4.25, 4.26, and 4.27 contain the coated fiber test cases and Figures 4.28, 4.29, and 4.30 give the baseline comparison for the bare fibers. The coated fiber signals were approximately double the bare fiber signals except for the bare fiber #1 case. These results show the ringing phenomena more clearly because of the finer time resolution. The larger ringing effect is a result of the snubbing coaxial cable discussed earlier. The high frequency ringing is due to the PMT base not being wired for measurements in the picosecond range. The PMT does have a photon transit time of about 20 nanoseconds and this shows up on all of the plots.

The plots created from data measured with the faster oscilloscope (Tektronix model TDS 684A) exhibit an Dy:YAG emisison signal which is stronger than the background noise. The plots exhibit a reproducable signal which is the measurement required to construct the proposed optical thermal sensor. The evanescent coupling scheme would also have been invetsigated if the scope was available, but the scope was on loan from the Naval Research Laboratory and only available for five hours. After setting up for measurements, only one hours worth of experiments were conducted which limited the number and diversity (not including the evanescent coupling) of tests. The potential for the evanescent coupler was not thoroughly investigated and could produce a stronger emission signal distinguishable from noise as shown by the side on illumnation of the larger (600 μm) fibers.

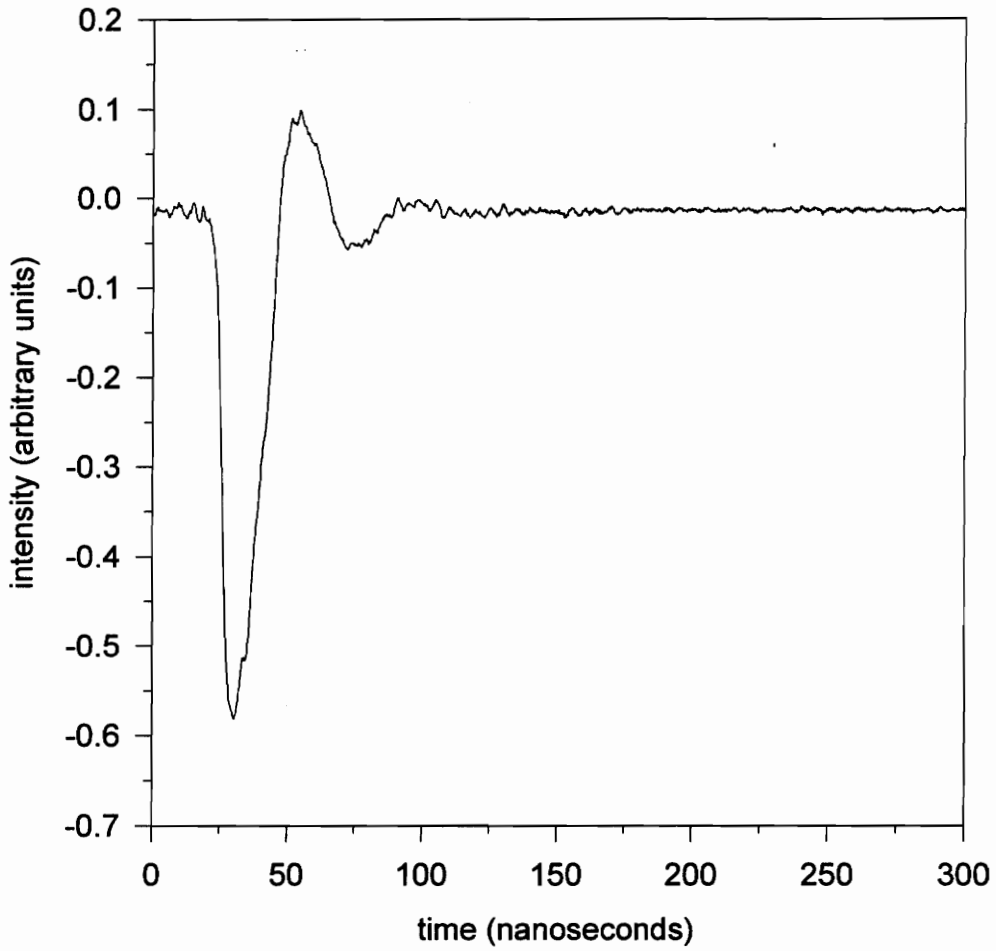

Figure 4.25: Dy:YAG coated fiber #1 (ϕ = 600 μm) external excimer illumination Tektronix oscilloscope

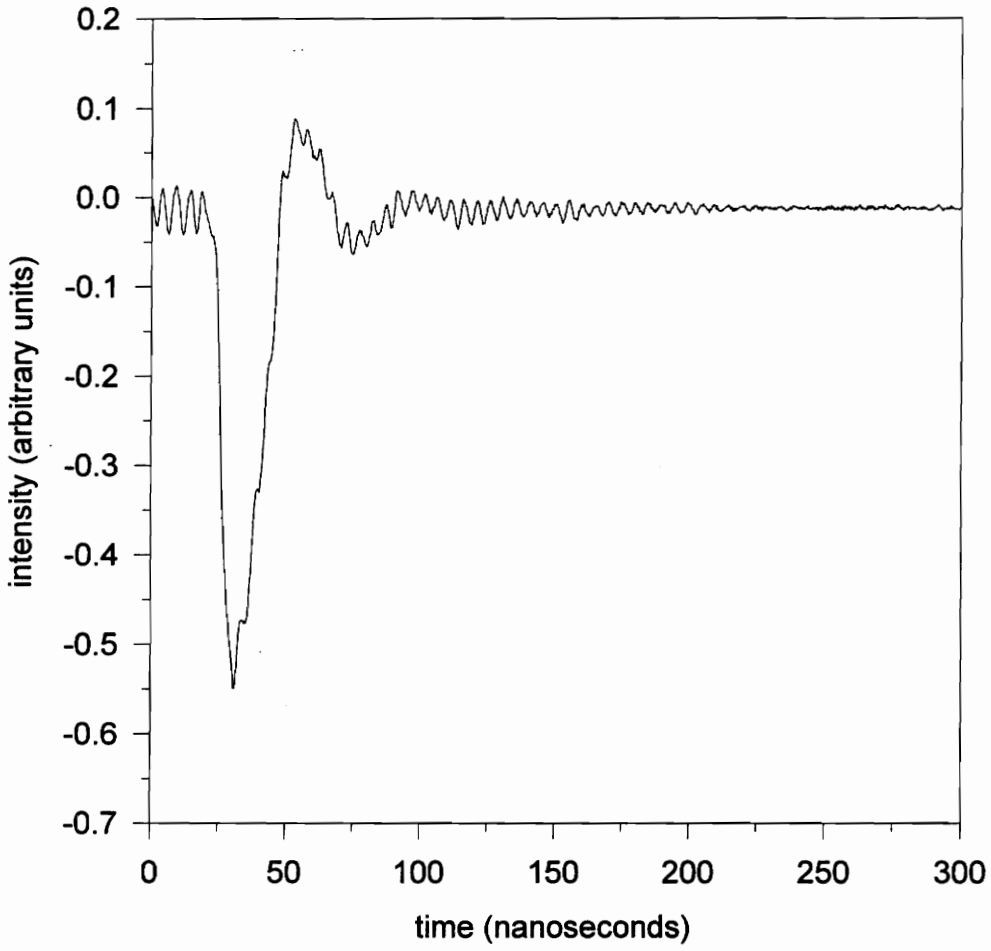

Figure 4.26: Dy:YAG coated fiber #2 (ϕ = 600 μm) external excimer illumination Tektronix oscilloscope

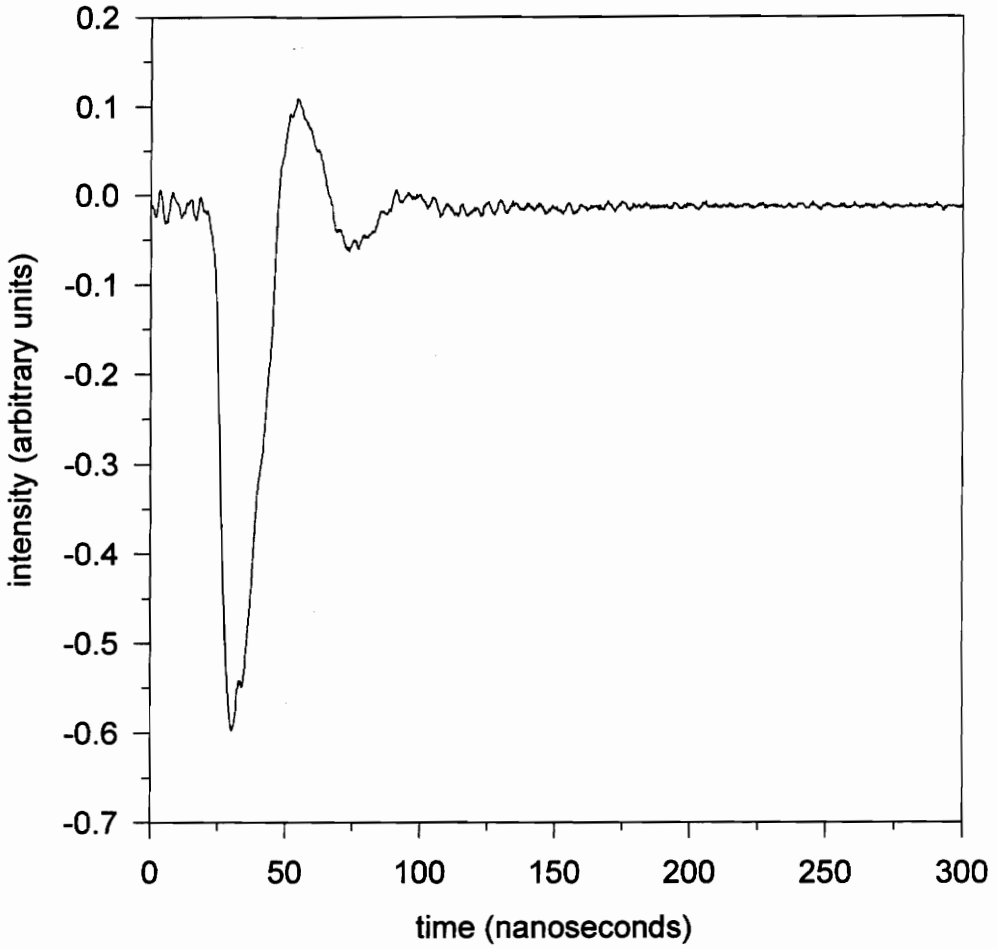

Figure 4.27: Dy:YAG coated fiber #3 (ϕ = 600 μm) external excimer illumination Tektronix oscilloscope

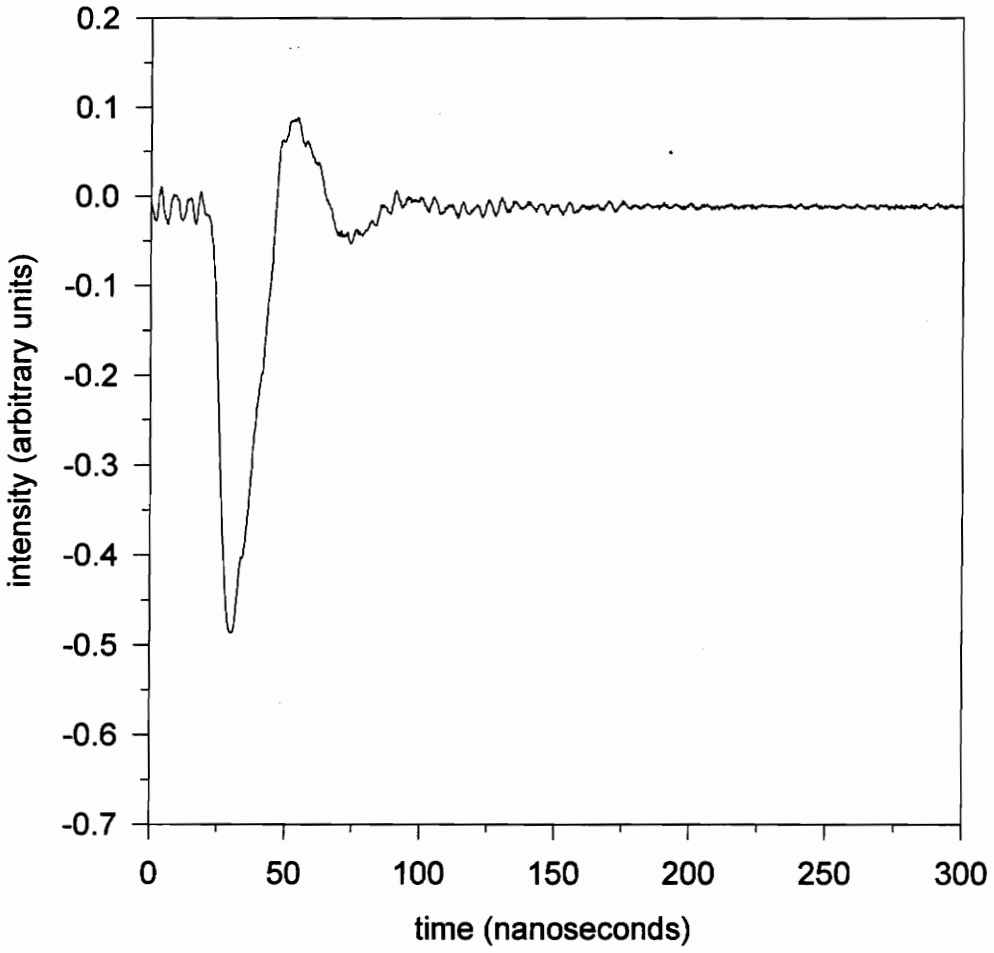

Figure 4.28: Bare fiber #1 (ϕ = 600 μm) external excimer illumination Tektronix oscilloscope

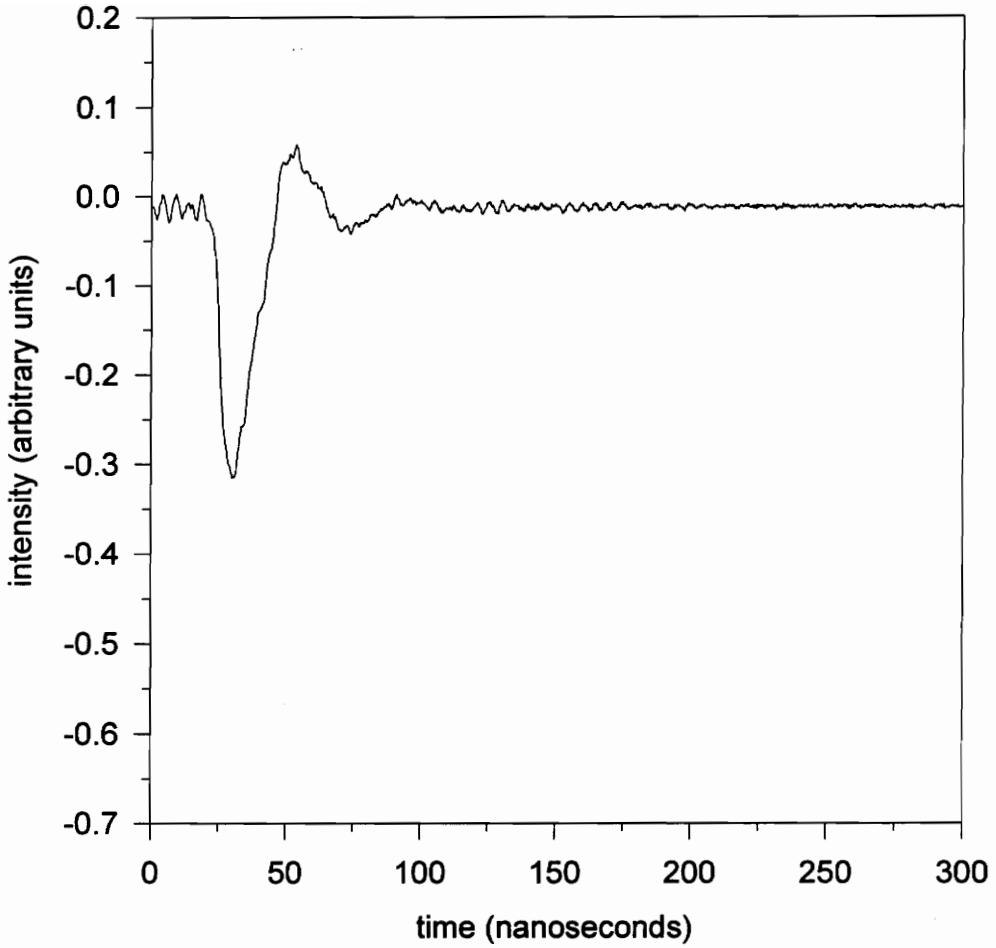

Figure 4.29: Bare fiber #2 (ϕ = 600 μm) external excimer illumination Tektronix oscilloscope

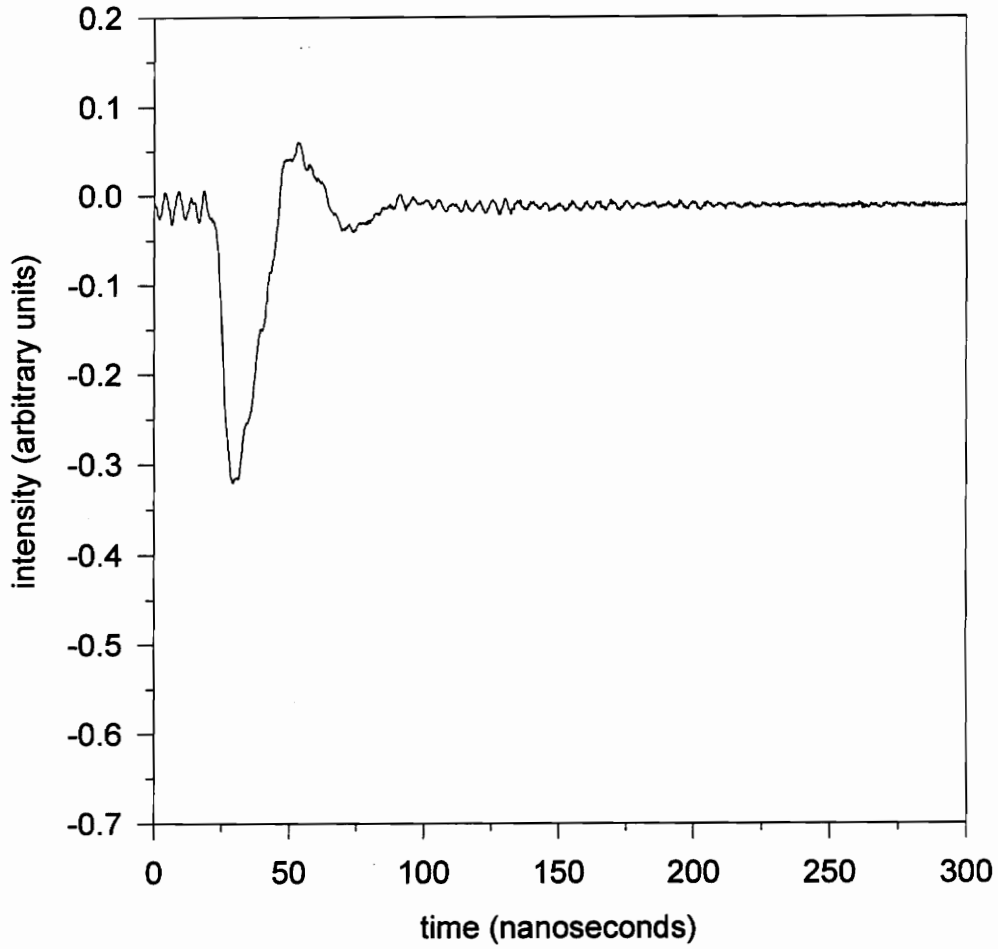

Figure 4.30: Bare fiber #3 (ϕ = 600 μm) external excimer illumination Tektronix oscilloscope

5.0 SUMMARY AND CONCLUSIONS

5.1 SUMMARY

This study can be broken up into three main parts: (i) synthesis of Dy:YAG from raw materials in the lab, (ii) deposition of this material onto an optical fiber, and (iii) measurements of the visible emission from the prototype sensor.

5.1.1 Dy:YAG SYNTHESIS

The results of the Dy:YAG synthesis can be summarized as:

1) The Dy:YAG crystal could not be synthesized using the solid state synthesis technique. The XRD patterns showed that the crystal planes of the reference YAG structure did not match.
2) The Dy:YAG crystal was synthesized using the precipitation reaction. This was confirmed by a matching reference XRD pattern.

5.1.2 DEPOSITION TECHNIQUES

Two deposition methods were tested in this thesis. One was a thin film pulsed laser deposition (PLD) and the other a thick film slurry technique. The deposition results are summarized below:

1) A thin film of Dy:YAG crystals could not be deposited onto the fiber using the pulsed laser deposition technique. This method transformed the crystal into an

amorphous layer on the substrate. The proposed explanation for this outcome is that the required substrate temperature (~1100°C, Bai, et al. [1994]) in the vacuum chamber could not be reached with the current heating element.

2) A thick film of Dy:YAG could be deposited onto the fibers utilizing the slurry technique. There was some residue left behind from the binder materials, but the XRD pattern matched the powder's. The thick film Dy:YAG coated fibers were, therefore, used in the experiments to check the emission properties of the sensor.

5.1.3 EMISSION SIGNALS

The emission signals were measured for the evanescent coupling technique and external pumping of the Dy:YAG coated fibers. The results are given below:

1) The evanescent coupling was checked for a large and small diameter fiber, 2 mm and 600 μm respectively.
   - The small diameter fiber's noise was greater than the emitted visible signal from the Dy:YAG coating.
   - The larger fiber also emitted more noise than signal, but the noise came from impurities from within the fiber.

2) The external pumping was also checked for the large and small diameter fibers.
   - The large fiber case produced the same amount of noise and signal for the coated and uncoated fibers.
   - The noise and signal were of equal magnitude for the small fiber, also.

3) A faster digital oscilloscope revealed that the above measurements were inconclusive. The tests reveal that a finer time resolution scope taking more averages shows a signal which doubles the noise for an externally excited 600 μm Dy:YAG coated fiber. Appendix G contains the standard deviation for the peak value on some of the emission signal measurements.

5.2 CONCLUSIONS

External pumping of the coated fibers showed that the emission signal can be separated from the background noise with the faster Tektronix scope. Therefore, the proposed Dy:YAG optical thermal sensor design is valid, using the optical fiber to waveguide the visible emission from the sensor element to a remote optical detector.

The emission spectrum for the Dy:YAG used for coating the fibers did not match the one of Goss, et al. [1989], but the temperature independent peak in the spectrum was close. If the emission from this wavelength range remains independent of and the other emission range increases with temperature then the synthesized Dy:YAG could be used to construct an optical thermal sensor. The Nicolet digital oscilloscope was too slow measure the room temperature emission of the temperature independent peak. This peak must be separated from the background noise in order to utilize the intensity ratio temperature correlation.

The Pulsed Laser Deposition of the Dy:YAG needs improvement, because the thin film is more durable than the thick film slurry. The thick film is very fragile can not endure a combusting environment. Another advantage to the thin film is that it may have a better evanescent wave coupling due to the uniformity of the fiber core-coating interface—more Dy:YAG crystals in the absorbing matrix.

5.2.1 RECOMMENDATIONS

The coated optical thermal sensor needs more testing to utilize the Dy:YAG temperature dependent emission for a fully functional heat flux sensor. The Dy:YAG crystal has been shown to measure temperatures up to 2100 K according to Lewis, et al. [1990] and Goss, et al. [1989]. Hopefully, with further investigation, the Pulsed Laser Deposition thin film Dy:YAG prototype sensor could evolve into a heat flux gauge for use in an operational turbine. A possible design of a heat flux gage using fiber sensors is shown in Figure 5.1 (patent pending US 1995).

The key to building the heat flux sensor is distinguishing two pulses from two different locations along a single fiber. Another aspect of the sensor which would make it more robust is the ability to pump the Dy:YAG from within the fiber using the evanescent wave phenomena. Perfecting the PLD of the Dy:YAG thin film would improve the coupling efficiency and coating durability.

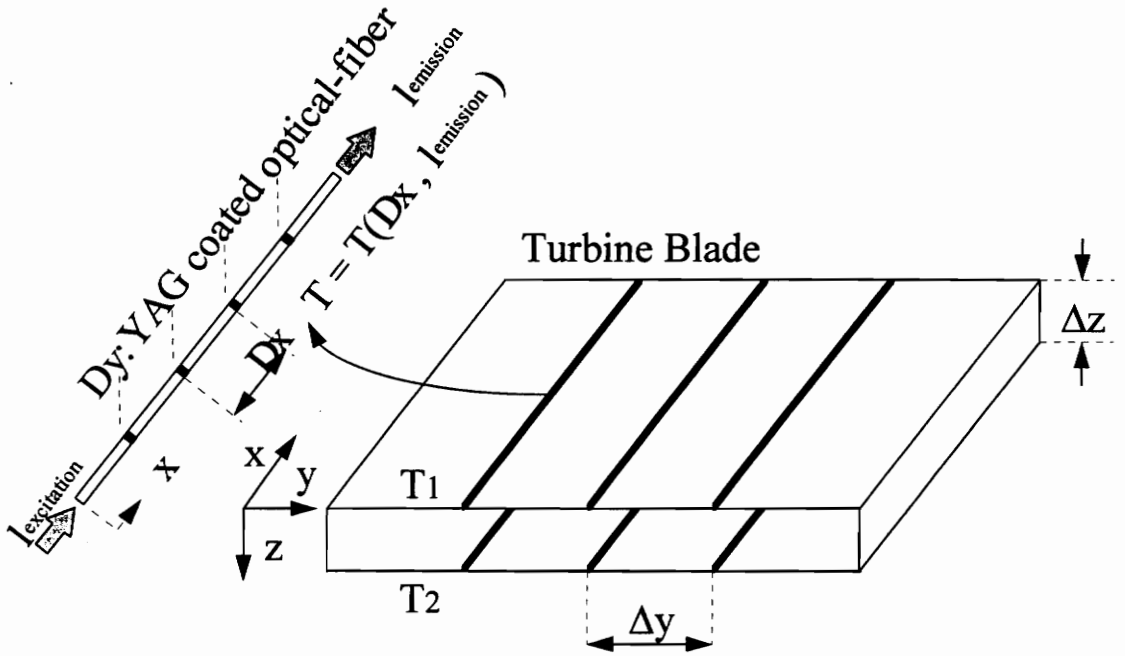

Figure 5.1: Heat flux gauge schematic (patent pending US 1995)

REFERENCES

Allison, S. W., Cates, M. R., Scudiere, M. B., Bentley, H. T. III, Borella, H., and Marshall, B., "Remote thermometry in a combustion environment using the phosphor technique", *SPIE*, v788, pp. 90-99, 1987.

Andrade, J. D., VanWagenen, R. A., Gregonis, D. E., Newby, K., & Lin, J. N., "Remote Fiber-Optic Biosensors Based on Evanescent-Excited Fluoro-Immunoassay: Concept and Progress", *IEEE Transactions on Electron Devices*, vED-32, #7, pp. 1175-1179, July 1985.

Bai, G. R., Chang, H. L. M., and Foster, C. M., "Preparation of single-crystal $Y_3Al_5O_{12}$ thin film by metalorganic chemical vapor deposition", *Applied Physics Letters*, v64, #14, pp. 1777-1779, April 4, 1994.

Bizzak, D. J., and Chyu, M. K., "Rare-earth phosphor laser-induced fluorescence thermal imaging system", *Rev. of Sci. Instrum.*, v65, #1, pp. 102-107, January 1994.

Burle Reference Manual, *Photomultiplier Handbook - Theory Design Application*, Burle Industries, Inc., pp. 80-90, 1980.

Cole, G., "Design of an optical heat flux gage", 1993.

Dakin, J. P., "Distributed optical fiber sensors", *SPIE*, v1797, pp. 76-108, 1992.

Dakin, J. P., "Multiplexed and distributed optical fibre sensor systems", *J. Phys. Elec.*, v20, pp. 954-967, 1987.

Davies, D. E. N., "Signal Processing for Distributed Optical Fibre Sensors", Proceedings of the 2nd International Conference on Optical Fibre Sensors (IEE) , pp. 285-295, September 1984.

Farries, M. C., and Fermann, M. E., "Temperature sensing by thermally-induced absorption in a neodymium doped optical Fibre", *SPIE*, v798, pp. 115-120, 1987.

Goss, L. P., Smith, A. A., and Post, M. E., "Surface thermometry by laser-induced fluorescence", *Rev. Sci. Instrum.*, v60, #12, pp. 3702-3706, December 1989.

Healy, P., "Instrumentation principles for optical time domain reflectometry", *J. Phys. Elect. & Sci. Inst.*, v19, #1-6, pp. 334-341, 1986.

Lewis, W., Turley, W. D., Borella, H. M., and Noel, B. W., "Noncontact Thermometry in Excess of 2500 degrees F using Thermographic Phosphors", *Proceedings of the International Instrumentation Symposium*, v36, pp. 23-27, 1990.

Lieberman, R. A., Blyler, L. L., and Cohen, L. G., "A Distributed Fiber Optic Sensor Based on Cladding Fluorescence", *Journal of Lightwave Technology*, v8, #2, pp. 212-220, February 1990.

Marcuse, D., "Launching Light into Fiber Cores from Sources Located in the Cladding", *Journal of Lightwave Technology*, v6, #8, pp. 1273-1279, August 1988.

Quoi, K. W., Lieberman, R. A., Cohen, R. G., Shenk, D. S., and Simpson, J. R., "Rare-Earth Doped Optical Fibers for Temperature Sensing", *Journal of Lightwave Technology*, v10, #6, pp. 847-852, June 1992.

Rogers, A. J., "Distributed Optical -Fibre Sensors for the Measurement of Pressure, Strain and Temperature", *Physics Reports (Review Section of Physics Letters)*, v169, #2, pp. 99-143, 1988.

Sami, D. A., Brewington, A. J., Thomas, M. A., and Miller, J. A., "High-Temperature Remote Thermometry Using Laser-Induced Fluorescence Decay Lifetime Measurements of Y_2O_3:Eu and YAG:Tb Thermographic Phosphors", *IEEE Transactions on Instrumentation and Measurement*, v42, #3, pp. 735-739, June 1993.

Shackelford, J F., *Introduction to Materials Science for Engineers*, 2nd Ed., Macmillan Publishing Company, pp. 108-116, 1988.

Smith, T. V., and Smith, D. B., "Fiber optic temperature sensor using a Y_2O_2S:Eu thermographic phosphor", *SPIE*, v2070, pp. 456-463, 1993.

Snyder, A. W. and Love, J. D., *Optical Waveguide Theory*, Chapman and Hall, pp. 3-50, 124-125, & 205-223, 1983.

Tobin, K. W. Jr., Beshears, D. L., Turley, W. D., Lewis, W. III, and Noel, B. W., "Fiber-sensor design for turbine engines", *SPIE*, v1584, pp. 23-31, 1991.

Tobin, K. W., Allison, S. W., Cates, M. R., Capps, G. J., Beshears, D. L., Cyr, M., and Noel, B. W., "High-Temperature Phosphor Thermometry of Rotating Turbine Blades", *AIAA Journal*, v28, #8, pp. 1485-1490, August 1990.

Vij, D. R. (Ed.), *Thermoluminescent Materials*, PTR Prentice-Hall, pp. 1-29, 1993.

Wickersheim, K. A., and Sun, M. H., "Fiberoptic Themometry and its Applications", *Journal of Microwave Power and Electromagnetic Energy*, v22, pp. 85-94, 1987.

Zehnder, T., Blatter, A., and Bächli, A., "SiC films prepareed by pulsed excimer laser deposition", *Thin Solid Films*, v241, pp. 138-141, 1994.

APPENDIX A

FABRICATION GUIDANCE & MATERIAL SOURCES

Solid State Reaction Raw Materials:

Aluminum Oxide (Al_2O_3), alpha, 99.98% (metals basis), <1 micron powder

Dysprosium Powder (Dy), 99.9% (REO), -40 mesh

Yttrium Oxide (Y_2O_3), REaction, 99.99% (REO), <10 micron white powder

Precipitation Reaction Raw Materials:

Aluminum Nitrate ($Al(NO_3)_3 \bullet 9H_2O$), 98% (Assay), Hygroscopic

Ammonium Hydroxide (NH_4OH), 70%

Dysprosium Oxide (Dy_2O_3), REaction, 99.9% (REO), powder

Nitric Acid (HNO_3), 70%

Yttrium Oxide (Y_2O_3), REaction, 99.99% (REO), <10 micron white powder

Water (H_2O), deionized

The following steps outline the procedure for the precipitation reaction to synthesize the Dy:YAG.

(1) The first step in the precipitation reaction is weighing the constituents according to the calculated mole ratios. The Dy:YAG (2 mole % Dy) has a molecular weight of 598.13 and the goal was to produce a sample with a mass of 23.93 g. This required weighing 0.448 g of Dy_2O_3, 13.278 g of Y_2O_3, and 74.996 g of $Al(NO_3)_3 \bullet 9H_2O$.

(2) The aluminum nitrate is mixed with deionized water, ~1000 mL. The exact amount of water is not too important, but enough is needed to dissolve the aluminum nitrate. The solution is then mixed vigorously with a stirrer.

(3) In a separate container, add about 50 mL of nitric acid (HNO_3, 70%). Heat slowly to a low boil.

(4) Add a small amount of the yttrium oxide to the nitric acid. Repeat the addition of the Y_2O_3 until the solution becomes transparent and then add the rest. Rinse the remaining yttrium oxide with deionized water and add to the acid solution.

(5) Pour the dysprosium oxide powder into the nitric acid solution. Stir the solution to dissolve the powder. Rinse the remaining dysprosium oxide with deionized water and add to the acid solution.

(6) Eye drop more nitric acid into the solution until all of the powder dissolves.

(7) Pour the nitric acid mixture into the aluminum nitrate solution. Wash out the remaining nitric acid mixture with deionized water and add to the solution.

(8) Add approximately 100 mL of deionized water to the solution and stir.

(10) Add about 225 mL ammonium hydroxide (NH_4OH, 70%) until litmus paper (7-11 range) turns green (9). Stir the mixture thoroughly.

(11) Fill the remainder of the beaker with deionized water and stir.

(12) Allow the solution to stand for four days while washing twice daily. Washing is a process where the water atop the precipitate is poured off and more deionized water is added to the solution and then stirred. Repeat this washing process twice a day.

(13) Place the beaker into an oven at 100 °C for 36 hours.

(14) The precipitate from the beaker is then ground into a fine powder and fired for 1.5 hours. The firing procedure is given below.

$$T_{room} \xrightarrow{\Delta T=+550°C/hour} 1450°C(1.5hours) \xrightarrow{\Delta T=-600°C/hour} T_{room}$$

note: heating and cooling rates are oven dependent and not critical

APPENDIX B

SLURRY THICK FILM FABRICATION GUIDANCE & MATERIAL SOURCES

Solvent Solution:

toluene	80 %
ethanol	20 %

Binder Solution:

toluene	61.30 %
ethanol	15.30 %
PVB	13.20 %
plasticizer	7.80 %
surfactant	2.40 %

note: All percentages represent the mass fraction.

Phosphor:

Dy:YAG	2 mole % Dysprosium

Grinding Media:

Al_2O_3 grinding spheres, $\phi = 0.508$ cm, 99.5 % pure

Slurry Mixture:

Solvent	4.2 g
Binder	18.7 g
Dy:YAG	20.1 g
Grinding Media	103.9 g

The slurry mixture is placed in a jar and mixed on a roller for 24 hours.

Thick Film Deposition:

(1) Coat fibers and substrate by dipping into the slurry mixture.

(2) Allow to dry for 24 hours.

(3) Anneal fibers and substrate in an oven to remove binder and solvent from thick film, leaving only the Dy:YAG thick film. The annealing procedure is given by:

$$T_{room} \xrightarrow{\Delta T=+2°C/\min} 450° C(2hours) \xrightarrow{\Delta T=+5°C/\min} 800° C(1hour) \xrightarrow{\Delta T=-5°C/\min} T_{room}\ .$$

APPENDIX C

ELECTROMAGNETIC FIBER EQUATIONS

The following equations are taken from Snyder and Love [1983]. The electric and magnetic field vectors are **E**(x,y,z) and **H**(x,y,z) respectively. Each vector has two parts—one is the power guided without attenuation and the other is remaining power radiated from the fiber. The guided wave is the sum of the bound modes given by:

$$\vec{E}(x,y,z) = \sum_j a_j \vec{E}_j(x,y,z) + \sum_j a_{-j} \vec{E}_{-j}(x,y,z) + \vec{E}_{rad}$$

$$\vec{H}(x,y,z) = \sum_j a_j \vec{H}_j(x,y,z) + \sum_j a_{-j} \vec{H}_{-j}(x,y,z) + \vec{H}_{rad}$$

The electromagnetic bound modes are the transverse resonance's of the fields within the optical fiber. The subscript j indexes the finite number of modes, M. The positive and negative values for j represent the forward and backward traveling modes respectively. The subscript "a" represents the modal amplitudes and depend on the fiber illumination source.

The electric and magnetic fields $\vec{E}_j$ and $\vec{H}_j$ of a bound mode are solutions of Maxwell's equations. The vector Laplacian ($\vec{\nabla}^2$) complicates these equations. $\vec{\nabla}^2$ couples the components of the field vectors for an arbitrary coordinate system. A Scalar Laplacian (∇^2) replaces the vector Laplacian ($\vec{\nabla}^2$) for fixed Cartesian coordinates of $\vec{E}_j$ and $\vec{H}_j$. Therefore the vector wave equation simplifies to:

$$\left\{\nabla_t^2 + n^2k^2 - \beta_j^2\right\}\vec{e}_j = -\left\{\vec{\nabla}_t + i\beta_j\hat{z}\right\}\left\{\vec{e}_{tj} \bullet \vec{\nabla}_t \ln n^2\right\}$$

$$\left\{\nabla_t^2 + n^2k^2 - \beta_j^2\right\}\vec{h}_j = -\left(\vec{\nabla}_t \ln n^2\right) \times \left(\left\{\vec{\nabla}_t + i\beta_j\hat{z}\right\} \times \vec{h}_j\right.$$

where β_j is the propagation constant, n=n(x,y) is the refractive index profile, $k=2\pi/\lambda$ is the free-space wavelength number, and λ is the free-space wavelength. The electric ($\vec{e}_j$) and magnetic ($\vec{h}_j$) fields have Cartesian components for the fixed Cartesian coordinate system.

The scalar wave equation for step profile ($n=n_{co}$ in the core and $n=n_{cl}$ in the cladding) fibers simplifies to:

$$\left\{\nabla_t^2 + n^2k^2 - \beta_j^2\right\}e_{zj} = 0 \qquad \textbf{(C-1)}$$

where β_j is the eigenvalue (propagation constant) and e_{zj} is the longitudinal electric field component of the jth mode. The field components are solutions to the scalar wave equation if and only if it satisfies equation C-1 for all values of x and y, including the core-cladding interface. This is not the case for any component of e_{zj} on a step profile fiber of an arbitrary shape. Thus, the boundary conditions of Maxwell's equations are imposed to solve for the field component in the core and cladding respectively. The longitudinal magnetic field components are derived similarly. The transverse components are then solved for by:

$$\vec{e}_{tj} = \frac{i}{n^2 k^2 - \beta_j^2}\left\{\beta_j \vec{\nabla}_t e_{zj} - \left(\frac{\mu_0}{\varepsilon_0}\right)^{1/2} k\hat{z} \times \vec{\nabla}_t h_z\right\}$$

$$\vec{h}_{tj} = \frac{i}{n^2 k^2 - \beta_j^2}\left\{\beta_j \vec{\nabla}_t h_{zj} + \left(\frac{\varepsilon_0}{\mu_0}\right)^{1/2} kn^2 \hat{z} \times \vec{\nabla}_t e_z\right\}$$

where ε_0 is the free-space dielectric constant and μ_0 is the free-space permeability.

APPENDIX D

X-RAY DIFFRACTION

X-ray diffraction (XRD) is an experimental tool used to identify crystal structures. Diffraction results from scattered x-ray radiation by the crystal atoms whose spacing is about the same as the wavelength of the radiation. This diffraction grating causes the light to be scattered with a strong intensity in a few specific directions. The measured crystal structure represents a three-dimensional diffraction grating and the repeated stacking of the crystal planes serves as a simple diffraction grating. For a simple crystal lattice, the condition for diffraction is shown in Fig. D1 (a). X-ray beams must be scattered off adjacent crystal planes in phase producing a strong intensity, otherwise destructive interference negates the scattering intensity. The Bragg condition determines the precise geometry for constructive interference:

$$n\lambda = 2d\sin(\theta)$$

where n is the integral number of radiation wavelengths (λ), d is the spacing between adjacent crystal planes, and θ is the Bragg angle. Figure D1 (b) shows the relationship of the Bragg angle (θ) and the diffraction angle (2θ). Figure D1 (c) illustrates a schematic of an XRD machine. Over 40,000 XRD patterns are cataloged by the Joint Committee on Powder Diffraction Standards (JCPDS) taken from Shackelford [1988] for identifying new and existing materials, like YAG for example.

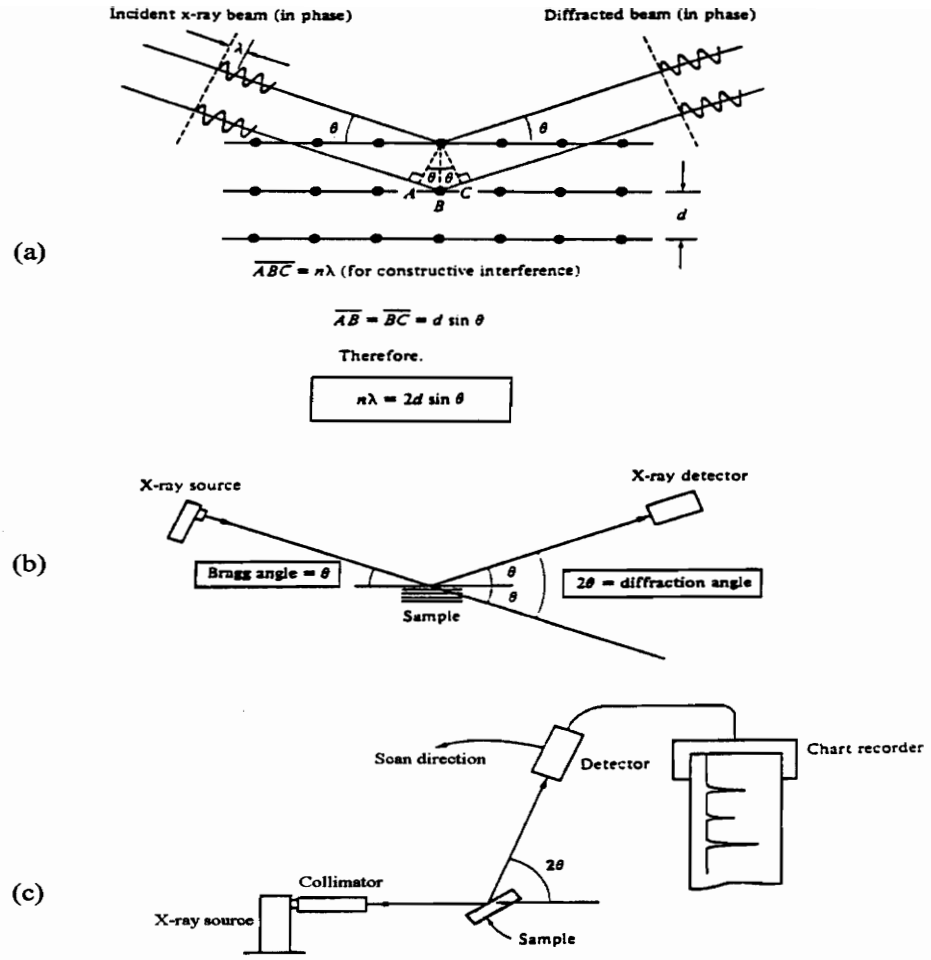

Figure D1: (a) Simple crystal lattice x-ray diffraction condition
(b) Bragg and diffraction angle relationship
(c) XRD schematic
(Shackelford [1988])

APPENDIX E

PULSED LASER DEPOSITION

Pulsed laser deposition (PLD) is a versatile deposition technology. The use of short intense pulses makes laser ablation a congruent process which allows production of complex films from a multi-component target. The intense laser pulses hitting the target produce a plasma above the ablated area. Charged and neutral particles (with kinetic energies of 100 eV and 10 eV respectively) are ejected in a narrow angular dispersion orthogonal to the target surface. This ion assisted process promotes dense film growth with good adhesive properties. The deposited thin films have the same composition as the target material. The process takes place in a vacuum to prevent contamination of the films (i.e. hydrogen contamination). Figure E1 shows a schematic for pulsed laser deposition taken from Zehnder, et al. [1994]).

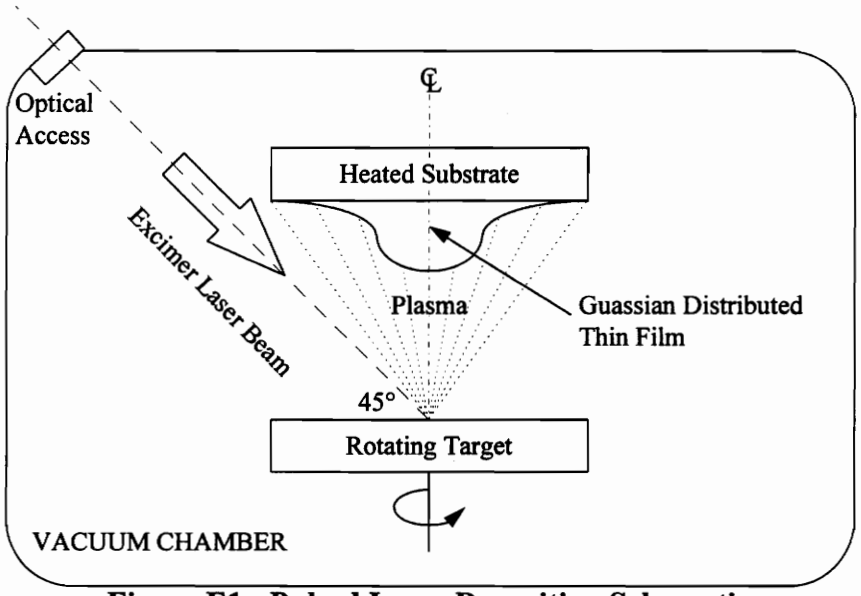

Figure E1: Pulsed Laser Deposition Schematic

APPENDIX F

COMPUTER PROGRAMS

NICOLET OSCILLOSCOPE-COMPUTER DATA TRANSLATION BASIC

CODE

```
10 REM      "DANTRAN.BAS"
20 REM
30 REM      This program transfers every nth point from a Nicolet
40 REM      digital oscilloscope recorded waveform and stores the
50 REM      data as an ASCII file to be read by plotting programs
60 REM      such as Proplot.
70 REM
80 CLS : KEY OFF
90 PRINT "You should have started GWBASIC as 'GWBASIC /C:2048'"
100 PRINT "If you did not, exit and do so.  The program will not
function"
110 PRINT "correctly unless you do."
120 PRINT
130 PRINT "Also, please make sure the CAPS LOCK key is on; this program
only"
140 PRINT "accepts uppercase letters for input."
150 PRINT
160 REM PRINT "Which channel do you wish to transfer data from: A or B";
170 REM INPUT A$
175 A$ = "A"
180 IF A$ = "A" OR A$ = "B" THEN 210 ELSE 190
190 PRINT : PRINT "I said UPPERCASE only!  Perhaps you misunderstood;
please try again."
200 B$ = INKEY$: IF B$ = "" THEN 200 ELSE 80
210 PRINT
220 INPUT "Input start time (i.e., first data point to be read): "; STRT
230 PRINT
240 PRINT "If disk storage is desired, type name of file."
250 PRINT "(8 characters maximum; extension is preset *.DAT)."
260 PRINT "If not, simply press <ENTER> ";
270 INPUT T$
280 REM PRINT : PRINT "   A sampling frequency of 1 means that every
point will be"
290 REM PRINT "   translated, a 2 means every fourth point, a 3 means
every"
300 REM PRINT "   eighth point, and so on in powers of two."
310 REM PRINT : PRINT "What sampling frequency do you desire";
320 REM INPUT XPT
330 CLS
340 DEFINT A-Z
350 DIM N#(11)
```

```
360 OPEN "COM2:9600,S,7,1,LF" FOR RANDOM AS #1
370 PRINT #1, CHR$(1) + ">";
380 PRINT #1, "K,0,131,52"
390 CLOSE
400 OPEN "COM2:9600,N,8,1" FOR RANDOM AS #1
410 PRINT #1, "C,13,13" + CHR$(10)
420 INPUT #1, E
430 PRINT #1, "C,8,1,13"
440 INPUT #1, E
450 PRINT #1, "C,4,1,13"
460 INPUT #1, E
470 IF A$ = "A" THEN PRINT #1, "N,0"
480 PRINT #1, "N,1"
490 INPUT #1, E
500 FOR I = 1 TO 11
510 INPUT #1, N#(I)
520 NEXT I
530 INPUT #1, E
540 X = 15872 / 2 ^ N#(2)
550 DIM D(X)
560 PRINT "Waveform has"; X; "data points."
570 PRINT "Time per point ="; N#(6); "seconds."
580 PRINT "Voltage range ="; N#(5) * 32000; "volts."
590 PRINT
600 PRINT "Transferring data to computer now; please wait..."
610 R = X: I = 0
620 IF A$ = "A" THEN PRINT #1, "D,6,1,0'," + STR$(X) + ",1"
630 REM IF A$ = "B" THEN PRINT #1, "D,6,2,0'," + STR$(X) + ",1"
640 INPUT #1, E
650 IF R < 1000 THEN 680
660 REM IF LOF(1) > 50 THEN 660
670 PRINT #1, CHR$(19);
680 WHILE LOC(1) > 3: L$ = INPUT$(1, 1): H$ = INPUT$(1, 1): D(I) =
CVI(L$ + H$): I = I + 1: WEND
690 LOCATE 7, 4: PRINT "Finished with data point"; I;
700 R = X - I
710 IF R > 0 THEN PRINT #1, CHR$(17); : GOTO 650
720 INPUT #1, E
730 HZ# = N#(8) * 65536! + N#(9)
740 IF T$ = "" THEN 850
750 LOCATE 9, 1: PRINT "Normalizing and storing data - this will take a
minute or two."
760 PRINT
770 OPEN T$ + ".DAT" FOR OUTPUT AS #2
780 REM IRATE = 2 ^ XPT
790 FOR K = 0 TO X - 1
800 REM IJL = IJL + 1
810 REM IF IJL = 16 THEN IJ = IJ + 1: LOCATE 11, 4: PRINT "Finished with
program point"; IJ;
815 LOCATE 11, 4: PRINT "Finished with program point"; K + 1;
820 IF (K - HZ#) * N#(6) < STRT THEN GOTO 840
```

```
830 REM IF IJL = 16 THEN PRINT #2, (K - HZ#) * N#(6), (D(K) - N#(7)) *
N#(5): IJL = 0
835 PRINT #2, (K - HZ#) * N#(6), (D(K) - N#(7)) * N#(5)
840 NEXT K
850 CLOSE : LOCATE 13, 1: PRINT "End of program."
860 BEEP: END
```

TEKTRONIX OSCILLOSCOPE DATA TRANSLATION INSTRUCTIONS

CNVRTWFM Ver 1.94 (cnvrtwfm.exe)

Revisions since Version 1.80

Port to SPARC10 and multiple platform)
Bug fix for vertical offset
Added conversion of ISF files longer than 32767 points
Added conversion of ISF files to mathcad with header
Bug fix for ISF YZERO and YOFF

Description: cnvrtwfm is a utility for converting TDS file system .WFM and TD 100 .ISF files to other waveform formats. Formats generated include CURVE? response compatible binary, and ascii and generic spreadsheet mathcad and .WFM files.

Normal Use: cnvrtwfm in it's default usage converts a list of .WFM files to .ISF files containing a waveform preamble and a curve in 8 bit twos complement. Typical usage:

cnvrtwfm tek00001.wfm	-> creates tek00001.isf
cnvrtwfm *.wfm	-> creates *.isf (converts all wfms)

Advanced Use: cnvrtwfm has a number of command line flags to facilitate custom file output. These are used on the command line with the file list as follows:

cnvrtwfm [flags] <file list>

Flags:

-p	include preamble (default)
-p-	don't include preamble
-d	include waveform data (default)
-d-	don't include waveform data
-8	output 8 bit data (default)
-8-	output 16 bit data
-b	binary output format (default)
-b-	ascii output
-s	swap bytes (Intel default)
-s-	don't swap bytes (Motorola)
-i	show file info on console
-i-	don't show info (default)
-r	output raw data only (no preamble no header)
-r-	don't output raw data only (default)
-l	output spreadsheet data only (no preamble no header)

-l- don't output spreadsheet format (default)
-m output mathcad data only (no preamble no header no x)
-m- don't output mathcad format (default)
-w output wfm files (from .isf input only)
-w- don't output wfm files (default)

Spreadsheet format is a list of comma separated ascii x, y pairs where x is the scaled time axis (0 = trigger) and y is the scaled vertical axis. Pairs are delimited by crlf.

Mathcad data is a list of crlf separated values. If the default header is selected, the first 3 values are the record length, the time between samples, and the jitter of the record in samples. Jitter is expressed as a value between 0 and 1. The header is followed by the data values. If the header is dissabled via the -p- switch, only the data values are output.

Output File Types: Different output file types are labeled via file extension. The default output file extension is ".ISF". ".ISF" files have a waveform preamble and binary curve data. Files in spreadsheet or mathcad format are labeled ".DAT", non-spreadsheet files using ascii format are ".ASC", TDS file system compatible files ".WFM", and all other files are ".WAV".

Examples:

cnvrtwfm -d- -p- -i *.wfm	-> shows file info for all files and creates no output files.
cnvrtwfm -l *.wfm	-> creates spreadsheet output files *.dat.
cnvrtwfm -b- tek00001.wfm	-> creates ascii ouput file tek00001.asc
cnvrtwfm -r -8- tek00001.wfm	-> creates output file tek00001.wav which consists of N 16 bit twos complement values where N is the record length of the .wfm file.
cnvrtwfm -w *.isf	-> creates output files *.wfm

Installation: To install cnvrtwfm copy the cnvrtwfm execuable to a directory which is in your path variable. To display your path variable type path <enter> at your command prompt.

DATAFILE AVERAGING FORTRAN CODE

```
c program AVERAGE.EXE averages oscilloscope readings and writes to a single data
file
      real time(15000),intens,ave(15000)

c zero ave array
      do 100 i=1,15000
         ave(i)=0.0
 100  continue

c open output file
      open(6,file='e:\danno\data\tektron\coat3.dat')

c open oscilloscope output files
      open(10,file='e:\danno\data\tektron\coat3\tek00095.dat')
      open(11,file='e:\danno\data\tektron\coat3\tek00096.dat')
      open(12,file='e:\danno\data\tektron\coat3\tek00097.dat')
      open(13,file='e:\danno\data\tektron\coat3\tek00098.dat')
      open(14,file='e:\danno\data\tektron\coat3\tek00099.dat')
      open(15,file='e:\danno\data\tektron\coat3\tek00100.dat')
      open(16,file='e:\danno\data\tektron\coat3\tek00101.dat')
      open(17,file='e:\danno\data\tektron\coat3\tek00102.dat')
      open(18,file='e:\danno\data\tektron\coat3\tek00103.dat')
      open(19,file='e:\danno\data\tektron\coat3\tek00104.dat')

c loop through data files and sum average
      do 300 i=1,15000
         do 200 j=1,10
            read((9+j),*)time(i),intens
            ave(i)=ave(i)+intens
 200     continue
 300  continue

c close open data files
      close(10)
      close(11)
      close(12)
      close(13)
      close(14)
      close(15)
```

```
      close(16)
      close(17)
      close(18)
      close(19)

      open(20,file='e:\danno\data\tektron\coat3\tek00105.dat')
      open(21,file='e:\danno\data\tektron\coat3\tek00106.dat')
      open(22,file='e:\danno\data\tektron\coat3\tek00107.dat')
      open(23,file='e:\danno\data\tektron\coat3\tek00108.dat')
      open(24,file='e:\danno\data\tektron\coat3\tek00109.dat')
      open(25,file='e:\danno\data\tektron\coat3\tek00110.dat')
      open(26,file='e:\danno\data\tektron\coat3\tek00111.dat')
      open(27,file='e:\danno\data\tektron\coat3\tek00112.dat')
      open(28,file='e:\danno\data\tektron\coat3\tek00113.dat')
      open(29,file='e:\danno\data\tektron\coat3\tek00114.dat')

c loop through data files and sum average
      do 500 i=1,15000
         do 400 j=1,10
            read((19+j),*)time(i),intens
            ave(i)=ave(i)+intens
 400     continue
 500  continue

c close open data files
      close(20)
      close(21)
      close(22)
      close(23)
      close(24)
      close(25)
      close(26)
      close(27)
      close(28)
      close(29)

      open(30,file='e:\danno\data\tektron\coat3\tek00115.dat')
      open(31,file='e:\danno\data\tektron\coat3\tek00116.dat')
      open(32,file='e:\danno\data\tektron\coat3\tek00117.dat')
      open(33,file='e:\danno\data\tektron\coat3\tek00118.dat')
      open(34,file='e:\danno\data\tektron\coat3\tek00119.dat')
      open(35,file='e:\danno\data\tektron\coat3\tek00120.dat')
```

```
      open(36,file='e:\danno\data\tektron\coat3\tek00121.dat')
      open(37,file='e:\danno\data\tektron\coat3\tek00122.dat')
      open(38,file='e:\danno\data\tektron\coat3\tek00123.dat')
      open(39,file='e:\danno\data\tektron\coat3\tek00124.dat')

c loop through data files and sum average
      do 700 i=1,15000
         do 600 j=1,10
            read((29+j),*)time(i),intens
            ave(i)=ave(i)+intens
 600     continue
 700  continue

c close open data files
      close(30)
      close(31)
      close(32)
      close(33)
      close(34)
      close(35)
      close(36)
      close(37)
      close(38)
      close(39)

      open(40,file='e:\danno\data\tektron\coat3\tek00125.dat')
      open(41,file='e:\danno\data\tektron\coat3\tek00126.dat')
      open(42,file='e:\danno\data\tektron\coat3\tek00127.dat')
      open(43,file='e:\danno\data\tektron\coat3\tek00128.dat')
      open(44,file='e:\danno\data\tektron\coat3\tek00129.dat')
      open(45,file='e:\danno\data\tektron\coat3\tek00130.dat')
      open(46,file='e:\danno\data\tektron\coat3\tek00131.dat')
      open(47,file='e:\danno\data\tektron\coat3\tek00132.dat')
      open(48,file='e:\danno\data\tektron\coat3\tek00133.dat')
      open(49,file='e:\danno\data\tektron\coat3\tek00134.dat')

c loop through data files and sum average
      do 900 i=1,15000
         do 800 j=1,10
            read((39+j),*)time(i),intens
            ave(i)=ave(i)+intens
 800     continue
```

```
 900  continue

c close open data files
      close(40)
      close(41)
      close(42)
      close(43)
      close(44)
      close(45)
      close(46)
      close(47)
      close(48)
      close(49)

      open(50,file='e:\danno\data\tektron\coat3\tek00135.dat')
      open(51,file='e:\danno\data\tektron\coat3\tek00136.dat')
      open(52,file='e:\danno\data\tektron\coat3\tek00137.dat')
      open(53,file='e:\danno\data\tektron\coat3\tek00138.dat')
      open(54,file='e:\danno\data\tektron\coat3\tek00139.dat')
      open(55,file='e:\danno\data\tektron\coat3\tek00140.dat')
      open(56,file='e:\danno\data\tektron\coat3\tek00141.dat')

c loop through data files and sum average
      do 1100 i=1,15000
         do 1000 j=1,7
            read((49+j),*)time(i),intens
            ave(i)=ave(i)+intens
 1000     continue
 1100  continue

c close open data files
      close(50)
      close(51)
      close(52)
      close(53)
      close(54)
      close(55)
      close(56)

c loop through and average
      do 1200 i=1,15000
         ave(i)=ave(i)/47.0
```

```
      write(6,*)time(i),ave(i)
1200  continue

      stop
      end
```

APPENDIX G

ERROR ANALYSIS

The standard deviation was calculated for some of the emission spectrums to see how the peaks matched up from plot to plot. The expression for s (standard deviation) is given by:

$$s = \sqrt{\left\{\left(\frac{1}{n-1}\right)\left[\sum_i y_i^2 - \frac{\left(\sum_i y_i\right)^2}{n}\right]\right\}^2}$$

where n is the number of samples and y_i is the specific sample. The table below summarizes the standard deviation values for the emission figures:

TABLE G1
STANDARD DEVIATIONS FOR THE PEAK VALUE

Figure	Peak Location	s
4.1	0.22 μs	$4.81e^{-4}$ μs
4.2	0.20 μs	$2.70e^{-4}$ μs
4.3	0.20 μs	$2.09e^{-4}$ μs
4.4	0.22 μs	$1.13e^{-3}$ μs
4.5	0.20 μs	$2.18e^{-4}$ μs
4.6	0.20 μs	$2.01e^{-4}$ μs
4.7	0.20 μs	$3.29e^{-4}$ μs
4.8	0.20 μs	$1.39e^{-4}$ μs
4.9	0.22 μs	$4.05e^{-4}$ μs
4.10	0.06 μs	$1.75e^{-5}$ μs
4.17	0.20 μs	$6.29e^{-4}$ μs
4.18	0.20 μs	$2.71e^{-4}$ μs

TABLE G1 (cont.)
STANDARD DEVIATIONS FOR THE PEAK VALUE

Figure	Peak Location	s
4.19	0.24 μs	$4.63e^{-4}$ μs
4.20	0.20 μs	$7.10e^{-5}$ μs
4.21	0.24 μs	$3.38e^{-4}$ μs
4.22	0.20 μs	$4.23e^{-4}$ μs
4.23	0.20 μs	$4.77e^{-4}$ μs
4.24	0.20 μs	$1.60e^{-3}$ μs

All of the s values are relatively small which means the plots fall on top of each other from test case to test case.

Figures 4.11-4.16 are not included since they only plot a single test case, but the peak occurs at the same time as above (~.2 μs). The Tektronix scope measurement data was averaged as a whole, thus the standard deviation values could not be calculated (Figures 4.25-4.30). The peak occurs at the same time for all six measurements (~30 ns) and is concluded that they would also agree from measurement to measurement.

VITA

Daniel Joseph Wrona was born on May 12, 1970 in Pittsburgh Pennsylvania. He grew up in Rennerdale and graduated from Chartiers Valley High School in 1988.

In August 1988 he began his studies at Virginia Tech. After four years of school and one year working as a co-op student for Grumman he received a Bachelor of Science in Aerospace Engineering in May of 1993. He continued his education at Virginia Tech pursuing a Master of Science in Mechanical Engineering.

His plans for the immediate future are to work for the Army Aviation Applied Technology Directorate (AATD) testing and evaluating the Army's helicopter fleet.